university of groningen

Modeling the Nonlinear Behaviour of Philips Trimmer

Authors:
N. VISSER (S2692554)
Daily Supervisors:
MSc A. Sarkar
Dr. D. Dirksz (Philips Drachten)

Supervisor:
Prof. dr. ir. J.M.A. Scherpen
Second Supervisor:
Prof. dr. ir. B.Jayawardhana

December 3, 2022

Contents

List of Figures

List of Tables

Nomenclature

A_{lcs} limit cycle amplitude predicted by the condition for harmonic balance

$c_{c,2}$:   damping coefficient cutter

$c_{g.4}$:   damping coefficient guard

$c_{h,3}$:   damping coefficient guard housing

$c_{m,1}$:   damping coefficient motor

$k_{db,2}$:   spring constant driving bridge

$k_{g,4}$:   spring constant guard

$k_{h,3}$:   spring constant housing

$k_{m,1}$:   spring constant motor

$k_{s,5}$:   spring constant coil

$m_{c,2}$:   cutter mass

$m_{g,4}$:   guard mass

$m_{h,3}$:   guard housing mass

$m_{m,1}$:   motor mass

DF   Describing function

DOF: Degrees of freedom

EOM: Equations of motion

FBD: Free body diagram

SISO: single-input single-output

Acknowledgments

First and foremost, I would like to thank my daily supervisor Arijit Sarkar. Our weekly meetings provided me the guidance, ideas, knowledge, literature review I needed to capitalise on for this project. the guidance during the project. Secondly, I'm grateful to Dr. Daniel Dirksz (Philips Drachten) for offering me this project. The feedback I've received from you during our monthly meetings was very useful and kept me on my toes during the project. It was also nice working with you during the joint experiment we conducted together. That being said I would like to thank Philips Drachten for being able to conduct that experiment in one of their facilities. Lastly, I would like to thank prof. dr. ir. Jacquelien Scherpen, for introducing me to the topic of describing functions and for her feedback during our monthly meetings.

Abstract

This study presents a framework to include nonlinearities to a linear model of trimmer dynamics. Nonlinear elements often contribute to the existence of limit cycles in control system. This is undesirable since it intensifies the vibrations that the trimmer already experiences. The framework, to include these nonlinearities, utilises the *describing function method*. This method relies quasi-linearization of the nonlinear component, such that the stability of this system can be studied utilising linear control theory, under strict conditions. Describing function is particular useful for finding limit cycling behaviour. Development and validation of the properties corresponding to the limit cycles are utilised with Matlab simulations, and further validated with experiment.

Despite the describing function method insisted that limit cycling behaviour should exist for a certain amount of play/backlash in the trimmer, experimental data did not support this with evidence.

A potential explanations is presented, stating that the Coulomb friction between some of the fundamental components of the trimmer alleviates the magnitude of the predicted limit cycle. Other play models are introduced to the system to facilitate for a more generic justification that only stable limit cycles can occur over a fixed range of frequencies. It showed that this range is bounded by the contours of the describing function for the two limiting cases for friction-, and inertia-controlled backlash.

Keywords: describing function theory, nonlinear control theory, self-sustained oscillations

Chapter 1

Introduction

Trimmer is an essential electronic gadget in everyday life of a human being. Therefore, it's critical that the user has a pleasant experience. Vibration is evident during the use of the trimmer. However, increasing vibrations can lead to unpleasant experience for the user. Vibrations may originate from a various sources, thus not all of them can be regulated or eliminated. This research is devoted to investigate vibrations caused by nonlinear elements within trimmer dynamics.

Trimmers are devices that comprise many interconnecting elements, to realise the reciprocating movement. Typically, the distinctive elements are made of a various materials. Some elements are made of PU, while other elements are made from a steel alloy. Some of the interconnecting elements are designed in such a way that there is a certain amount of play between the elements. Vibrations inside the device may also be caused by play in addition to the oscillatory motion of the components of the trimmer. It is therefore desirable to investigate the relations between the amount of play and the induced extra vibration generated by it.

Currently, Philips Drachten is working towards a model-based system engineering approach. This reduces the need for prototyping and enables designers to comprehend the effects of altering model parameters since a virtual representation of the trimmer is created. In the world of engineering, this virtual representation is also known as a 'digital twin'. A digital twin, of any device, is its counterpart in virtual representation, and can be used for product optimisation.

As of now, Philips Drachten does have a complex system (digital twin) for their linear trimmer model. However, the nonlinear elements, such as play and friction, have yet to be added to this model. It is anticipated that these nonlinearities may contribute to the additional vibrations.
This project's objective is to incorporate these nonlinearities into the linear digital twin and investigate how they affect the vibrations.

The problem statement for this research project is formulated as follows:

There is a gap of knowledge in understanding the vibrations caused by nonlinearities. Specifically, the relationship between the amount of play and the induced additional vibrations is unknown.

1.1   System description

This section will give a brief description of the relevant elements/components within the trimmer. A complete mathematical framework will be derived the chapter 2.
The basic operation of a trimmer is as follows: a saw-patterned blade moves on top of another saw-

patterned blade with high reciprocating motion, enabling hair to be cut.

As briefly stated before, this operation is accomplished by means of interconnecting elements. It is beyond the scope to analyse all components, within trimmer, only the essential components are studied here. The essential components are shown in Figure 1.1.
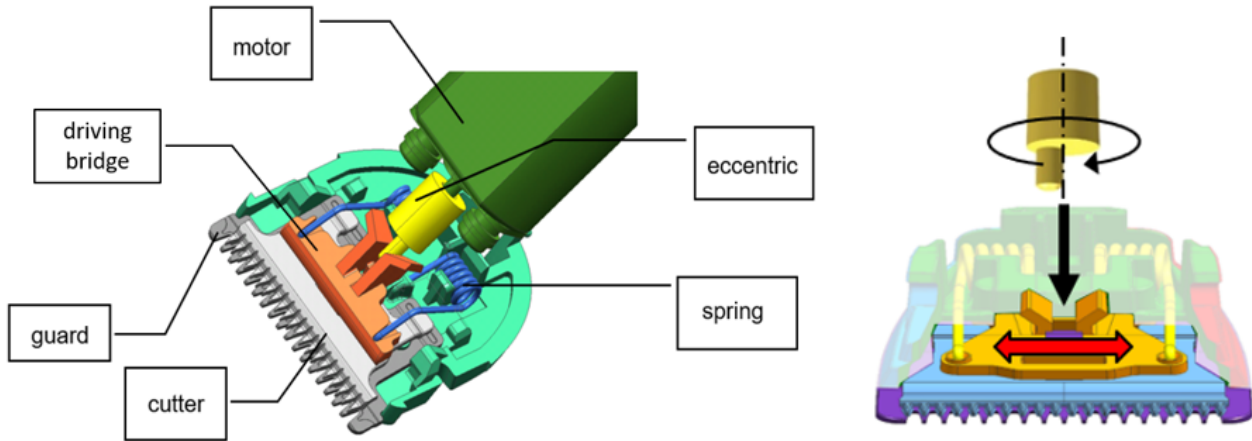
Figure 1.1: Schematic overview of the relevant components of the Philips trimmer. Image retrieved from Philips Drachten

Figure 1.1 shows that an eccentric pin in mounted to the plastic cylindrical shell (yellow). The shell is directly attached to an electrical motor, which allows the shell to rotate and cause the pin to oscillate. Due to the eccentricity of the pin, it can convert the oscillating motion into a reciprocating motion, shown by right-hand figure of Figure 1.1. The driving bridge is made of plastic element that has two vertically raised edges on either side, in which the pin precisely fits. However, due to manufacturing errors, it can happen that there is a certain amount of play between the pin and the driving bridge.

Figure 1.1 shows that the 'cutter', is rigidly connected to the driving bridge. The cutter is pressed to the 'guard' by means of a spring. From that it is observed that the guard is connected to the guard housing which is in turn connected to the plastic housing containing the electric motor.

So for this trimmer, there is only play between the pin and the driving bridge which may cause vibrations. Frictional force between the cutter and guard is another nonlinear element that must be taken into account when creating the overall nonlinear digital twin.

The outline of the research project is as follows. In Chapter 1, the research objective and relevant research questions are presented. Then in Chapter 2 a mathematical framework is defined that models the linear dynamic behaviour of the trimmer. Subsequently, a nonlinear framework that is able to include the nonlinear elements is introduced, which is known as the describing function method. The nonlinear model is then analysed by means of Simulink models. Especially, the time response of these Simulink model is investigated by means of Fast Fourier Transform, check if the frequency response indicates the existence of limit cycles in the nonlinear systems. Two configuration of control system are analysed, namely the open-, and closed-loop configuration. Where to open-loop configuration facilitates to validate the experimental results obtained in Chapter 3. While the closed-loop configuration can better be used the check for the general condition for harmonic balance. In Chapter 4 Matlab codes are presented and validate. Subsequently, the results generated by using some of these codes are analysed in Chapter 5. Afterwards, the implication(s) of the major results will be discussed in Chapter 6. In addition, some future research topics, regarding these major results, are opted for. Finally, the main results are summarised in Chapter 7. Furthermore, in Chapter 7 the research question, presented in the next sections, will be answered.

Since this project was largely based on the computation of Matlab codes, for the readability of this thesis, the codes are not included in the main body, but are presented in the Appendix A.

1.2   Research objective

The main objective of this research project is to obtain a better understanding of the vibrations induced by play. This enables designers to quantify the implications caused by play and hence potentially minimise this effect by changing model parameter(s). Specifically, there is a gap in knowledge on the underlying effects of the nonlinear components, such as play, contributing to the existence of limit cycle, and hence additional vibrations that occur due to these limit cycles. Future work has to translate and quantify to predicted limit cycles to vibrations.

A solid approach to study these effects is to construct a digital twin, that is able to describe to motion of the trimmer and that can predict the existence of limit cycles causing vibrations. This leads to the following research objective:

Design a digital twin which describes the behaviour of nonlinear trimmer dynamics, and is able to predict the existence of limit cycles due to the presence of play. So, a model that describes the relationship between the induces vibrations caused by play is desirable.

1.3   Research question

The motivation and research objective is accurately presented, which can be summarised into mean and sub research questions:

- What is the influence of the size of play to the induced limit cycles and hence to observed vibrations?

  - What is the effect of damping on the linear stability of the system?
  - What is the influence the play element to the stability and performance of the system?
  - What is the influence of the frictional components the stability and performance of the system?
  - What is the influence of the input amplitude, and backlash width, to the stability and performance of the system?
  - What is the influence of the input frequency to the stability and performance of the system?
  - How does the predicted limit cycle, by the describing function method, manifest itself in the output of the system?

Hypothesis
It is expected that for a certain amount of play, limit cycling existence are present, with a corresponding amplitude an frequency. Additionally it is expected that increasing amount of play will lead to a limit cycle with an increasing amplitude.

Chapter 2

Theory

The mathematical theory presented in this chapter, provides the reader with necessary information to understand the developed method required to predict limit cycling behaviour in trimmer dynamics. There will be a clear distinction between the linear (section 2.2) and nonlinear (section 2.3) models for the trimmer dynamics. First the linear model is presented. Subsequently, the linear model is used as a foundation for the nonlinear model, where play and friction are added. As briefly stated before, the method used to incorporate the nonlinear elements in to the linear model is known as the describing function method. This method will be presented in section 2.3.

2.1 Problem description

Depending on the amount of play, the trimmer might induce unpleasant vibrations. These vibrations resulting from induced limit cycles. Currently, Philips Drachten has a digital twin that is able to describe the linear model with a certain precision. However, as stated before, this model does not include the nonlinear elements such as: play and friction. There are several techniques to include these nonlinearities. In general a nonlinear system can be analysed via linearization around an operating point. However, the resulting system can only be analysed around a single operating point. Even small perturbations from that operating point might cause the model the malfunction. Another method to analyse nonlinear systems is the describing function method. This method is a quasi-lineralization method and is particularly useful for prediction of limit cycles associated with nonlinear system.

2.2 Linear trimmer dynamics

As shown see in the upcoming sections, the describing function method is a quasi-linearization approach based on a nonlinear system being subjected by a linear transfer function, in terms of a closed-loop configuration. In other words, the linear part of the model has to be separated from the nonlinear part of the model. To use the describing function method, there are a few restrictions on the linear part of the model. It will be shown in section 2.3 that the main restriction is that the linear part behaves as a 'low-pass' filter. A linear transfer function frequency response study is required to verify this restriction. State-space representations result in the transfer function, which in turn are easily obtained from the equations of motion.

2.2.1 Equations of motion trimmer dynamics

Classical mechanics ascribes several methods to obtain the equations of motion (EOM) . Euler-Lagrange, Newtonian and Hamiltonian will all produce the same set of EOM. The popular Euler-Lagrange method was chosen for this project since Euler-Lagrange facilitates the use of generalised

coordinates. In other words, the direction of the coordinates, describing the motion, does not have to be taken into account. This is a direct consequence of the Euler-Lagrange being 'energy-based', whereas Newtonian and Hamiltonian mechanics are 'force-based' methods, and thus depend on a well-defined coordinate base.

Based on a Free Body Diagram (FBD) of the trimmer's essential components, the energy functions associated with Euler-Lagrange mechanics can be derived. An illustration of the essential components with the related FBD is shown in Figure 2.1.

(a) Schematic illustration   (b) FBD: of essential components
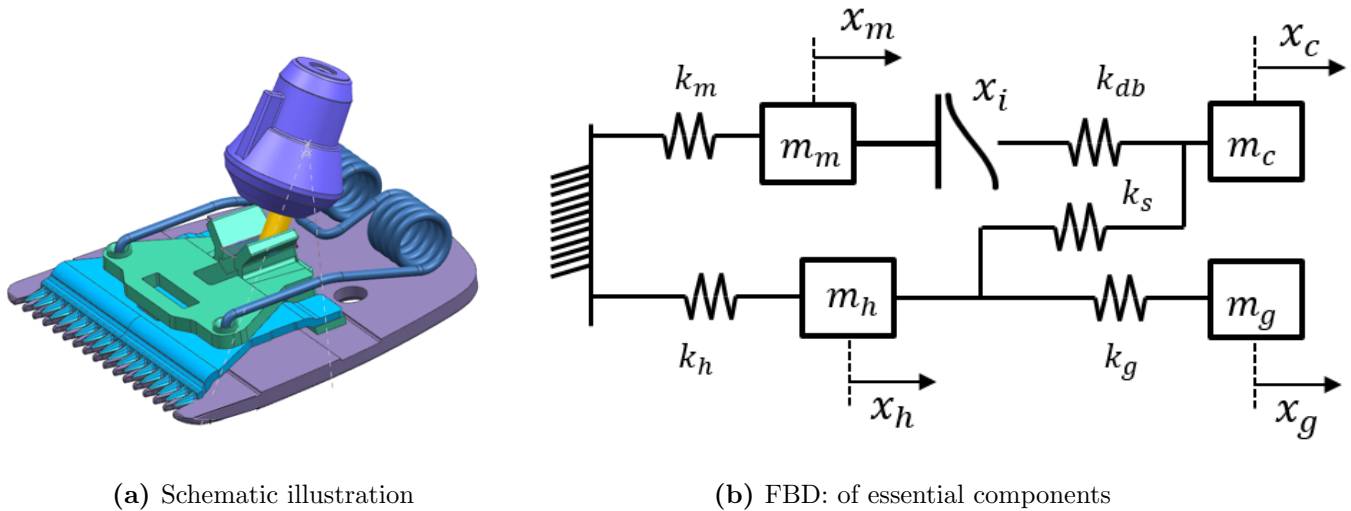
Figure 2.1: Schematic illustration of the essential components, with the related FBD. Illustration obtained from Philips Drachten

where m_m = motor mass, m_h= guard housing mass, m_g= guard mass and m_c= cutter mass , corresponding to the illustration shown by Figure 1.1. The same scripts hold for the position and springs, with the additional spring k_s which is the coil spring stiffness. As explained before, the system described by Figure 1.1 is driven by an electric motor. This motion is considered as in input x_i in Figure 2.1b. A pin is eccentrically mounted on top of a cylindrical shell. In advance, the pin is located precisely between the edges of the driving bridge shown in Figure 2.1b, such that the rotating motion of the pin is converted to reciprocating motion of the driving bridge and hence the cutter. This can better be explained by considering the top view of the shaft with the eccentric pin Figure 2.2.
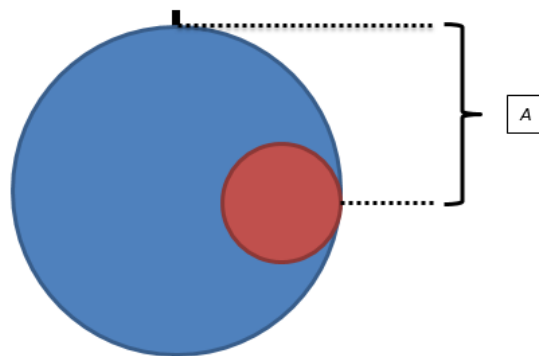
Figure 2.2: Top view: cylindrical shaft with eccentric pin mounted on top. Where A is the amplitude of the displacement input, resulting from the eccentricity of the pin with respect to the middle of the cylindrical shaft.

The oscillating motion of the pin is obtained, since the pin has an eccentric position with respect to the cylindrical shell. An oscillating motion can be mathematically expressed as follows:

$$x_i(t) = A\sin(2\pi ft) \tag{2.1}$$

where A is the amplitude (shown in Figure 2.2), or magnitude of the eccentric distance and f is the rotating frequency, i.e. the rotational speed of the electric motor.

From Figure 2.1b, with the consideration that x_i is denoted as Equation 2.1, the EOM are derived by means of the Euler-Lagrange method, which depend on the 'Lagrangian'. The Lagrangian states the difference between the kinetic and potential energy of the system, and is denoted as Equation 2.2:

$$\mathcal{L}(q, \dot{q}) = T - U \tag{2.2}$$

where q represent the position state vector, $\dot{q}$ represent the velocity state vector, T represents the kinetic energy and U represents the potential energy. Figure 2.1 shows that the model contains four masses, all these masses contribute to the total kinetic energy of the system. The amount of kinetic energy depends on the relative velocity of the corresponding masses. In general the total kinetic energy of a system is denoted by:

$$T(\dot{q}_i) = \sum_{i=1}^{n} \frac{1}{2} m_i \dot{q}i^2 \tag{2.3}$$

It follows that the total kinetic energy, for trimmer dynamics, is denoted as:

$$T(\dot{q}_1, \dot{q}_2, \dot{q}_3, \dot{q}_4) = \frac{1}{2} m_1 \dot{q}_1^2 + \frac{1}{2} m_2 \dot{q}_2^2 + \frac{1}{2} m_3 \dot{q}_3^2 + \frac{1}{2} m_4 \dot{q}_4^2 \tag{2.4}$$

where $m_1 = m_m$, $m_c = m_2$, $m_h = m_3$ and $m_g = m_4$, same script applies to the springs and dampers. The position and velocity terms of each mass are expressed in terms of q_i and $\dot{q}_i$ respectively, to leave room for the state-variables introduced in the latter stage.

The potential energy function represented by U, requires more effort. A spring's potential energy is determined by its relative displacement. I.e. if a spring is fixed on one side and elongated on the other side the potential energy in that particular spring is determined by the displacement of the elongated side of the spring. If a spring is not fixed on one side, the potential energy in that particular spring is determined by the relative displacement between the two ends of the spring. For the system, springs of: k_{db}, k_s and k_g have potential energy based on the displacement of neighbouring masses. Based on these assumptions, the potential energy of the system is defined as follows:

$$U(q_1, q_2, q_3, q_4) = \frac{1}{2} k_1 (q_1)^2 + \frac{1}{2} k_2 (q_2 - q_1 - u)^2 + \frac{1}{2} k_3 q_3^2 + \frac{1}{2} k_4 (q_4 - q_3)^2 + \frac{1}{2} k_5 (q_2 - q_3)^2 \tag{2.5}$$

where q_i represents the positional state vector and u represents the displacement function of the eccentric pin. Now that the kinetic and potential energy function are defined the Lagrangian follows from Equation 2.2. The Lagrangian is then used is the Euler-Lagrange equations, denoted by Equation 2.6:

$$\frac{d}{dt}\left(\frac{\partial \mathcal{L}}{\partial \dot{q}_i}\right) - \frac{\partial \mathcal{L}}{\partial q_i} + \frac{\partial R}{\partial \dot{q}_i} = Q_i \tag{2.6}$$

where $\mathcal{L}$ is the Lagrangian , q_i is the position state vector, $\dot{q}_i$ is the velocity state vector Q_i accounts for the externally applied input to the system and R is the dissipation function. The latter function accounts for the elements that dissipate energy out of the system. Dissipating elements are dampers and frictional components. For the linear system friction will not be accounted for[1]. The dissipation function is then denoted as:

$$R = \frac{1}{2} c_1 \dot{q}_1^2 + \frac{1}{2} c_2 (\dot{q}_2 - \dot{q}_1 - \dot{u})^2 + \frac{1}{2} c_3 \dot{q}_3^2 + \frac{1}{2} c_4 (\dot{q}_4 - \dot{q}_3)^2 \tag{2.7}$$

---

[1]For the nonlinear system, the Coulomb friction might be added to the EOM

where $\dot{u}$ is the input velocity differentiated from the input displacement function: $u(t) = x_i(t) = A\sin(2\pi ft)$, such that:

$$\dot{u} = \frac{du}{dt} = \frac{d}{dt}(A\sin(2\pi ft))$$
$$\dot{u} = 2\pi f\cos(2\pi ft)$$

(2.8)

Plugging Equation 2.4, Equation 2.5 andEquation 2.7 into the Euler-Lagrange equation Equation 2.6, yields the four EOM for the four each essential components illustrated in Figure 2.1b:

$$\ddot{q}_1 = \frac{1}{m_1}\left[-(c_1 + c_2)\dot{q}_1 + c_2\dot{q}_2 - (k_1 + k_2)q_1 + k_2q_2 - k_2u - c_2\dot{u}\right]$$

$$\ddot{q}_2 = \frac{1}{m_2}\left[c_2\dot{q}_1 - c_2\dot{q}_2 + k_2q_1 - (k_2 + k_5)q_2 + k_5q_3 + k_2u + c_2\dot{u}\right]$$

$$\ddot{q}_3 = \frac{1}{m_3}\left[-(c_3 + c_4)\dot{q}_3 + c_4\dot{q}_4 + k_5q_2 - (k_3 + k_4 + k_5)q_3 + k_4q_4\right]$$

$$\ddot{q}_4 = \frac{1}{m_4}\left[c_4\dot{q}_3 - c_4\dot{q}_4 + k_4q_3 - k_4q_4\right]$$

(2.9)

An example derivation of $\ddot{q}_1$ is shown in Appendix D. From the EOM defined by Equation 2.9, the state-space representation directly follows. State-space representation is a mathematical model of a physical system as a set of input, output and state variables related by first-order differential equations instead of the above second-order differential equations. State-space representation can be easily used to study the stability of linear systems. In addition, the transfer function used for the describing function methods results from the state-space representation. In matrix form, the general form of the state-state representation is:

$$\dot{q}(t) = Aq(t) + Bu(t)$$
$$y(t) = Cq(t) + Du(t)$$

(2.10)

where $q(t)$ is the state vector, $y(t)$ is the output vector, $u(t)$ is the input vector, A is the state matrix, B is the input matrix, C is the output matrix and D is the feedforward matrix.

The state vector is defined as: $x_1 = q_1$, $x_2 = q_2$, $x_3 = q_3$, $x_4 = q_4$, $x_5 = \dot{q}_1$, $x_6 = \dot{q}_2$, $x_7 = \dot{q}_3$ and $x_8 = \dot{q}_4$, that leads to:

$$\dot{x}_1 = x_5$$
$$\dot{x}_2 = x_6$$
$$\dot{x}_3 = x_7$$
$$\dot{x}_4 = x_8$$
$$\dot{x}_5 = \frac{1}{m_1}\left[-(c_1 + c_2)x_5 + c_2x_6 - (k_1 + k_2)x_1 + k_2x_2 - k_2u - c_2\dot{u}\right]$$
$$\dot{x}_6 = \frac{1}{m_2}\left[c_2x_5 - c_2x_6 + k_2x_1 - (k_2 + k_5)x_2 + k_5x_3 + k_2u + c_2\dot{u}\right]$$
$$\dot{x}_7 = \frac{1}{m_3}\left[-(c_3 + c_4)x_7 + c_4x_8 + k_5x_2 - (k_3 + k_4 + k_5)x_3 + k_4x_4\right]$$
$$\dot{x}_8 = \frac{1}{m_4}\left[c_4x_7 - c_4x_8 + k_4x_3 - k_4x_4\right]$$

(2.11)

From Equation 2.10, it follows that the A-matrix is:

$$A = \begin{pmatrix} 0 & 0 & 0 & 0 & 1 & 0 & 0 & 0 \\ 0 & 0 & 0 & 0 & 0 & 1 & 0 & 0 \\ 0 & 0 & 0 & 0 & 0 & 0 & 1 & 0 \\ 0 & 0 & 0 & 0 & 0 & 0 & 0 & 1 \\ -\frac{k_1+k_2}{m_1} & \frac{k_2}{m_1} & 0 & 0 & -\frac{c_1+c_2}{m_1} & \frac{c_2}{m_1} & 0 & 0 \\ \frac{k_2}{m_2} & -\frac{k_2+k_5}{m_2} & \frac{k_5}{m_2} & 0 & \frac{c_2}{m_2} & -\frac{c_2}{m_2} & 0 & 0 \\ 0 & \frac{k_5}{m_3} & -\frac{(k_3+k_4+k_5)}{m_3} & \frac{k_4}{m_3} & 0 & 0 & -\frac{(c_3+c_4)}{m_3} & \frac{c_4}{m_3} \\ 0 & 0 & \frac{k_4}{m_4} & -\frac{k_4}{m_4} & 0 & 0 & \frac{c_4}{m_4} & -\frac{c_4}{m_4} \end{pmatrix} \tag{2.12}$$

where $A \in \mathbb{R}^{8\times8}$. The B-matrix is:

$$B = \begin{pmatrix} 0 & 0 \\ 0 & 0 \\ 0 & 0 \\ 0 & 0 \\ -\frac{k_2}{m_1} & -\frac{c_2}{m_1} \\ \frac{k_2}{m_2} & \frac{c_2}{m_2} \\ 0 & 0 \\ 0 & 0 \end{pmatrix} \tag{2.13}$$

where $B \in \mathbb{R}^{8\times2}$. From the dimensions of the B-matrix, it follows that the state-space representation requires a dual input vector $u(t)$. This is a direct consequence that the systems contains velocity dependent $(\dot{u}(t))$ components such as dampers. The output equation of Equation 2.10 depend on the value of interest. The determination of limit cycles is further investigated by means of the relative displacement between the cutter and the guard, which forces the output vector Equation 2.10 $(y(t))$ to be:

$$\vec{y}(t) = \underbrace{\begin{pmatrix} 0 & 1 & 0 & -1 & 0 & 0 & 0 & 0 \end{pmatrix}}_{C} q(t) \tag{2.14}$$

leading to $C \in \mathbb{R}^{1\times8}$. The linear model can be either be analysed by the EOM defined by Equation 2.9 or by Equation 2.10 and corresponding matrices. Stability of the system is easily determined by the latter representation.

As stated before, the describing function method only applies for systems where the linear part of the model behaves as a low-pass filter. By using the state-space representation derived in this section, the frequency response of the linear system can be determined to quantify whether or not the linear part of the system behaves like a low-pass filter.

2.2.2   Frequency response

The frequency response is a quantitative measurement between the ratio of input and output signal. These measurements provide information about the magnitude and phase shift between an input and output signal. A widely used, method to analyse these properties, is the Bode plot. The Bode plot method is a graphical representation of frequency response. Generally, the Bode plot of a single-input, single-output systems consist of two plots stacked on top of each other. The top plot is providing the magnitude shift, while the bottom plot provides information about the phase shift of the output signal corresponding to the input signal.

The transfer function Equation 2.21 is used to find the magnitude and phase shift to a periodic input

signal $u(t)$ and output signal $y(t)$. A block diagram, of the transfer function $G(s)$, in frequency domain is shown in Figure 2.3. Substituting $s = j\omega$ into the Laplace transform of the linear system,
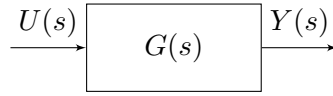
Figure 2.3: Block diagram of a linear system, described by the transfer function $G(s)$

Equation 2.21, yields the magnitude:

$$\left| \frac{A_y}{A_u} \right| = |G(j\omega)| \tag{2.15}$$

and the phase shift of between the input and output signal:

$$\angle G(j\omega) = \phi(j\omega) = \phi \tag{2.16}$$

To obtain the transfer function $G(s)$ shown by Figure 2.3, the Laplace transform of the input and output signal has to be taken, $u(t) \rightarrow U(s)$ and $y(t) \rightarrow Y(s)$ respectively. Laplace transforming a function is converting a continuous-time signal into the frequency domain of that system, s-space. From Figure 2.3 it follows that the output signal in s-space is produced by multiplying the input signal $U(s)$ with the transfer function $G(s)$, resulting in:

$$Y(s) = G(s)U(s) \tag{2.17}$$

Inferring from the general definition of the Laplace transform for one-sided functions beginning at $t = 0$, the output signal $y(t) \rightarrow Y(s)$ is obtained using the Equation 2.18 [4].

$$Y(s) = \mathcal{L}\{y(t)\} = \int_0^\infty y(t)e^{-st} \tag{2.18}$$

^{2} and for the input signal $u(t) \rightarrow U(s)$:

$$U(s) = \mathcal{L}\{u(t)\} = \int_0^\infty u(t)e^{-st} \tag{2.19}$$

Rewriting Equation 2.17 shows that the transfer function is obtained by taking the ratio between $U(s)$ and $Y(s)$. The transfer function $G(s)$ can be obtained by measuring the output frequency for a specific input frequency for a range of frequencies. However, as this requires a lot of time, a faster, more efficient method is developed which is related to the state-space representation presented above by Equation 2.10. Take the Laplace transform on both sides of the state-space representation yields:

$$sQ(s) = AQ(s) + BU(s)$$
$$Y(s) = CQ(s) + DU(s) \tag{2.20}$$

where $sQ(s)$ results form the Laplace transform of a derivative function, namely $\dot{q}(t)$. Equation 2.20 shows a system with 2 equations and 2 unknowns, which can then be used to solve for the ratio between $Y(s)$ and $U(s)$, leading to the transfer function:

$$G(s) = \frac{Y(s)}{U(s)} = C(sI - A)^{-1}B + D \tag{2.21}$$

the full derivation of the transfer function is shown in Appendix D. The state-space representation's matrices A, B, C, and D are now the only variables that affect the transfer function $G(s)$, denoted by Equation 2.21.

---

^{2}The '$\mathcal{L}$', from the Laplace transform is different than the '$\mathcal{L}$' resulting from the Lagrangian

2.2.3   Linear Stability Analysis

There are numerous methods for evaluating the stability of the linear component of the model. Here is a description of two of these methods each serving their one purpose.

The first method to determine the stability of the open-loop linear system is examined by the observation of the eigenvalue's 'location', corresponding to the A-matrix defined in state-space representation. Given the state-space representation Equation 2.10, the eigenvalue problem of this matrix results in:

$$\det(A - \lambda I) = 0 \tag{2.22}$$

The eigenvalues, resulting from the solutions of Equation 2.22, might be complex-valued numbers ($\lambda_k \in \mathbb{C}$) but the open-loop stability is only determined by checking if the eigenvalues of the A-matrix all have negative real-part.

Corollary 2.2.0.1 *If the $Re(\lambda_k) \leq 0$ for each k, then $|e^{At}| \leq K e^{-\gamma t}$ for some $\gamma \geq 0$*

The imaginary-part of the complex-valued eigenvalues correspond the resonance frequencies of the system. The implications of these resonance frequencies will be analysed in subsection 5.1.2.

Another methods to determine the stability of a linear time invariant system is the so-called Nyquist stability criterion. The Nyquist stability criterion is a graphical technique for determining the stability of a dynamical system [5].

It relates the open-loop frequency response and pole location to the stability of the closed-loop system. The foundations of the Nyquist criterion are based on Cauchy's argument principle, which is a graphing technique, resulting from the contour of the transfer function on the complex plane.

The contour of the transfer function is obtained by plotting: $G(s) \to G(j\omega)$, from $s = -j\infty$ to $s = +j\infty$. The direction of increasing frequencies has to be draw on this contour. In terms of Nyquist stability criterion encirclements are points, corresponding to poles are zeros, in the complex plane that are encircled by the contour. Keep in mind the the encirclements can be either enclosed by the contour in clockwise are counterclockwise direction. From the number of encirclements the principal argument is defined. Zeros and poles, in the right hand plane (RHP) of the complex plane, are defined as Z and P respectively. Assuming that the Nyquist plot of the transfer function encircles the origin N times, the principal argument then states:

$$N = Z - P \tag{2.23}$$

where the sign of N determines whether the encirclements are clockwise are counterclockwise.

The closed-loop stability arises from the open-loop stability criterion described above. An extension of the closed-loop stability criterion is used when the nonlinear component(s) are introduced to the system in terms of the describing function. The description function might be viewed as another transfer function for the time being, denoted by $N(s)$ [3]. Adding $N(s)$ to Figure 2.3 and converting the open-loop configuration to the closed-loop configuration lead to the feedback system shown in Figure 2.4. For this closed-loop configuration, the transfer function bet between input $U(s)$ and output $Y(s)$ is defined as:

$$M(s) = \frac{G(s)}{1 + G(s)N(s)} \tag{2.24}$$

From the closed-loop system the following observations are made:

1. Closed-loop system is stable if and only if $M(s)$ has zero RHP poles.

2. Poles of $M(s)$ equal the zeros of $1 + G(s)N(s)$.

---

[3]The describing function will be thoroughly analysed in the upcoming sections
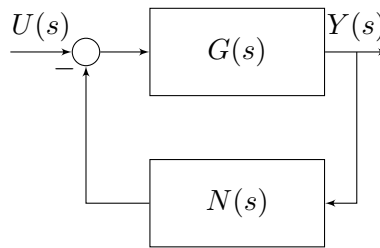
Figure 2.4: General feedback system

3. If Nyquist plot $1 + G(s)N(s)$ encircles origin, then $G(s)N(s)$ will encircle $(-1, j0)$ in complex plane.

Combining the arguments leas to the following statement[6]:

> *Closed-loop system is stable if the number of RHP poles in $G(s)N(s)$ equals the number of counter-clockwise encirclements of the point $(1, j0)$ by the Nyquist plot of $G(s)N(s)$*

When assessing the stability of the potential limit cycles anticipated by the describing function, the extension of this Nyquist stability criterion is taken into consideration.

2.3   Nonlinear trimmer dynamics

There are several methods to incorporate the nonlinear elements to the linear model described above. For this study, the describing function method, abbreviated with DF is chosen since this method is prescribed when determining the existence of limit cycles caused by the nonlinear component(s) in trimmer dynamics, which are: play and friction. In advance, the predicted limit cycles contribute to the additional vibrations, which are unpleasant. A limit cycle is a closed trajectory such that at least one other trajectory spirals into it. Stability of limit cycles follows directly from the Nyquist stability criterion defined in the previous section.

2.3.1   Introduction to the Describing Function Method

As derived in the previous section, for the linear dynamics, the frequency response method, in terms of the transfer function, is a powerful tool for analysing linear systems. Since transfer functions cannot be applied to nonlinear systems, this approach is constrained when nonlinear components are taken into account.

During the second half of the 20th century, a lot of research was done on an extension of the frequency response method onto nonlinear systems. One of the solutions they can up with is the DF method. This method approximates the nonlinear component by a quasi-linear element, and can therefore be treated in the light of the extension of the Nyquist stability criterion defined by Equation 2.24. In other words, the nonlinear component is replaced by a quasi-linear component whose gain is a function of input amplitude [7].

Nonlinearities can be classified into continuous and discontinuous nonlinear systems. The DF method is particularly useful for so-called: hard-nonlinearities. Hard-nonlinearities are discontinuous nonlinearities at some point over the entire domain of that nonlinearity. I.e., the nonlinearity is locally not differentiable at that particular discontinuity and hence the nonlinearity cannot be approximated by linear functions. However, hard-nonlinearities are in some sense almost linear (quasi-linear). Almost linear since hard-nonlinearities are either on or off, for example an Coulomb friction. In other words,

if the input velocity, subjected to the nonlinear Coulomb friction, has reached a certain velocity the output will instantaneously switch to a linear regime. Other hard-nonlinearities are: saturation, deadzone and backlash. Fundamentally, the idea of the DF method can best be introduces by assuming a limit cycling exists in a closed-loop configuration [8]. Consider that this limit cycle is present in the closed-loop configuration shown by Figure 2.5 with a fixed amplitude and frequency. In this configuration the nonlinear block is denoted by $N(A, \omega)$, whereas the linear block is denoted by $G(j\omega)$[1]. This closed-loop configuration looks similar to the previously defined closed-loop configuration de-
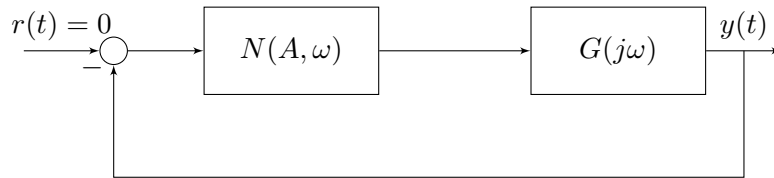
Figure 2.5: Block diagram of linear model with nonlinear input and $r(t) = 0$

noted with Figure 2.4, where $N(s) \rightarrow N(A, \omega)$. The goal here is to find this quasi-linear frequency response function in terms of input amplitude and frequency [2]. This function is known as the DF corresponding to a particular nonlinearity. To derive the DF itself, it must first be noted that the 'condition for harmonic balance' follows directly from the loop transfer function from Figure 2.4, which is denoted as: $1 + G(s)N(s) = 0$. Similarly, the loop transfer function of the configuration shown by Figure 2.5 can be derived by assuming that a self-sustained oscillation exist with a fixed amplitude A and frequency ω, leading to:

$$N(A, \omega)G(j\omega) + 1 = 0 \tag{2.25}$$

Equation 2.25 is the general form of the 'condition for harmonic balance'.

2.3.2 Applications and Assumptions for the Describing Function Method

Applications
Using the DF approach to analyse nonlinear systems is not always possible. To utilise this approach, some formal restrictions must be defined. It is necessary for the nonlinearities to be almost linear, otherwise the frequency response cannot be determined for that element. [9]. In addition, the fact of the limit cycle could by approximated by a sinusoid. The well-known Van der Pol equation, however, shows that elliptic shape limit cycles can occur for fixed amplitudes and frequencies if $\alpha \geq 0$ [10].

Predicting limit cycles is important since limit cycles occur in most nonlinear system. Usually, the occurrence of limit cycles undesirable since they:

1. Contribute to poor control accuracy

2. Contribute to increasing wear or even mechanical failure

3. Contribute to unpleasant additional vibrations and noise

Therefore, it is crucial to understand the effect of the occurrence the limit cycle(s) in the trimmer dynamics since they contribute to unpleasant additional vibrations and noise. It is usually sufficient to know that limit cycles exist, with corresponding amplitudes and frequencies, within a system, without knowing their exact waveform.

Assumptions
Limit cycle(s) of the system shown in Figure 2.5 can be found with the DF method. However, the system has to satisfy the following four conditions[2]:

1. There is only a single nonlinear component.
   This assumption indirectly implies that if there are more than 1 nonlinearties, the set of nonlin-earities has to be lumped together.

2. The nonlinear component is time-invariant.
   This assumptions is made because the Nyquist criterion, on which the stability of the DF method is based, applies only for linear time-invariant systems.

3. Corresponding to a sinusoidal input $u(t) = sin(\omega t)$, only the fundamental component $u_1(t)$ must be considered.
   This is a crucial assumption for the DF method since the DF method is an approximate method. This assumption implies that the higher frequency harmonics, in the output signal form the nonlinearity $u(t)$, can be neglected. Therefore the linear part of the system must behave as a low-pass filter, i.e.:

$$|G(j\omega)| \gg |G(jn\omega)|, \qquad\qquad for \qquad\qquad n = 2, 3, ... \qquad (2.26)$$

   Previously mentioned low-pass filtering condition must applicable for the linear part of Fig-ure 2.5, hence higher harmonics of periodic signal, caused by the nonlinear component, will be attenuated. Only fundamental harmonic will pass through the linear part of the system. There-fore it is appropriate to assume that the signal, passing through the entire system, is basically a sinusoid corresponding to the self-sustained oscillation.

4. The nonlinearity is odd, i.e. $f(-y) = -f(y)$ for all y so that no rectification occurs.

These assumptions will come back throughout this research, especially the third assumption is critical. This assumption is also known as the 'filtering hypothesis'.

2.3.3 Definitions Describing Function Method

The DF can be derived with the limitations defined in the preceding section. For now only consider the nonlinear component of Figure 2.5 defined by $N(A, \omega)$ shown in Figure 2.6.
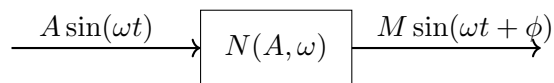
Figure 2.6: Describing Function representation nonlinear element

On the assumption that a self-sustained oscillation, with a sinusoidal shape, is present within the system shown by Figure 2.5, at some time it has to pass trough the nonlinear element $N(A, \omega)$. The limit cycle can be defined as:

$$u(t) = A\sin(\omega t) = Ae^{j\omega t} \qquad (2.27)$$

where A is the amplitude and ω the frequency of the limit cycle. If the input signal of a nonlinear element is periodic, then the output signal will also be periodic, but shifted in amplitude and phase. Despite the shift in amplitude and frequency, the output signal can be approximated with a Fourier series. Approximating the output signal $y(t)$ with a Fourier series:

$$y(t) = \frac{a_0}{2} + \sum_{n=1}^{\infty}(a_n\cos(n\omega t) + b_n\sin(n\omega t)) \qquad (2.28)$$

where the Fourier coefficients a_i and b_i can be determined with:

$$a_0 = \frac{1}{\pi} \int_{-\pi}^{\pi} y(t) d(\omega t)$$
$$a_n = \frac{1}{\pi} \int_{-\pi}^{\pi} y(t) \cos(n\omega t) d(\omega t) \qquad (2.29)$$
$$b_n = \frac{1}{\pi} \int_{-\pi}^{\pi} y(t) \sin(n\omega t) d(\omega t)$$

The standard caveat is that the transfer function should behave as a low-pass filter, third assumption above, such that higher harmonics will be attenuated. In addition the fourth assumptions yields: $a_0 = 0$. With these assumptions in mind, only the base Fourier coefficients a_1 and b_1 remain:

$$a_1 = \frac{1}{\pi} \int_{-\pi}^{\pi} y(t) \cos(\omega t) d(\omega t)$$
$$b_1 = \frac{1}{\pi} \int_{-\pi}^{\pi} y(t) \sin(\omega t) d(\omega t) \qquad (2.30)$$

With the assumptions applied to the Fourier series, the output signal denoted by Equation 2.28 reduces to:

$$y(t) \approx a_1 \cos(\omega t) + b_1 \sin(\omega t) = M \sin(\omega t + \phi) \qquad (2.31)$$

it follows that:

$$M(A, \omega) = \sqrt{a_1^2 + b_1^2} \qquad (2.32)$$

and

$$\phi(A, \omega) = \tan^{-1}(\frac{a_1}{b_1}) \qquad (2.33)$$

Using basic definitions of frequency domain analysis, shows that the DF block can represented by the ratio between the output (Equation 2.31) and input (Equation 2.27) signals:

$$N(A, \omega) = \frac{y(t)}{u(t)} = \frac{M \sin(\omega t + \phi)}{A \sin(\omega t)} \qquad (2.34)$$

in complex notation the above reduces to:

$$N(A, \omega) = \frac{Me^{j(\omega t + \phi)}}{Ae^{j\omega t)}} = \frac{M}{A} e^{j\phi} = \frac{1}{A}(b_1 + ja_1) \qquad (2.35)$$

Finally, an expression for the nonlinear element used in Figure 2.5 is produced, that depends on the Fourier coefficients a_1 and b_1. Keep in mind that the input signal's frequency and amplitude both affect the general DF. For the nonlinear elements in trimmer dynamics, backlash and Coulomb friction, the DF only depends on input amplitude, i.e. $N(A, \omega) \rightarrow N(A)$, as shown in the upcoming sections.

Now that the assumptions and definitions of the DF are defined, the Fourier coefficients affecting the DF must be derived. It is necessary to compute the integrals Equation 2.30 to acquire these coefficients. Numerical integration technique is usually used to find these coefficients, where the input-output relationship of a particular nonlinearity is well-defined over a periodic domain.

2.3.4 Computation of Backlash DF in Trimmer Dynamics

Play/backlash nonlinearities mainly exist in transmission systems. It is common to leave small gaps between interconnected elements to avoid that the interconnected elements break when moving. In addition to the fact that mechanical systems are designed that way, manufacturing errors can cause

backlash as well.

Deriving the DF for backlash will be made easier by visualising the idea of backlash. Consider the motor shown in Figure 2.7 which is in oscillating motion. For now the mass of the load is considered weightless $M = 0$. In literature this is called friction-controlled backlash since the load has no inertia since it was assumed that it had no weight. This is the most common form of backlash. If
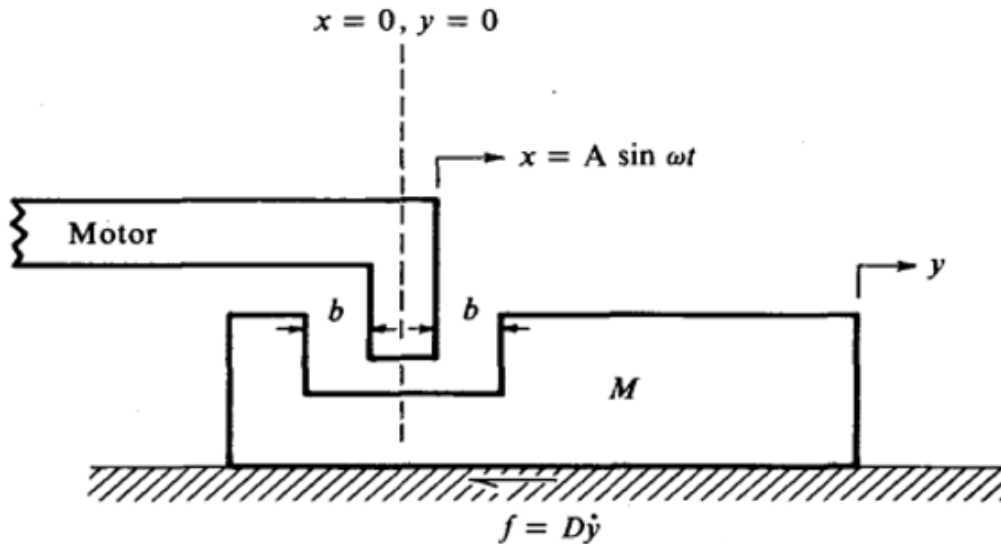
Figure 2.7: Oscillating motor driving a viscous friction plus inertia load through a linkage with backlash b. Image retrieved from book of Gelb [1].

the amplitude of the oscillating motion of the motor is less than $A < b$, the edges of the load are never in contact with the motor. Therefore the load is not in motion, corresponding to segment OA in Figure 2.8. When increasing the amplitude of the motor to values $A \geq b$, the load and motor will establish contact and the load will follow the motion of the motor in linear fashion[4], corresponding to segment AB in Figure 2.8.

This virtual representation can be translated to trimmer dynamics, by considering the motor as the eccentric pin and the load as the driving bridge, where backlash exists between the two.

The oscillating motion of the pin ensures that the pin reverses direction at some point in time. When this happens, the pin and the driving bridge are separated, and since the assumption states the the driving bridge has no inertia, the driving bridge does not move [5]. Once the pin has overcome the backlash width of $2b$, contact is reestablished with the driving bridge, shown by segment BC in Figure 2.8: This repeating pattern, caused by periodic motion, forms a closed path EBCD shown in the graph Figure 2.8. The shape of the path, or height of B, C, D and E depends on the input amplitude corresponding to the eccentric pin. Additionally, from the closed path it can be seen that backlash is a multi-valued element by nature. This means that there for a given input, two output values are possible. The nonlinear element has in some sense a certain 'memory'. Multi-valued nonlinearities lead to energy storage in the system. Energy storage is a frequent cause of instability or self-sustained oscillation [2].

In dealing with backlash, the following two limiting cases are considered. The first case considers that the frictional forces on the load are dominant or $M = 0$, this corresponds to the analyse of the i/o-relations above. Secondly, inertia forces are dominant ($D = 0$ in Figure 2.7 or $M \neq 0$), this is called: inertia-controlled backlash. Combining the two limiting cases lead to so-called: viscous-controlled backlash [1], where $M \neq 0$ and $D \neq 0$. The latter case reflects to more realistic backlash scenario

---

[4]This is applicable for friction-controlled backlash

[5]Only applies to to friction-controlled backlash as seen in the following sections
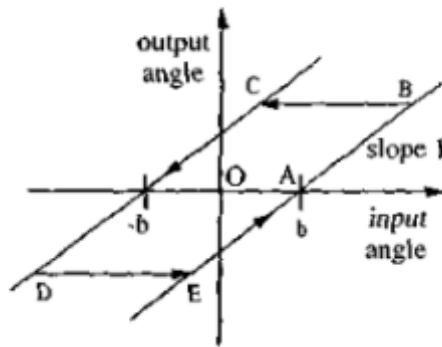
Figure 2.8: Backlash nonlinearity input/output relation. Image retrieved from book of Slotine [2].

since driving bridge has some inertia and there is also some friction between the cutter and guard. In fact, the frictional forces are dominant for trimmer dynamics, as we'll see in the upcoming sections.

Friction-controlled backlash
In the first case, it is assumed that the load only moves whenever contact between motor and load is established. Whenever the motor is reversing direction, the load is not moving since it was assumed that the load had zero inertia $M = 0$.
I/o-relation for fiction-controlled backlash with sinusoidal input, is shown in Figure 2.9. When the pin and driving bridge are in contact, there is a linear relationship between their motion, therefore the slope is $k = 1$. The total backlash gap the pin has to overcome to reestablish contact with the driving bridge is denoted by $2b$. Based on the input wave and the graphical representation of backlash, the 'backlashed output' signal from Figure 2.9 can be obtained in piece-wise manner. Then this piece-wise signal for $y(t)$ is used to derive the Fourier coefficients, which in turn are used to achieve the DF for the backlash nonlinearity. Assume that $A \geq b$ and observe that indeed the output signal $y(t)$ can be split into four distinct regions over one period, shown by the backlashed output signal in Figure 2.9. For simplicity the period starts at $\omega t = \frac{\pi}{2}$ and ends ate $\omega t = \frac{5\pi}{2}$. The output signal initially (value $\geq \frac{\pi}{2}$), has a constant value of $-(A - b)$. Once contact is reestablished at angle $\omega t = \pi - \gamma$, the output signal will follow the input signal but is shifted by the amount of backlash b. When the input reverses direction, and separates with the driving bridge, the output signal remains constant with value: $(A - b)$. Once contact has been reestablished again, the output signal follows the input signal, but is shifted by $-b$. This leads to a piece-wise function for the backlashed output signal $y(t)$, denoted by Equation 2.36.

$$y(t) = \begin{cases} -(A - b) & \text{if } \frac{\pi}{2} < \omega t \leq \pi - \gamma \\ (A\sin(\omega t) + b) & \text{if } \pi - \gamma < \omega t \leq \frac{3\pi}{2} \\ (A - b) & \text{if } \frac{3\pi}{2} < \omega t \leq 2\pi - \gamma \\ (A\sin(\omega t) - b) & \text{if } 2\pi - \gamma < \omega t \leq \frac{5\pi}{2} \end{cases} \tag{2.36}$$
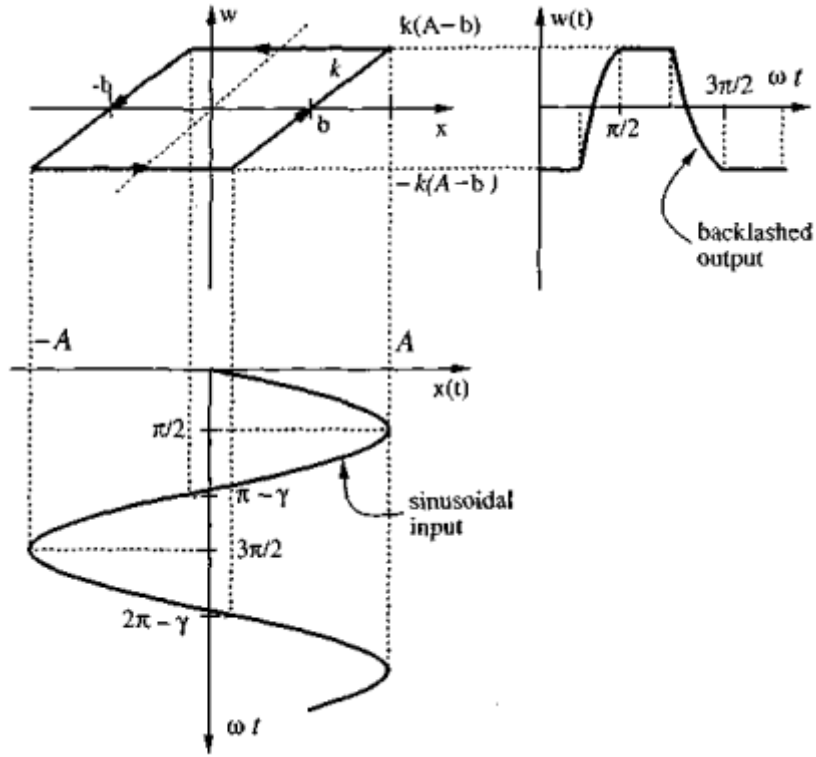
Figure 2.9: Input-output relation backlash operator. Top left: shows backlash i/o-relation. Bottom: shows sinusoidal input to backlash element. Top right: shows the output obtained by tracing the corresponding lines between input and backlash element. Image retrieved from book of Slotine [2].

where $\gamma = \sin^{-1}(1 - 2b/A)$. According to the piece-wise output values, the Fourier coefficients of Equation 2.30 are calculated. For the a_1, the Fourier integral becomes:

$$a_1 = \frac{1}{\pi} \underbrace{\int_{\pi/2}^{\pi-\gamma} -(A - b) \cos(\omega t) d(\omega t)}_{=\frac{2b(b-A)}{A}}$$

$$+ \frac{1}{\pi} \underbrace{\int_{\pi-\gamma}^{3\pi/2} (A \sin(\omega t) + b) \cos(\omega t) d(\omega t)}_{=0}$$

$$+ \frac{1}{\pi} \underbrace{\int_{3\pi/2}^{2\pi-\gamma} (A - b) \cos(\omega t) d(\omega t)}_{=\frac{2b(b-A)}{A}}$$

$$+ \frac{1}{\pi} \underbrace{\int_{2\pi-\gamma}^{\frac{5\pi}{2}} (A \sin(\omega t) - b) \cos(\omega t) d(\omega t)}_{=0}$$

(2.37)

leading to:

$$a_1 = \frac{1}{\pi} \left[\frac{2b(b - A)}{A} + 0 + \frac{2b(b - A)}{A} + 0 \right]$$

$$a_1 = \frac{4b}{\pi} \left(\frac{b}{A} - 1 \right)$$

(2.38)

To obtain the Fourier coefficient of b_1, the same piece-wise values of $y(t)$ are used, leading to:

$$b_1 = \frac{1}{\pi} \underbrace{\int_{\pi/2}^{\pi-\gamma} (A-b)\sin(\omega t)d(\omega t)}_{=2(A-b)\sqrt{\frac{b(A-b)}{A^2}}}$$

$$+ \frac{1}{\pi} \underbrace{\int_{\pi-\gamma}^{3\pi/2} (A\sin(\omega t)+b)\sin(\omega t)d(\omega t)}_{=\frac{1}{4}A\left(-4\sqrt{\frac{b(A-b)}{A^2}}+2\sin^{-1}\left(1-\frac{2b}{A}\right)+\pi\right)}$$

$$+ \frac{1}{\pi} \underbrace{\int_{3\pi/2}^{2\pi-\gamma} -(A-b)\sin(\omega t)d(\omega t)}_{=2(A-b)\sqrt{\frac{b(A-b)}{A^2}}}$$

$$+ \frac{1}{\pi} \underbrace{\int_{2\pi-\gamma}^{\frac{5\pi}{2}} (A\sin(\omega t)-b)\sin(\omega t)d(\omega t)}_{=\frac{1}{4}A\left(-4\sqrt{\frac{b(A-b)}{A^2}}+2\sin^{-1}\left(1-\frac{2b}{A}\right)+\pi\right)}$$

(2.39)

so b_1 is:

$$b_1 = \frac{A}{\pi}\left[\frac{\pi}{2} - \sin^{-1}\left(\frac{2b}{A}-1\right) - \left(\frac{2b}{A}-1\right)\sqrt{1-\left(\frac{2b}{A}-1\right)^2}\right] \tag{2.40}$$

From these coefficients, the DF for friction-controlled backlash is achieved, according to $N(A) = \frac{1}{A}(b_1 + ja_1)$:

$$a_1 = \frac{4b}{\pi}\left(\frac{b}{A}-1\right)$$

$$b_1 = \frac{A}{\pi}\left(\frac{\pi}{2} - \sin^{-1}\left(\frac{2b}{A}-1\right) - \left(\frac{2b}{A}-1\right)\sqrt{1-\left(\frac{2b}{A}-1\right)^2}\right) \tag{2.41}$$

This result is used to solve for the condition of harmonic balance Equation 2.25. The limitations of this condition will be discussed in subsection 2.3.6. It is worth noting that,

- the DF for friction-controlled backlash is frequency independent since neither a_1 or b_1 is frequency dependent

- the DF has imaginary part since $a_1 \neq 0$ leading to to a complex-valued DF

Inertia-controlled backlash
In the above, the total backlash width was considered to be of value $2b$, here the total width is considered to be of value b. In contrary to the previous derivation for backlash, where it was assumed that the driving bridge had no inertia $M = 0$, it is now assumed that the driving bridge does have inertia, but is not subjected to frictional forces hence $D = 0$. I/o-relation for this specific backlash, is characterised by Figure 2.10. From the i/o wave characteristics, it can be shown that the output signal reaches maximum velocity at $\phi = n\pi$, where $n = 0, 1, 2, \dots$. At these values motor imparts to the load with corresponding value. The motor oscillates according to: $u(t) = A\sin(\omega t)$, so for integer values of π, the output signal takes the $u'(n\pi) = A\omega\cos(\omega n\pi) = A\omega$. After that, motor-load separation occurs, and the driving bridge will travel with constant velocity until contact between the pin and driving bridge is reestablished. Here, it is assumed that there is no 'bouncing' between the pin and driving
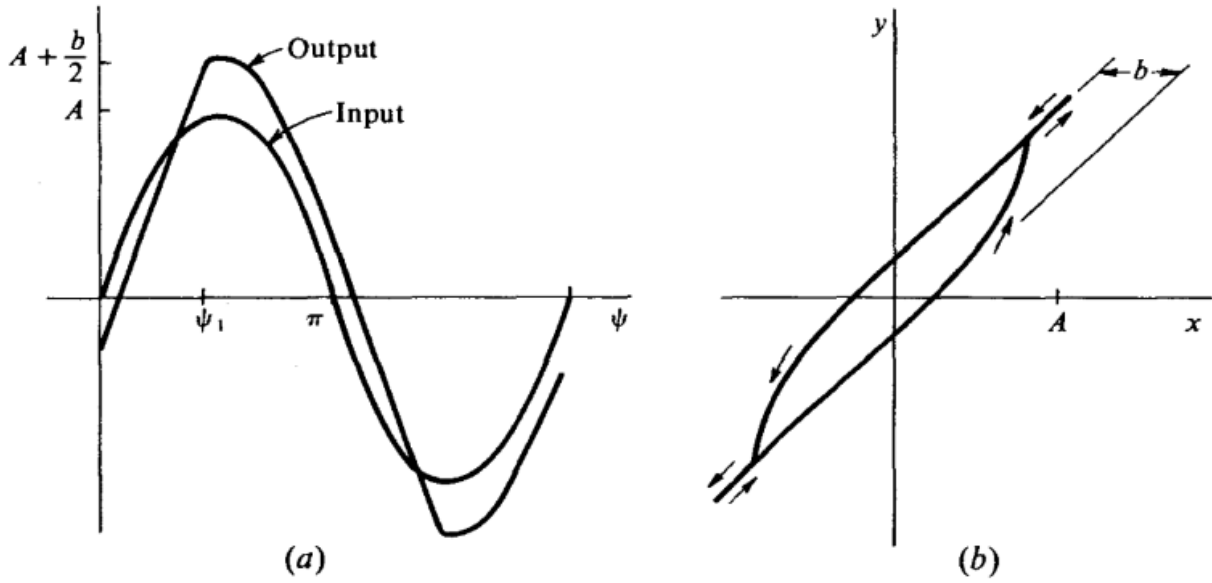
Figure 2.10: Inertia controlled backlash. (a) Waveforms for inertia controlled backlash. (b) Equivalent backlash characteristic. Image retrieved from book of Gelb [1].

bridge during impart. The piece-wise backlashed output signal $y(t)$ for inertia-controlled backlash is derived similarly to friction-controlled backlash. Consider the output wave denoted in Figure 2.10. For the first interval $0 < t \leq \phi$, output signal has linear motion with a value corresponding to the maximum velocity of the input wave since the driving bridge does not feel any frictional resistance, hence $y(t) = \omega A t - \frac{b}{2}$. Once the eccentric pin has overcome the backlash width, the output signal moves linearly with the input wave until the input wave has reached its maximum velocity, which is achieved at $t = T/2$. So the backlashed output wave has a value of: $y(t) = u(t) + \frac{b}{2}$, during $\phi < t \leq T/2$. For the adjacent interval driving bridge will travel with negative maximum constant velocity again. Finally, driving bridge and motor will collide again and output signal traces input signal again. The piece wise values of the output signal are listed in Equation 2.42:

$$
y(t) = \begin{cases}
\omega A t - \frac{b}{2} & \text{if } 0 \leq t < \phi \\
u(t) + \frac{b}{2} & \text{if } \phi \leq t < \frac{T}{2} \\
\omega A \cos(\omega \frac{T}{2})(t - \frac{T}{2}) & \text{if } \frac{T}{2} \leq t < \frac{T}{2} + \phi \\
u(t) - \frac{b}{2} & \text{if } \frac{T}{2} + \phi \leq t < T
\end{cases}
\tag{2.42}
$$

The angle $\phi = \omega t$, at which the motor and driving bridge reestablish contact, can be derived by the equating to piece-wise signal just before this angle with the piece-wise function after this angle, such that:

$$
\omega A t - \frac{b}{2} = u(t) + \frac{b}{2} = A \sin(\phi) + \frac{b}{2}
$$
$$
A\phi - A \sin(\phi) - b = 0
$$
$$
\phi - \sin(\phi) - \frac{b}{A} = 0
$$

Unfortunately, there is no exact solution for this equation, therefore numerical solutions have to be computed for the ratio of b/A. Similar to friction-controlled backlash the Fourier coefficients are a direct consequence of the piece-wise function for the backlashed output signal of $y(t)$, resulting in the

inertia-controlled backlash DF, denoted by:

$$N(A) = \frac{1}{\pi}(\pi + 2\sin(\phi_1) - \phi_1 - \sin(\phi_1)\cos(\phi_1)) - j\frac{1}{\pi}(1 - \cos(\phi_1))^2) \qquad (2.43)$$

where $\phi_1 = \sin(\phi_1) + \frac{b}{A}$. Here it is worth noting that the imaginary part has negative sign, whereas it has positive sign for friction-controlled backlash.

Viscous-controlled backlash
In the previous two cases, either friction or inertia was assumed to be zero. When friction and inertia coexist, the backlash component is more realistic, this is known as viscous-controlled backlash. Figure 2.11 shows the i/o wave characteristics for viscous-controlled backlash. In Figure 2.11, the
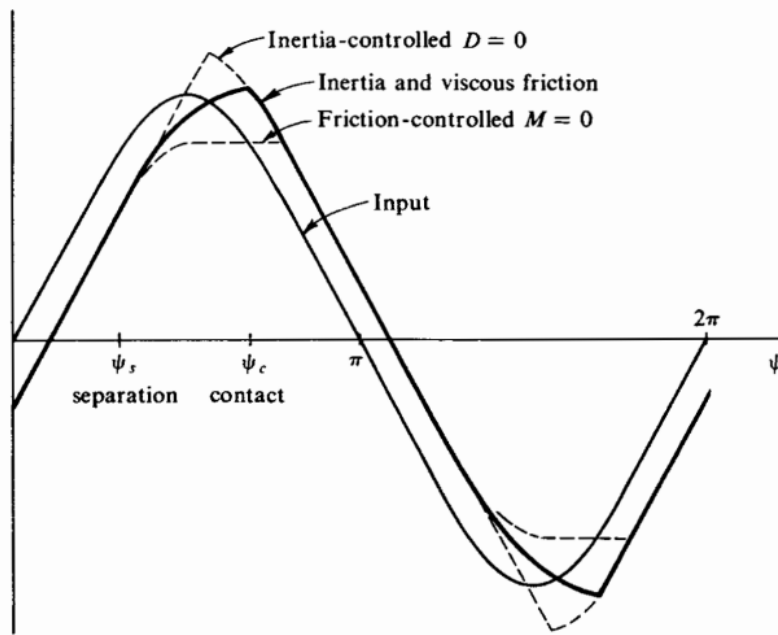
Figure 2.11: Viscous-controlled backlash waveform. Image retrieved from book of Gelb [1].

angle ϕ_s denotes the motor load separation point and ϕ_c denotes the angle at which the motor and load reestablish contact. The velocity of motor and load, pin and driving bridge respectively, are identical up till an angle of ϕ_s. This fact makes it possible to conclude that [1]:

$$\phi_s = \tan^{-1}\left(\frac{1}{\gamma}\right) \qquad (2.44)$$

where γ is the ratio of the inertia over the friction multiplied with the input frequency. In other words:

$$\gamma = \frac{M}{D}\omega \qquad (2.45)$$

Since γ depends on the frequency, the DF itself will be a frequency dependent DF. The contact angle can be obtained according to:

$$\sqrt{1 - \gamma^2} - \frac{b}{A} = \sin(\phi_c) + \frac{\gamma^2 e^{(1/\gamma)(\tan^{-1} 1/\gamma - \phi_c)}}{\sqrt{1 + \gamma^2}} \qquad (2.46)$$

From the i/o wave characteristics shown by Figure 2.11, the viscous-controlled DF is derived. Derivation of this complex DF is done in the book of A. Gelb [1]. Resulting in a complex, frequency dependent

DF, such that: $N(A, \omega)$. In complex gain notation, the DF is defined as:

$$N(A, \omega) = n_p(A, \omega) + jn_p(A, \omega) \tag{2.47}$$

where $n_p(A, \omega)$ and $n_q(A, \omega)$ are listed in Appendix B.2.

The take away from this section is that backlash nonlinearity, can be modelled according to friction-, inertia- or viscous-controlled backlash DF. Whereas the former two are two limiting cases. The results from these limiting cases will be presented in chapter 5.

2.3.5   Coulomb friction DF in Trimmer Dynamics

Besides the backlash nonlinearity, the trimmer consists of an additional nonlinearity which is friction. This results from friction between the cutter and guard. That comes as a result of the spring, shown in Figure 2.1a, pressing the cutter to the guard necessary to accurately trim hair that is in between. As a consequence, the relatively high normal force N induces a frictional force since $F_c = \mu N$.
A widely used model for friction is the model of Coulomb friction [11]. This model has the advantage that is is well-suited for DF theory, since it can be considered as a quasi-linear nonlinearity. In other words, the fictional value switches between two limiting cases. Classic Coulomb friction, with a discontinuity, is represented by [12]:

$$F(\dot{x}) = F_c sign(\dot{x}) \tag{2.48}$$

Here, F_c is the Coulomb friction coefficient multiplied by a sign operator. It follows that Coulomb friction can be decomposed piece-wisely, according to:

$$F(\dot{x}) = \begin{cases} F_c & \text{if } \dot{x} > 0 \\ 0 & \text{if } \dot{x} = 0 \\ -F_c & \text{if } \dot{x} < 0 \end{cases} \tag{2.49}$$

Equation 2.49 can also be considered as an ideal relay with instantaneous switching upon change of the input velocity. Based on the input of trimmer dynamics the input velocity is constantly changing due to periodic motion. This makes it possible to apply the ideal relay-based sinusoidal DF approach for Coulomb friction.
An ideal relay can be considered as an on-off nonlinearity, shown in Coulomb friction plot by Figure 2.12. Assuming a sinusoidal input is subjected to the Coulomb friction nonlinearity, can lead to the Coulomb friction DF. Unlike backlash, the nonlinearity here is actually velocity dependent instead of displacement. But since the it was assumed that the input displacement was an oscillating function, the derivative of that function is also a sinusoidal function. For computational reasons, the same sinusoidal input function is used to compute the DF for Coulomb friction [6].
Starting by deriving the first Fourier coefficients for a_1 and b_1 defined by Equation 2.30, with the potential output forces defined by Equation 2.49. So, if the input has positive velocity, the output will be a constant value of $+F_c$. On the other hand, if the input velocity is negative the output has constant value of $-F_c$. Because the pin is in oscillating motion, it will encounter both positive and negative Coulomb friction values over a period of 1 oscillation. Leading to the Fourier coefficient a_1:

$$a_1 = \frac{1}{\pi} \underbrace{\int_0^\pi F_c \cos(\omega t) d(\omega t)}_{=0} + \frac{1}{\pi} \underbrace{\int_\pi^{2\pi} -F_c \cos(\omega t) d(\omega t)}_{=0} \tag{2.50}$$

$$a_1 = 0$$

---

[6]All sinusoidal function lead to the same DF, when scaling is applied
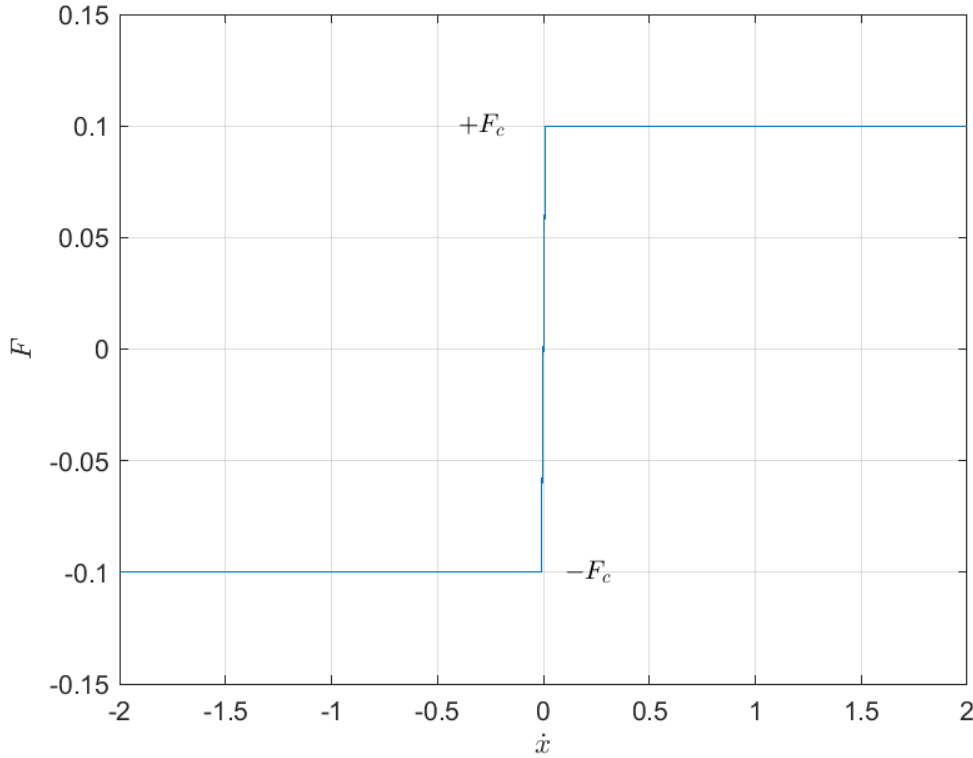
Figure 2.12: Example of Coulomb friction, based on an ideal relay

this immediately tells that the DF for Coulomb friction is purely real since $N(A, \omega) = \frac{1}{A}(b_1 + ja_1)$. In contrast, the real part of the DF, b_1, is not equal to zero since:

$$
\begin{aligned}
b_1 &= \frac{1}{\pi} \int_0^\pi F_c \sin(\omega t) d(\omega t) + \frac{1}{\pi} \int_\pi^{2\pi} -F_c \sin(\omega t) d(\omega t) \\
b_1 &= \frac{2}{\pi} \int_0^\pi F_c \sin(\omega t) d(\omega t) = \frac{2F_c}{\pi} \left[-\cos(\pi) - \cos(0) \right] \\
b_1 &= \frac{4F_c}{\pi}
\end{aligned}
\tag{2.51}
$$

According to Equation 2.35, this results in the Coulomb DF as:

$$
N(A) = \frac{4F_c}{A\pi}
\tag{2.52}
$$

In the upcoming section, it will be shown that intersections between the transfer function $G(j\omega)$ and the negative inverse of the DF $-1/N(A)$ lead to the prediction of limit cycles. Therefore it should be noted that the the negative inverse of the Coulomb DF is strictly real and negative. Indicating that the transfer function must intersect with the negative real axis to predict limit cycling behaviour based on Coulomb friction.

2.3.6 Describing Function Analysis of Nonlinear Systems

The preceding sections introduced the concept of DF's for the nonlinear elements for trimmer dynamics. In essence that means that the nonlinear element can be approximated by a frequency response function based on the Fourier expansion. This quasi-linearised technique can be applied to linear

control theory to predict the existence of limit cycles.

Limit cycle prediction
The quasi-linearised block diagram shown in Figure 2.5 indicates that the loop transfer function results in the condition for harmonic balance, as shown before. That is:

$$N(A, \omega)G(j\omega) + 1 = 0$$

Any solution(s) of this condition predicts a limit cycle with amplitude A and frequency ω. Solutions of the condition can be obtained algebraically or graphically. Algebraically, the condition has to be rewritten in terms of real and imaginary parts. Rewriting the above in real and imaginary parts, where $N(A, \omega) = \text{Re}(N(A, \omega)) + j\text{Im}(N(A, \omega))$ and $G(j\omega) = \text{Re}(G(j, \omega)) + j\text{Im}(G(j, \omega))$, lead to:

$$\text{Real}: \qquad \text{Re}N(A, \omega))\text{Re}(G(j, \omega)) - \text{Im}(N(A, \omega))\text{Im}(G(j, \omega)) = -1 \qquad (2.53)$$

$$\text{Imag}: \qquad \text{Im}(N(A, \omega))\text{Im}(G(j, \omega)) + \text{Im}(N(A, \omega))\text{Re}(G(j, \omega)) = 0 \qquad (2.54)$$

The set of consists of two equations with two unknowns, that will solve for the limit cycle amplitude A_{lc} and frequency of the limit cycle ω_{lc}, where the Real set solves for the amplitude and the imaginary set solves for the frequency. In general it is very difficult to solve these equations analytically, especially for high-order system like trimmer dynamics. Therefore the analytic solutions are performed by Matlab.
Another, more widely used and feasible approach, a graphical approach. The idea results from rewriting the condition for harmonic balance, such that:

$$G(j\omega) = -\frac{1}{N(A, \omega)} \qquad (2.55)$$

Plotting the right-hand side of together with the left-hand side of Equation 2.55 on the complex and observe if intersections between the two occur. If the two curves intersect, limit cycling behaviour is predicted.
For friction-, inertia-controlled backlash, and for Coulomb friction the DF is a frequency-independent function: $N(A, \omega) \rightarrow N(A)$ hence:

$$G(j\omega) = -\frac{1}{N(A)} \qquad (2.56)$$

Plotting $G(j\omega)$ for varying ω and plotting $N(A)$ for varying amplitude A, leads two the two curves on the complex plane. It is necessary to identify the increasing direction of A and ω of the two curves while analysing the stability of the anticipated limit cycle, as derived shortly. As an example consider the plot shown byFigure 2.13. For this particular example the DF is frequency independent. A limit cycle exists at point K, with an amplitude that is found by solving $-1/N(A)$ at that point. Whereas the frequency of that limit cycle is found by solving $G(j\omega)$ for ω at K.

Stability of limit cycles
If a limit cycle is predicted, either algebraically or graphically, the next step is to determine if the predicted limit cycle is (un)stable
From the Nyquist stability criterion, it is known that in order for the open-loop system to be stable, the closed-loop system is must be stable. This provides the critical point $(-1, 0)$ to lie to the left of the Nyquist locus. All the intersecting points between $-1/N(A)$ and $G(j\omega)$, can be thought of as critical points. With that in mind, consider the following example, shown in Figure 2.14. This plot shows that for this particular system 2 intersections between the curves exist, indicating that there are 2 limit cycles present in this system. The first limit cycle occurs at point L_1 with amplitude A_1 and frequency ω_1, while the second limit cycle occurs at point L_2 with amplitude A_2 and frequency ω_2. As mentioned previously, the increasing direction of A, corresponding to $-1/N(A, \omega)$, has to be taken into account.
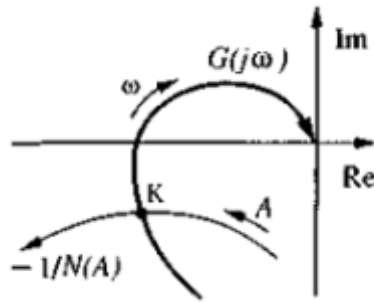
Figure 2.13: Graphical representation of the condition of harmonic balance: $G(j\omega) = -\frac{1}{N(A)}$. Image retrieved from book of Gelb [1].
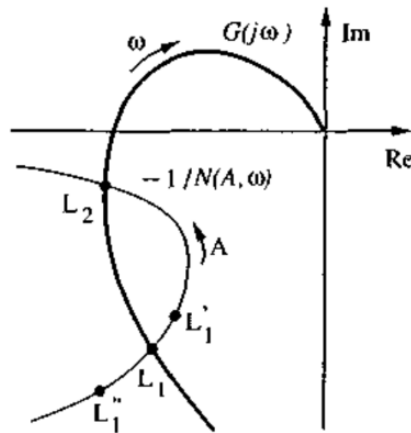
Figure 2.14: Graphical determination of the stability of a limit cycle. Image retrieved from book of Gelb [1].

In doing so, it is clear that the value of $A_1 \leq A_2$. A small perturbation in the positive direction of A_1, shift to corresponding operation point $L_1 \rightarrow L_1'$. Because this slightly perturbed operating point is now encircled by the curve of $G(j\omega)$, the perturbed operating point is considered to be unstable base on the extension of the Nyquist stability criterion. The perturbed operating point corresponding to L_1 will then grow in amplitude by absorbing energy, and thus continues to move along the curve of $-1/N(A)$ until the operating point merges to the operating point corresponding to the other limit cycle denoted by L_2. On the other hand, a small perturbation in the negative direction of A shift the operating point $L_1 \rightarrow L_1''$, which lies outside the encircle curve of $G(j\omega)$, which is considered the stable region and thus the system tries to attenuate/shrinking the amplitude by dissipating energy corresponding to the new operating point L_1''. Therefore the limit cycle corresponding to L_1 is unstable. Similar analyse shows that the limit cycle corresponding to L_2 is stable.

Some of the results presented and analysed in chapter 5, in fact show the coexistence of two limit cycles based on similar graphical approach, but indeed the output of the overall model results in the observation of only the stable limit cycle, corresponding to L_2 in this example.

2.4   Treatment of multiple nonlinearities

So far, only single nonlinearities in a closed loop configuration have been considered. However, for complex system such as trimmers, there are usually multiple nonlinearities in the system, as shown in the preceding sections. The work of A. Gelb [1], showed that an extension of the DF can be applied the systems containing multiple nonlinearities. Since backlash and Coulomb friction are ever present in trimmer dynamics, there are at least two nonlinearities for trimmer dynamics. A generalised cascaded model was proposed. However, the cascaded model only applies to systems where both nonlinearities are either positional dependent or velocity dependent [13]. Unfortunately, this does not apply to backlash and Coulomb friction, which depend on position or velocity, respectively. Hence this proposed cascaded model does not apply to trimmer dynamics. An alternative method has to be derived.

Equivalent nonlinearity
A so-called 'equivalent nonlinearity' is proposed [3]. This method stated the for a combination of the nonlinearities, with either position and velocity dependency parallel configuration can be obtained. Therefore a parallel configuration between backlash and Coulomb friction is required, where the latter is adjusted with an integrator such that both nonlinearities have equivalent dependencies, namely: position. The nonlinearity, that is expected to cause limit cycling behaviour, is known as the 'intentional' nonlinearity denoted by $N_r(A)$. Whereas the Coulomb friction between the cutter and guard, is known as the inherent nonlinearity, denoted by $N_f(A)$. An example of this parallel configuration is shown in Figure 2.15.
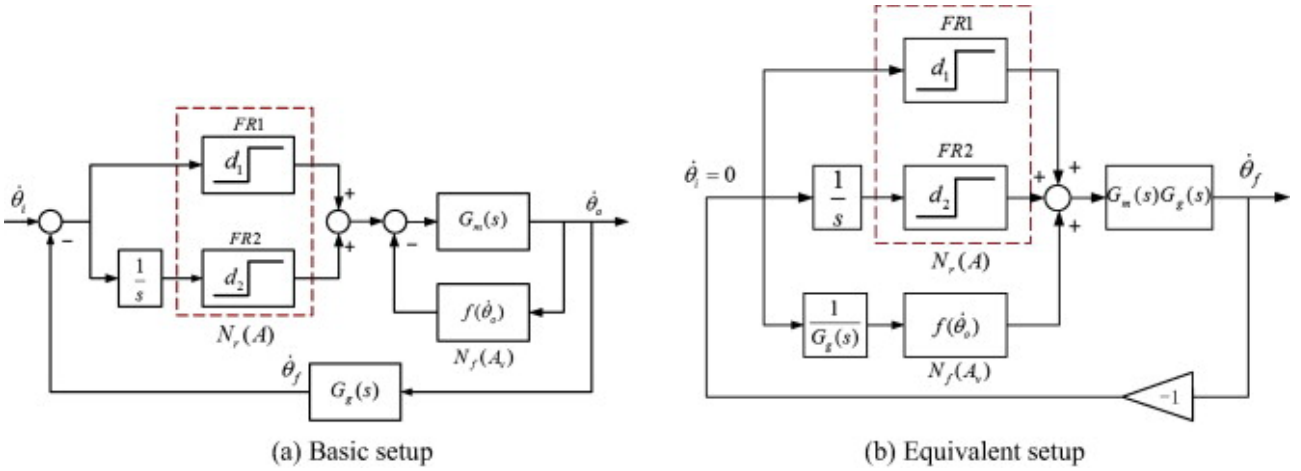
Figure 2.15: Example of parallel configuration, obtained from the study of Chen [3].
(a) displays the basic setup with inherent nonlinearity (Coulomb friction) in feedback wit the linear transfer function $G_m(s)$, subjected to an intentional nonlinearity (backlash). (b) displays the equivalent configuration from which the DF is derived.

In Figure 2.15, $G_g(s)$ denotes the intentional low-pass digital filter cascaded with the linear transfer function for trimmer dynamics, denoted by $G_m(s)$, to increase the order of the model so as to ensure the availability of DF method. That is, when the system moves sinusoidally, the amplitude of a limit cycle after filtered, denoted as A, can be derived as the product of the amplitude of velocity sinusoidal response amplitude A_v and the norm of the frequency response function of the low-pass filter $|G_g(j\omega)|$, and the relationship among them is $A = Av|G_g(j\omega)|$. If a self-sustained oscillations exist, in the parallel configuration shown by Figure 2.15(b), the condition for harmonic balance for this equivalent system is satisfies the following relation:

$$N_{eq}(A,\omega)G_{eq}(j\omega) + 1 = 0 \tag{2.57}$$

Figure 2.15(b) shows that the equivalent linearity of the transfer function is the product denoted as $G_{eq}(s) = G_m(s)G_g(s)$ and the equivalent nonlinearity $N_{eq}(A, \omega)$ is the sum of intentional nonlinearity for backlash $N_r(A)$ and the inherent nonlinearity for Coulomb friction $N_f(A)$, where the latter is adjusted by $1/G_g(s)$. Thus, the DF for the equivalent nonlinearity can be expressed as:

$$N_{eq}(A, \omega) = N_r(A) + \frac{1}{G_g(j\omega)} N_f(A) \tag{2.58}$$

For the sake of simplicity it is assumed that the intentional nonlinearity $N_r(A)$ is dominated by fiction-controlled backlash, instead of inertia-, or viscous-controlled backlash. The results for this DF are derived in subsection 2.3.4 as:

$$N_r(A) = \frac{1}{A} \left(\frac{\pi}{2} - \sin^{-1}\left(\frac{2b}{A} - 1 \right) - \left(\frac{2b}{A} - 1 \right) \sqrt{1 - \left(\frac{2b}{A} - 1 \right)^2} \right. $$
$$\left. + j \frac{4b}{\pi} \left(\frac{b}{A} - 1 \right) \right) \tag{2.59}$$

and for the inherent nonlinearity corresponding to Coulomb friction, the DF was derived in subsection 2.3.5 as:

$$N_f(A) = \frac{4F_c}{A\pi} \tag{2.60}$$

Plugging Equation 2.59 and Equation 2.60 into the expression for Equation 2.58 yields the equivalent nonlinearity. It must be noted that the equivalent DF, containing friction-controlled backlash and Coulomb friction, is amplitude A and frequency ω dependent, whereas the constituent nonlinearities are only amplitude dependent. In addition, it was assumed the intentional nonlinearity is friction-controlled backlash rather than inertia-, or viscous-controlled backlash since the spring force pressing the cutter to the guard is considered to be relatively high. In other words, the driving bridge is only in motion if and only if the oscillating eccentric pin is in contact with the driving bridge. Moreover, the DF for the equivalent nonlinearity is already fairly complex for friction-controlled backlash, and the inclusion of inertia makes it even more complex.

Chapter 3

Experimental setup and simulation modelling setup

This chapter gives a brief description of the experimental setup performed in cooperation with Philips Drachten. In advance the data obtained from these experiments, is compared to data obtained from identical simulink models. Simulink is a block diagram environment for multi domain simulation and Model-Based Design. Such that the model can be created according to physical blocks derived for the DF method.

3.1 Experimental setup

First, a description of the experimental setup is provided to acquire trimmer data for the purpose of validating the output from the simulink models. In particular the relative motion between the cutter and guard is measured by means of a high-speed camera since the output map in state-space representation is defined as: $y = x_4 - x_2$. Two experiments are performed, one with and one without backlash between the driving bridge and the eccentric pin.

The motion between the cutter and guard is captured by a high-speed camera in terms of frames. The frames per second (fps) rate is the number of frames captured in a given amount of time. There is a certain trade-off here because increasing the fps rate also increases the amount of data and hence the computing time. The high-speed camera utilised for these studies has a maximum rate of 1 million fps. A sampling rate of $F_s = 20[\text{kHz}]$ is chosen for this experiment. This translated to $N = 2000$ frames when measured over a 0.1-second time span. The accuracy of the experiment may be determined from the sampling rate and the number of frames by using the experiment's frequency resolution [14], denoted by Equation 3.1.

$$\Delta f = \frac{F_s}{N} \tag{3.1}$$

Consequently, this experiment's frequency resolution is: $\frac{20000}{2000} = 10[\text{Hz}]$. As a result, it is anticipated that the FFT's peaks will have a specific width due to the measurement's inherent inaccuracy, which results from the frequency resolution of $\Delta f = 10[\text{Hz}]$. The driving frequency should be represented by at least one peak on the FFT, and it may also display any harmonics that are related to that frequency. Since DF predicts a limit cycle in the second experiment with backlash, it is expected that the FFT will also contain an extra peak that does not match to a harmonic.[1].

Appendix C shows all relevant information regarding the experiment performed in cooperation with Philips Drachten. Some of the results are confidential and therefore it is not allowed to distribute the information listed in the Appendix C.

The general setup used for this experiment is shown in Appendix C.2 by Figure C.1. Two light

---

[1]limit cycle only exist if backlash a reached a certain width

sources are used to illuminate the fixed trimmer. Precisely in the middle of the two light sources is where the high-speed camera is positioned. The position of the cutter and cutter guard for each frame is determined utilising the related software: Photron FASTCAM viewer. To determine the relative motion between the cutter and guard, this program needs careful calibration. The calibration is achieved by placing a ruler directly behind the trimmer, where the length scale of the ruler is obviously known, shown in Figure C.2. The user must then specify two reference locations for tracking. One point is chosen on the cutter knife and one on the guard knife, indicated by the green boxes in Figure C.2. After that, the program will automatically transform the cutter's and guard's positions in relation to their reference point to data. Matlab may then be used to analyse this data.

3.2   Results from experiment

In the previous chapter, the experimental setup for analysing the motion of trimmer dynamics was given. Now the results form these experiments are analysed. As mentioned, two experiments are performed, one without and another with a small backlash gap. Three trials are included in each experiment to reduce to effect of errors.

Experiment 1, without backlash
The results for the experiment with $b = 0$[m], are shown in Figure 3.1.
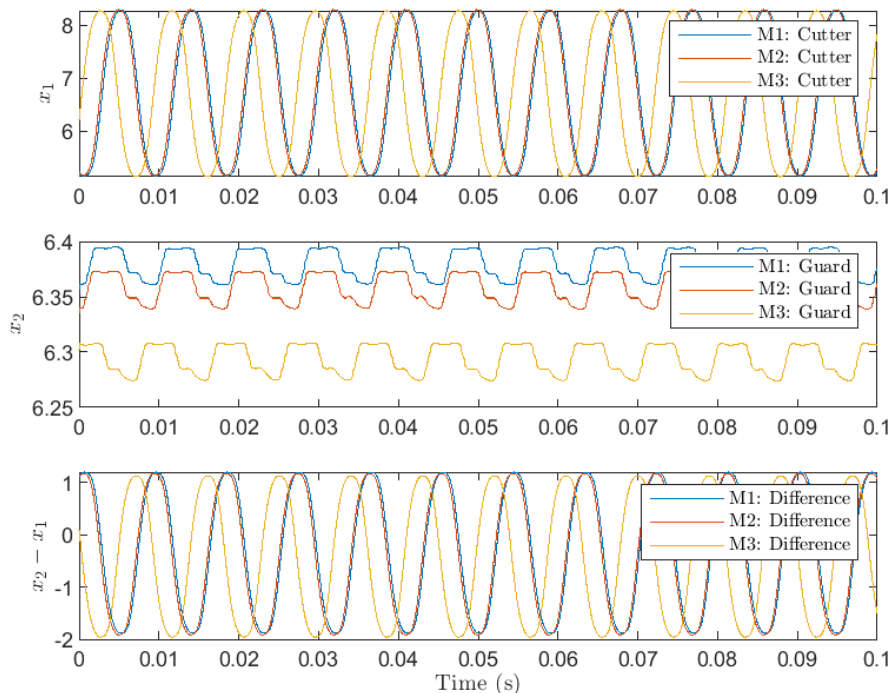
Figure 3.1: Results for 3 measurements for first experiment. Top: motion of cutter, middle: motion of guard and bottom: difference between cutter and guard

When comparing the motion of the cutter with the motion of the guard, it can be seen that the cutter's motion is more apparent; this is evident from the motion 'difference' depicted by the bottom plot. However, it can be seen that the signal has higher harmonics based on the movement of the guard. A FFT is performed on the $x_4 - x_2$ signal, shown by bottom plot of Figure 3.1. Intuitively, the fundamental frequency peaks at $f \approx 109$[Hz] similar to the driving frequency.

The results of the FFT for the three measurements are displayed in Figure 3.2. The FFT shows that
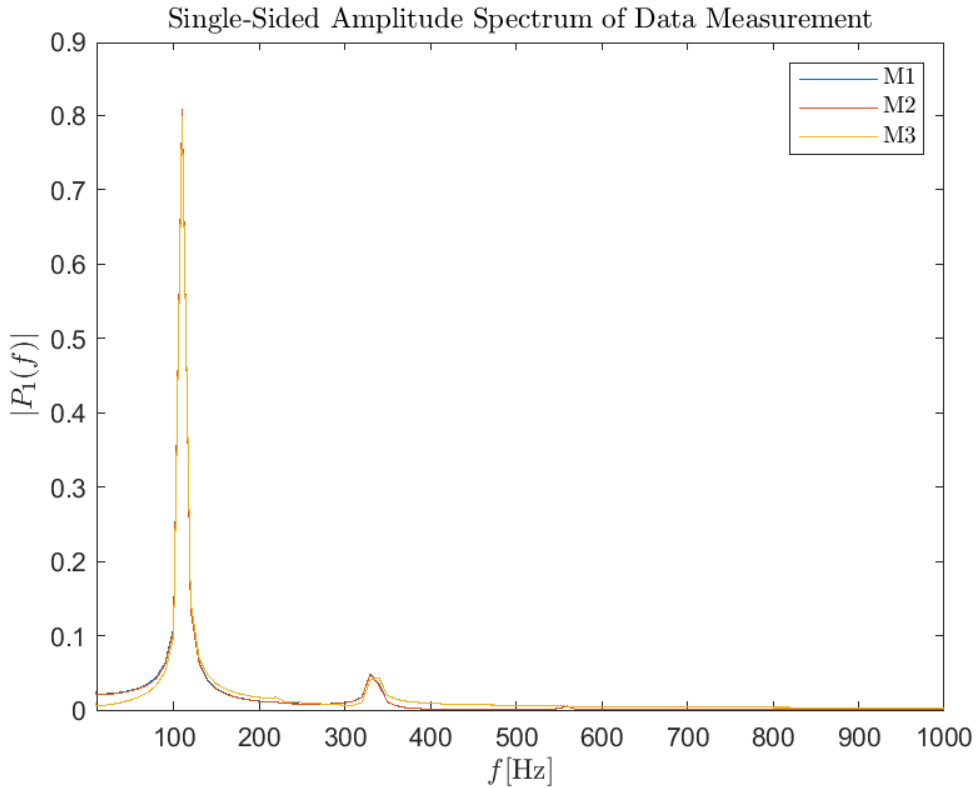
Figure 3.2: FFT of experiment 1, with no backlash gap $(b = 0[\text{m}])$

there are three dominant peaks in the FFT. Where the first peak corresponds to the expected driving frequency of $f_1 = 109.945$ [Hz]. Further study has shown that the second and third peaks are harmonics of the driving frequency since they are integer value of $f_1 = 109.845[\text{Hz}]$, shown in Table 3.1. It should be noted that peaks have a certain width that corresponds to the frequency resolution, calculated with Equation 3.1, that is: $\Delta f = 10[\text{Hz}]$. Since Coulomb friction is the only nonlinearity in this experiment

Table 3.1: FFT harmonics measurement 1

Harmonic	Frequency [Hz]	Difference $f_{i+2} - f_i$ [Hz]
f_1	109.945	-
f_3	329.835	219.890
f_5	559.725	219.890

and since there were no additional peaks in the FFT, it is argued that limit cycles are not produced by Coulomb friction.

Experiment 2, with backlash
For this experiment backlash is added between the driving bridge and the cutter. The backlash width is set to $b = 200e-6[\text{m}]$. Similar to the previous experiment, a FFT is generated from the motion between the cutter and guard. However, because this experiment includes backlash, a possible limit cycle is anticipated to be present. The properties of this limit cycles resulting from the backlash are presented in Appendix C.3. This graphical approach will be described in more detail in chapter 5. Figure C.3 shows that a limit cycle with frequency of $f = 488[\text{Hz}]$ is expected for this experiment. Therefore it

is expected that the FFT corresponding to this experiment shows a peak around this frequency. The FFT for this experiment is again obtained from the bottom graph of Figure 3.3. Taking the FFT of the
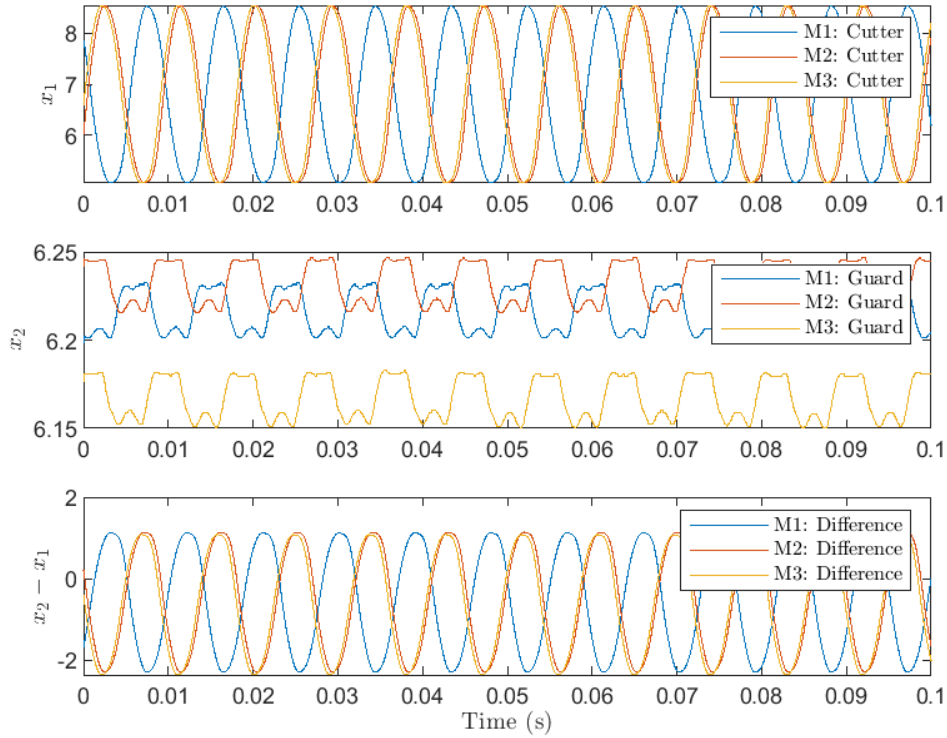
Figure 3.3: Results for 3 measurements with backlash. Top: motion of cutter, middle: motion of guard and bottom: difference between cutter and guard

bottom graph leads to the plot shown by Figure 3.4. The FFT consists of harmonics corresponding to the driving frequency, similar to previous experiment. However, more harmonics are dominant for this experiment. By ignoring the fundamental harmonic, additional information about the harmonics is revealed, shown in Figure 3.5. Note that the frequency difference between the harmonics is not always equal to the frequency of the fundamental harmonic $f = 109.945$. This may be explained by the experiment's frequency resolution of $f = \Delta 10$[Hz], and is thus regarded as a computational mistake. Moreover, the track points shown in the graph above, corresponds to only 1 of the 3 measurements. Measurement 2 and 3, M2 and M3 respectively, have slightly different 'peak' points for the harmonics. The fundamental harmonic, with the corresponding harmonics are shown in the Table 3.2:

Table 3.2: FFT harmonics measurement 2, for three separate measurements

Harmonic	Frequency M1 [Hz]	Frequency M2 [Hz]	Frequency M3 [Hz]
f_1	109.945	109.450	109.450
f_2	219.890	229.885	229.885
f_3	339.830	339.830	339.830
f_4	439.780	449.775	439.780
f_5	559.720	549.725	549.725

No additional frequencies were found in both experiment's FFT, indicating that no limit cycles were present for these experiments. For the first experiment this was straight forward since there was no
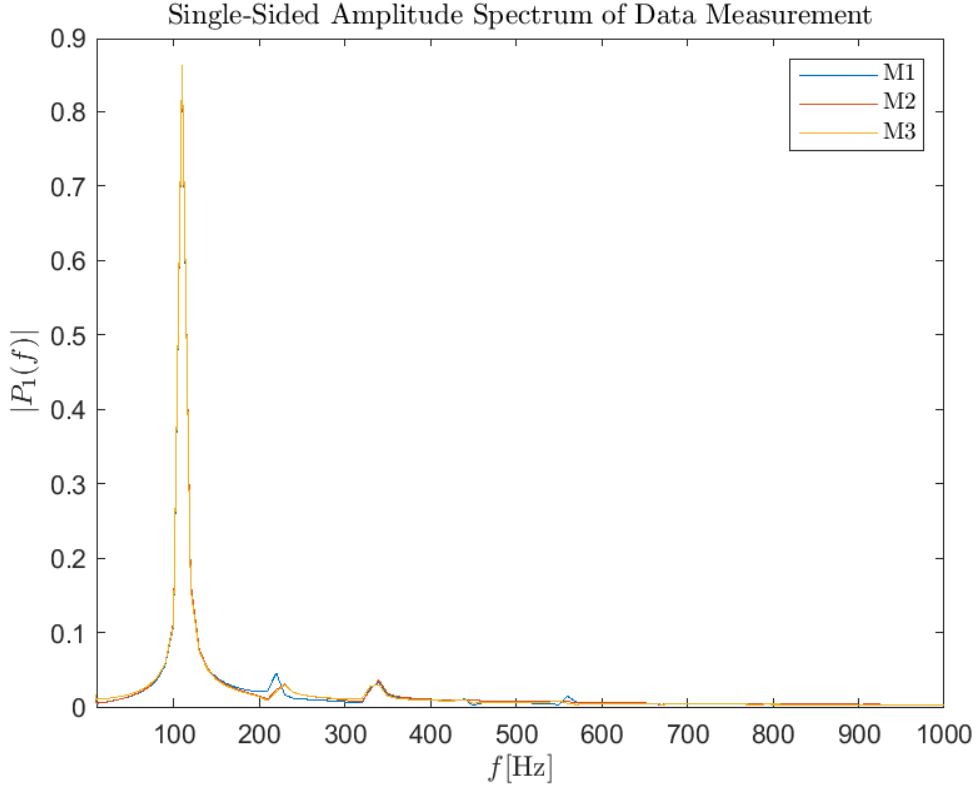
Figure 3.4: FFT of experiment 2, with backlash gap $b = 200\mu m$

backlash added to the system. On the other hand, the second experiment with backlash and based on DF method a limit cycle was expected to have a limit cycle.

3.3   Results general nonlinear Simulink model

This section is used to compare the experiment's findings with relevant Simulink models. Two Simulink models are constructed, one with external driving input in an open-loop configuration, and one without external input in closed-loop configuration, but with initial conditions applied to the system. Because of the latter's closed-loop design, it is anticipated that if a self-sustaining oscillation exists, it will loop through the system. Both configurations are included in Appendix C.5. Both configurations consist of two blocks. One block denotes the backlash nonlinearity, whereas the second block comprises the EOM related to the trimmer. The EOM were derived in chapter 2, however Coulomb friction is now added to these equations. Modelling Coulomb friction as an ideal relay yields to following expression for Coulomb friction: $F = F_c sign(\dot{q}_2 - \dot{q}_1)$[15], where the Coulomb friction value is assumed to be below 1.0[N]. The modified EOM are now shown in Equation 3.2.

$$
\begin{aligned}
\ddot{q}_1 &= \frac{1}{m_1} \left[-(c_1 + c_2)\dot{q}_1 + c_2\dot{q}_2 - (k_1 + k_2)q_1 + k_2q_2 - k_2u - c_2\dot{u} - F_c sign(\dot{q}_2 - \dot{q}_1) \right] \\
\ddot{q}_2 &= \frac{1}{m_2} \left[c_2\dot{q}_1 - c_2\dot{q}_2 + k_2q_1 - (k_2 + k_5)q_2 + k_5q_3 + k_2u + c_2\dot{u} + F_c sign(\dot{q}_2 - \dot{q}_1) \right] \\
\ddot{q}_3 &= \frac{1}{m_3} \left[-(c_3 + c_4)\dot{q}_3 + c_4\dot{q}_4 + k_5q_2 - (k_3 + k_4 + k_5)q_3 + k_4q_4 \right] \\
\ddot{q}_4 &= \frac{1}{m_4} \left[c_4\dot{q}_3 - c_4\dot{q}_4 + k_4q_3 - k_4q_4 \right]
\end{aligned}
\tag{3.2}
$$
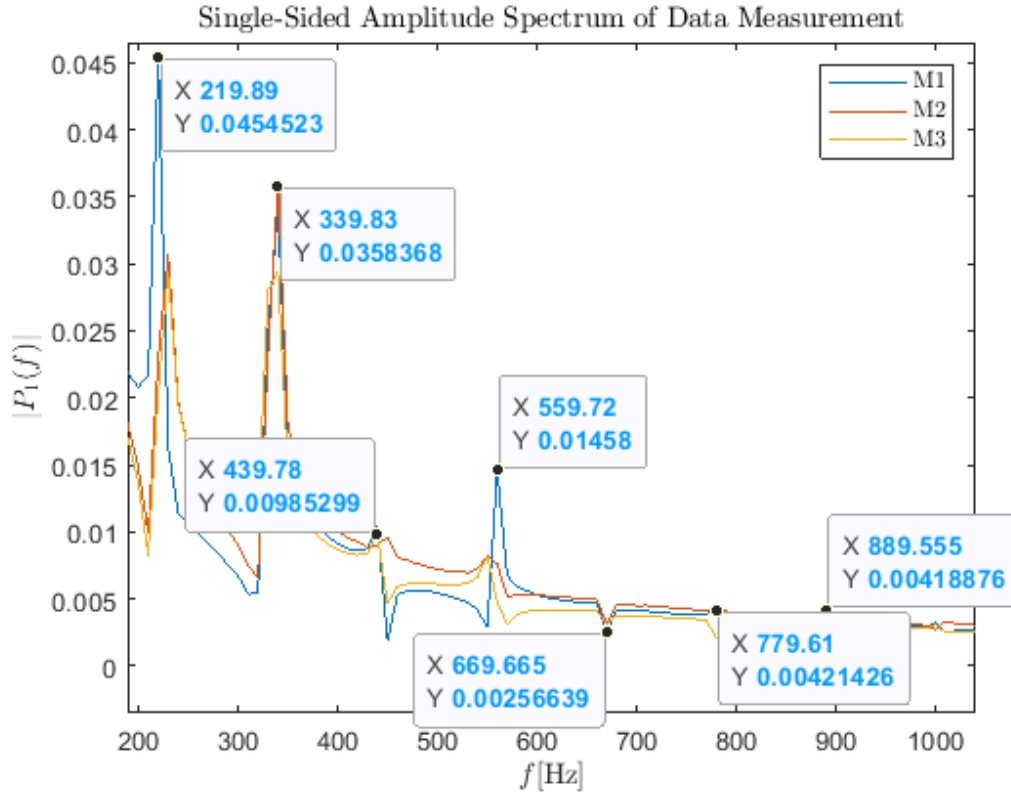
Figure 3.5: FFT with limitation on frequency range: $200 \leq f \leq 1000$[Hz], and with $b = 200\mu m$

where the model parameters are listed in Appendix C Table C.1. Both open-, and closed-loop configurations are simulated for three values of backlash ($b = [200e-6, 200e-5, 200e-4]$[m]), all comprising 3 values for Coulomb friction. First, a simulation of the model $b = 200e-6$[m] that represents the experiment with backlash is performed. The model configuration is listed Figure C.5 with the EOM defined by Equation 3.2. In addition, the time response and the associated FFT for all model configurations are also included in Appendix C.

First the models, resulting from the open-loop configuration shown in Appendix C.6.1, are analysed. The time response and FFT of the model with three options for Coulomb friction is shown in Figure 3.6. This model's time response exhibits the same behaviour as the experiment's time response plot. Filtering out the driving frequency ($f \approx 109$[Hz]) of the FFT lead to the plot shown by Figure 3.6b. The FFT demonstrates that, in addition to the fundamental driving frequency (which was filtered out for visual purposes), the open-loop configuration is dominant for the third and fifth harmonics, just as the experimental study proved. Additionally, the open-loop configuration's FFT did not reveal any additional harmonics, leading to the conclusion that the model and experiment are in agreement.

Since the experimental data and the general model coincide to some extent, the backlash size from the general model is gradually increased. Observing that the generic model does exhibit limit cycle behaviour for some larger values of b is the aim of this exercise.

Increasing the backlash width to $b = 200e-4$[m] generates the time response shown in Figure 3.7.
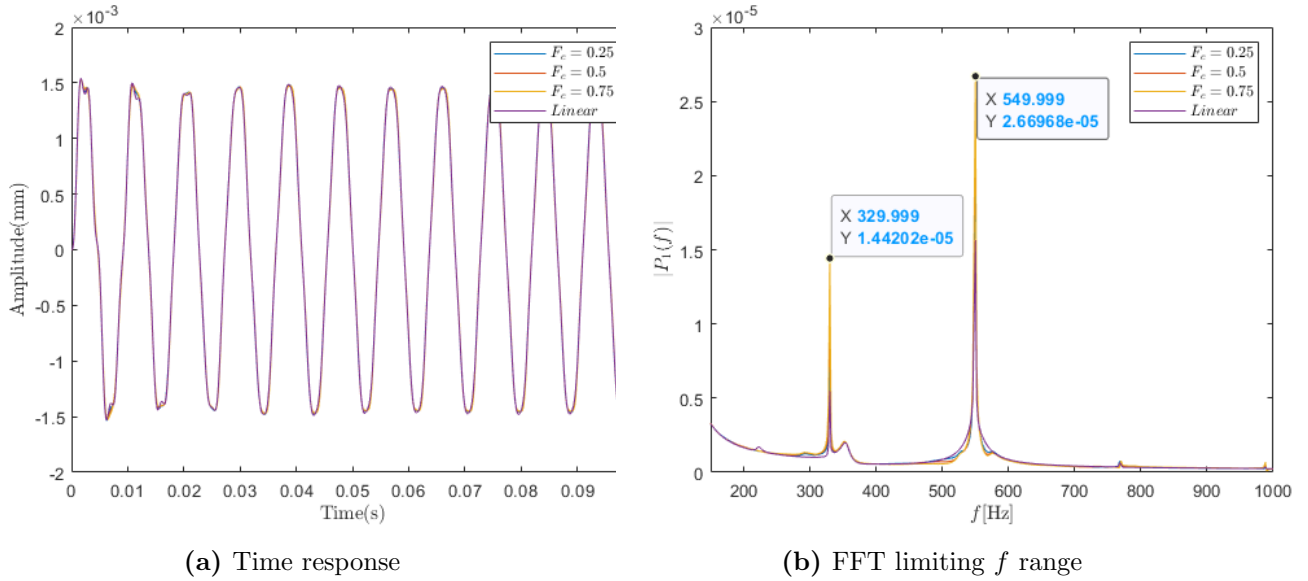
(a) Time response

(b) FFT limiting f range

Figure 3.6: Time response open-loop configuration, for $b = 200e - 6$[m] and $F_c = [0.25, 0.50, 0.75]$
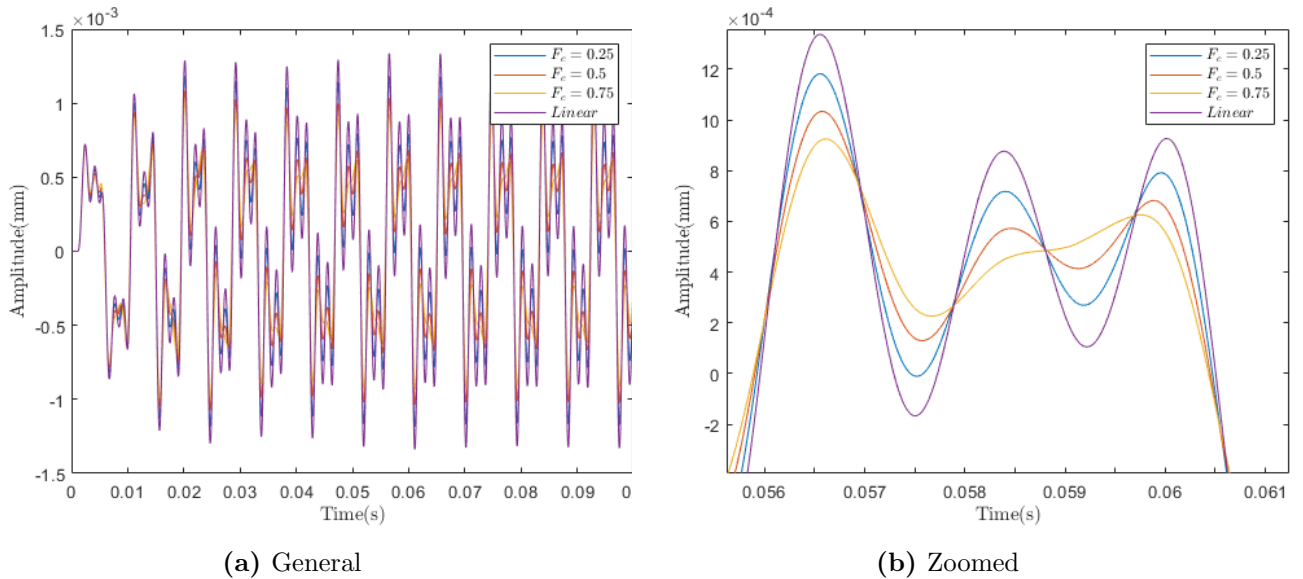
(a) General

(b) Zoomed

Figure 3.7: Time response open-loop configuration, for $b = 200e - 4$[m] and $F_c = [0.25, 0.50, 0.75]$

Figure 3.7b shows the zoomed time response of Figure 3.7a on top of a base harmonic. It is observed that there is an additional oscillation on top of top base oscillation, in fact it is observed that there are 2 additional oscillations. This suggests that the system may contain a limit cycle. In addition, it is observed that the amplitude of the new oscillations is suppressed by increased Coulomb friction, but the frequency of the oscillations is unaffected. Physically, this is explained by the fact that when Coulomb friction is applied, the self-sustained oscillations between the cutter and guard would encounter horizontal resistance, resulting in a decrease in amplitude but not in frequency. A FFT operation is used to the time response signal to calculate the frequency of the extra oscillation(s), shown by Figure 3.8.

(a) General

(b) Zoomed
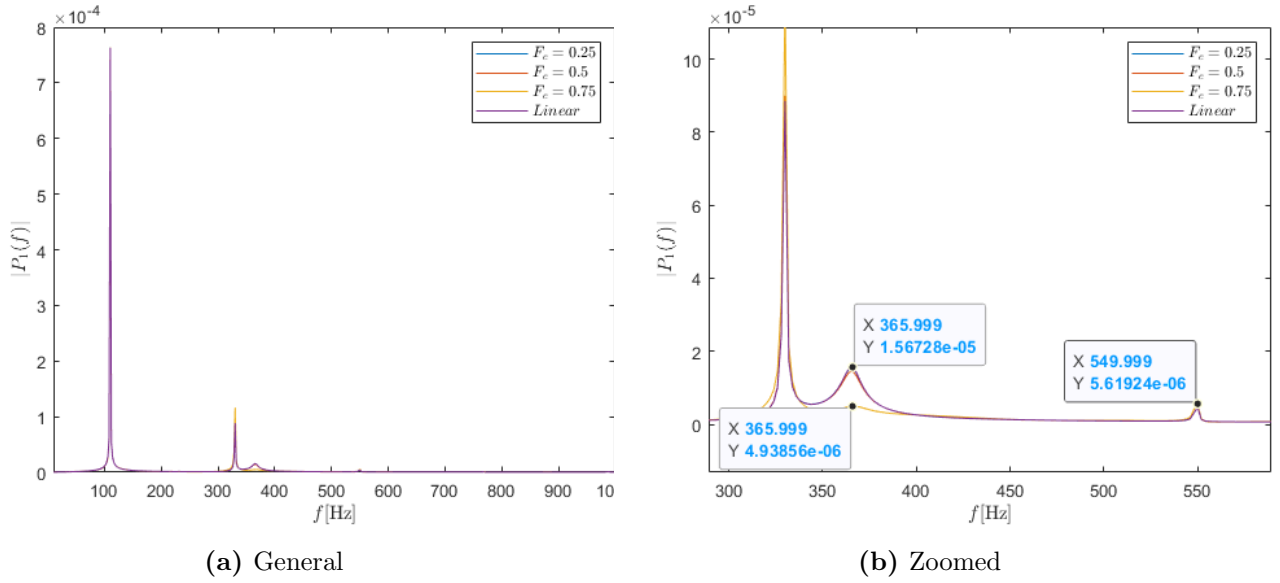
Figure 3.8: FFT: open-loop configuration, for $b = 200e - 4[m]$ and $F_c = [0.25, 0.50, 0.75]$

Figure 3.8a shows the general FFT of the open-loop configuration. Besides the harmonics corresponding to the driving frequency, the open-loop configuration contains additional peaks in the FFT. Filtering out the fundamental driving frequency leads to the plot shown by Figure 3.8b.

This plot shows 2 additional peaks in the FFT, with frequency $f = 365.999[Hz]$ and $f = 549.999$ [Hz], where the latter corresponding to the fifth subharmonic of the driving frequency of $f_5 = 549.999[Hz]$. However, the former does not correspond to a subharmonic. A limit cycle could be the cause of this frequency. The closed-loop configuration is simulated without using an external driving frequency to confirm that this is the case. The FFT for two limiting cases of b are shown in Figure 3.9, another case for an intermediate value of b, and the related time response, is shown in Appendix C.6.2. From

(a) $b = 200e - 6$

(b) $b = 200e - 4$
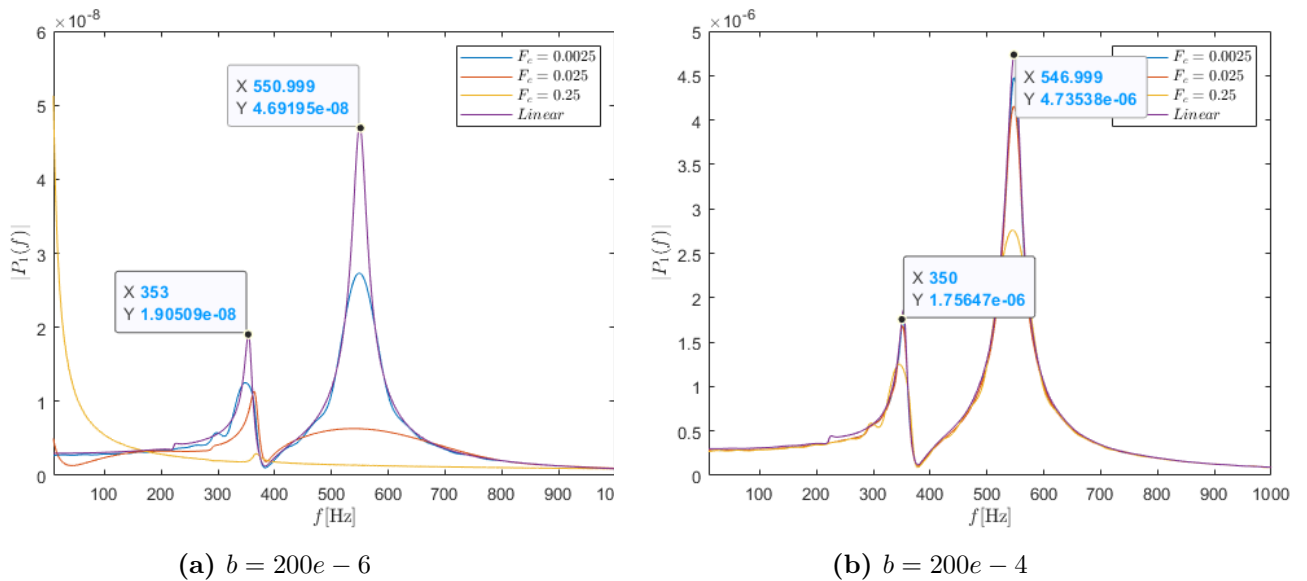
Figure 3.9: FFT: closed-loop configuration with $F_c = [0.0025, 0.020, 0.25]$

the Figure 3.9, it is observed that a peak corresponding to $f \approx 350[Hz]$ is observed no matter what the value of backlash is. The peak from the open-loop configuration agrees with this frequency. As

a result, it may be concluded that this peak belongs to a limit cycle. In addition, it is shown that when Coulomb friction value increases, the amplitude of the limit cycle is suppressed. Furthermore, the FFT's shown by Figure 3.9 demonstrate that when the backlash gap is increased, more Coulomb friction is needed to alleviate/suppress that peak [16]. As a result, the following conjecture is put forth: when Coulomb friction is introduced to the system, the amplitude of the limit cycle, that results from the backlash nonlinearity, is suppressed.

Chapter 4

Including nonlinearities in the simulation model

The trimmer's digital twin is created using Simulink models and Matlab code. Given that the DF approach depends on two distinct blocks, one linear and one nonlinear, the codes are likewise divided in this way. Furthermore, the DF method can only be used if the linear part behaves as a low-pass filter.

4.1   The linear model

The Matlab code that constructs the state-space representation, associated to the linear part of the model, is briefly explained and listed in Appendix A.2. Additionally, this code is used to determine whether the filtering hypothesis is true for the linear component of the model. For the remainder of this research the model parameters used in this project are listed in Appendix C Table C.2. Please take note that these model parameters differ from the experiment's model parameters. The filtering hypothesis is examined using the Bode plot, which is generated from the transfer function obtained from the state-space representation.

4.2   The nonlinear model

Utilising the linear transfer function, that results from the state-space representation, one can check is the condition for harmonic balance applies to the overall nonlinear system. A brief description of the code is listed in Appendix A.10. As mentioned there, the code can be applied for several nonlinearities which are defined as external function and are called within the general code. These functions itself, are also listed in Appendix A for the associated nonlinearities discussed in this research. Some of the self-defined code can be validated by comparing the i/o wave characteristics from the self-defined code with the results from built-in functions. However, Matlab does not have built-in function for all nonlinearities discussed in this report. In fact, Matlab only has built-in functions for friction-controlled backlash and Coulomb friction. Once the self-defined code for friction-controlled backlash is validate according to the built-in code, this code can serve as the foundation for the codes of inertia-, viscous-controlled backlash, and as a foundation for the code of the equivalent nonlinearity.

4.2.1   Friction-controlled backlash

First the self-defined code for friction-controlled backlash is constructed. The entire function, for the DF of friction-controlled backlash, is listed and briefly described in Appendix A.4. However, when computing the simulink time response of the system, the input-output wave characteristics in

time domain have to be defined as Equation 2.36. The code corresponding to the time domain is listed in Appendix A.8. Where the code in time domain validates that the built-in friction-controlled backlash yields equivalent i/o-behaviour as the self-defined code for the friction-controlled backlash when subjected to a sinusoidal function, shown in Figure 4.1.
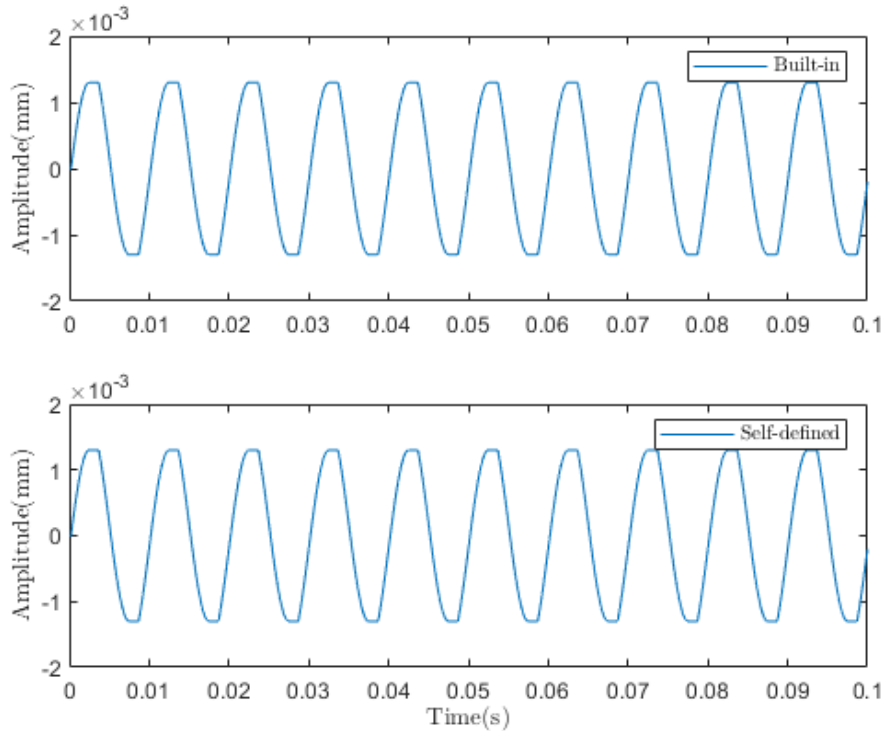
Figure 4.1: Output of built-in and self-defined block, where $b = 0.0004$[m]

4.2.2   Inertia-controlled backlash

Also for inertia-controlled backlash the DF (Appendix A.11) and the i/o wave characteristic in time domain are known (Appendix A.9). The DF is used to check if the condition for harmonic balance is satisfied, whereas the code corresponding to the i/o wave characteristic is used in the simulink model. Again the code and a brief description is listed in Appendix A.9. If an external sinusoidal function is applied to the code describing the i/o wave characteristic in time domain, then it produces the output shown in Figure 4.2.
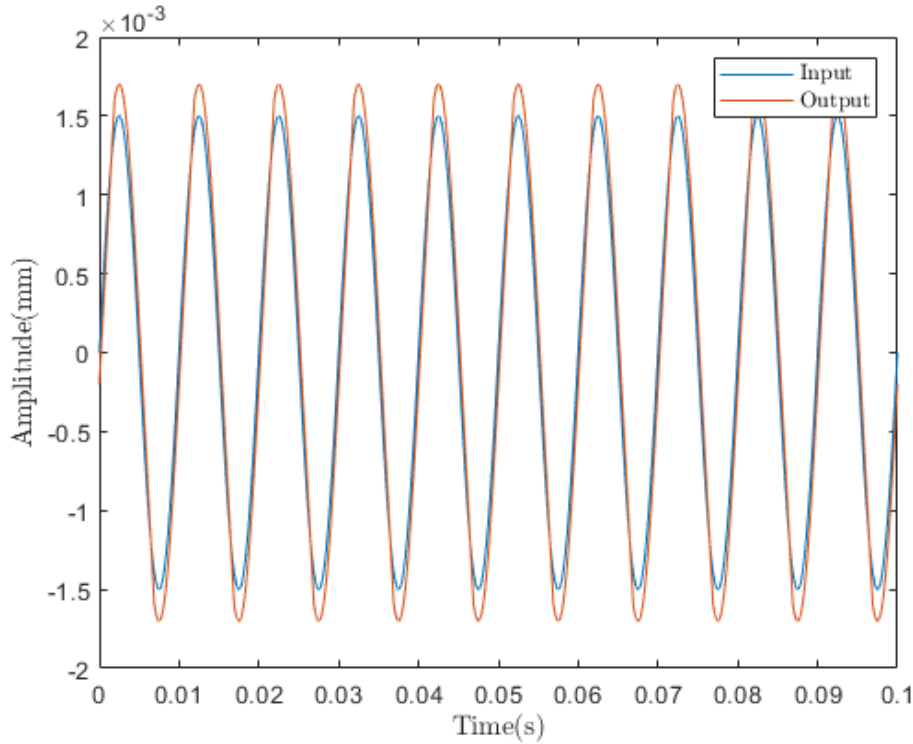
Figure 4.2: Input wave compared to output wave

Investigation of the signal prove that output signal shows similar behaviour as Figure 2.10. Additionally, the same code is used to analyse the i/o-relation for varying backlash widths b. The graph is shown in Figure 4.3. Amplitude of input wave is fixed at a value of $A = 0.0015[m]$. From Figure 4.3, it is observed that if $b = 0$ the output of the inertia-controlled nonlinearity shows similar characteristics as the sinusoidal input wave, as expected.

4.2.3 Viscous-controlled backlash

For friction-, and inertia-controlled backlash both the corresponding DF's and the i/o wave characteristics were known. For viscous-controlled backlash the i/o wave characteristics (shown by Figure 2.11) is not derived, however the DF is. Therefore it is still possible to check whether or not the condition for harmonic balance is satisfied for viscous-controlled backlash. As described in theory, the waveform depends on the ratio $\frac{M}{D}$, where D can be thought of the amount of inertia involved in the backlash, while M can be thought of the amount of friction. If $D = 0$ the nonlinearity is considered as a inertia-controlled backlash nonlinearity, when $M = 0$ the nonlinearity is consider as a friction-controlled nonlinearity. To construct the DF related to the viscous-controlled backlash, this ratio of $\frac{M}{D}$ has to be known. In general this ratio is however unknown, and therefore some arbitrary values are used in the DF code for viscous-controlled backlash, listed in Appendix A.6. Here the complex code generates the DF denoted by Equation 2.47. For an arbitrary ratio of $\frac{M}{D} = \frac{1}{99}$ and for an input frequency corresponding to the driving frequency $f = 100[Hz]$, the separation angle on which the viscous-controlled backlash DF is based can be calculated according to:

$$\gamma = \left(\frac{M}{D}\right)\omega$$

$$\gamma = \left(\frac{1}{99}\right)(2\pi 100)$$

$$\gamma = 634.6652[Hz]$$
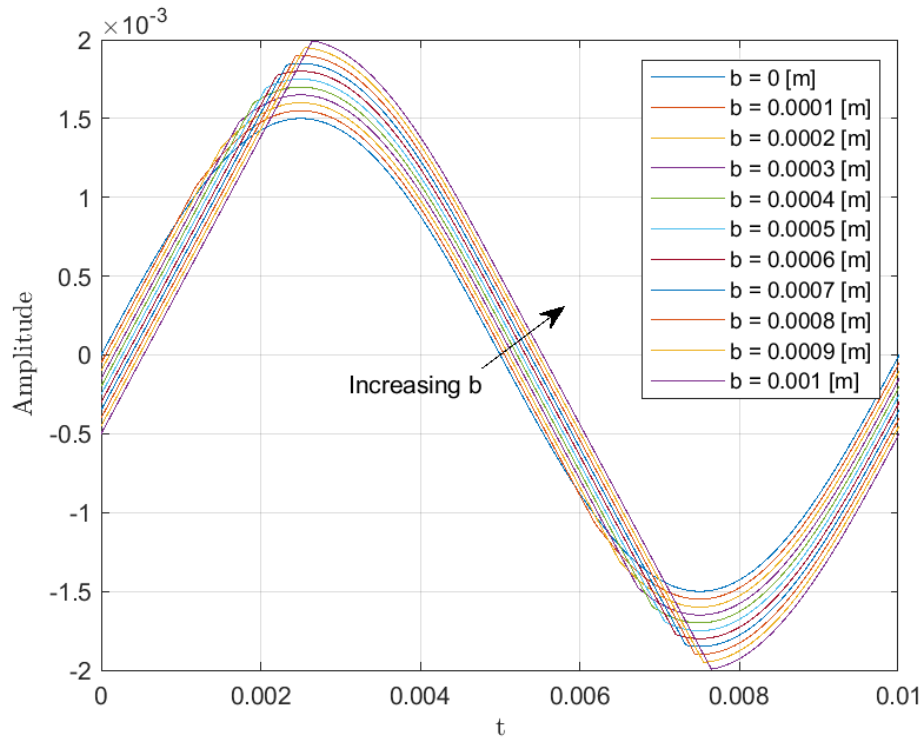
Figure 4.3: Inertia-controlled wave characteristics for inertia-controlled backlash for a variety of backlash widths b

According to Equation 2.44 the separation angle between motor and driving bridge is then defined as:

$$\phi_s = \tan^{-1}\left(\frac{1}{\gamma}\right)$$

$$\phi_s = \tan^{-1}\left(\frac{1}{634.6652}\right)$$

$$\phi_s = 0.0016[s]$$

Chapter 5

Simulation and results

In Chapter 3 and Chapter 4, experimentally obtained data was compared to data obtained from Simulink models. In this chapter the results of the developed Matlab models, especially the models that compute the condition for harmonic balance, are described and analysed. Before confirming that this condition is satisfied, the filtering hypothesis has to be checked on the linear part of the system. If the linear part of the system behaves as a low-pass filter, the condition can be checked, resulting in amplitude and frequency of potential limit cycles [1]. For friction-, inertia-controlled backlash, Coulomb friction and for the equivalent nonlinearity these predictions are then further verified by means of a FFT, that result from the time response of an associated simulink model.

5.1   Results linear trimmer model

The results from the Matlab model presented in section 4.1 will now be analysed. The results follow directly from the code listed in Appendix A.2.

5.1.1   General model definition

In chapter 2 it was derived that the output matrix C-matrix, resulting from the state-space representation Equation 2.10, only includes the relative position between m_2 and m_4. This makes the linear model a single-input single-output (SISO) model. The associated code for the linear part of the model is briefly described and listed in Appendix A.2.

Time response is usually the first thing to analyse when dealing with linear systems. this can be simulated according to the built-in function: `lsim(sys,u,t,init)` [2], where *sys* denotes linear dynamical system defined by Equation 2.10, u is the external driving input, t is the period over which the system has to be simulated and *init* posses the initial condition of the system. It is assumed that the system experiences nominal initial conditions. System parameters are not altered or disturbed in nominal initial conditions [18]. From the command: `lsim(sys,u,t,init)`, subjected to a external input $u(t) = 0.0015sin(2\pi100t)$, it follows that the time response of the system precisely oscillates according to the external to this external input $u(t)$, shown in Figure 5.1:

---

[1]If the condition is not satisfied, there is no limit cycle and hence no associated amplitude and limit cycle

[2]Other methods such as: `ode15s|` can also be used to compute the time response, but state-space model has to be derived anyway, since transfer function is based on that
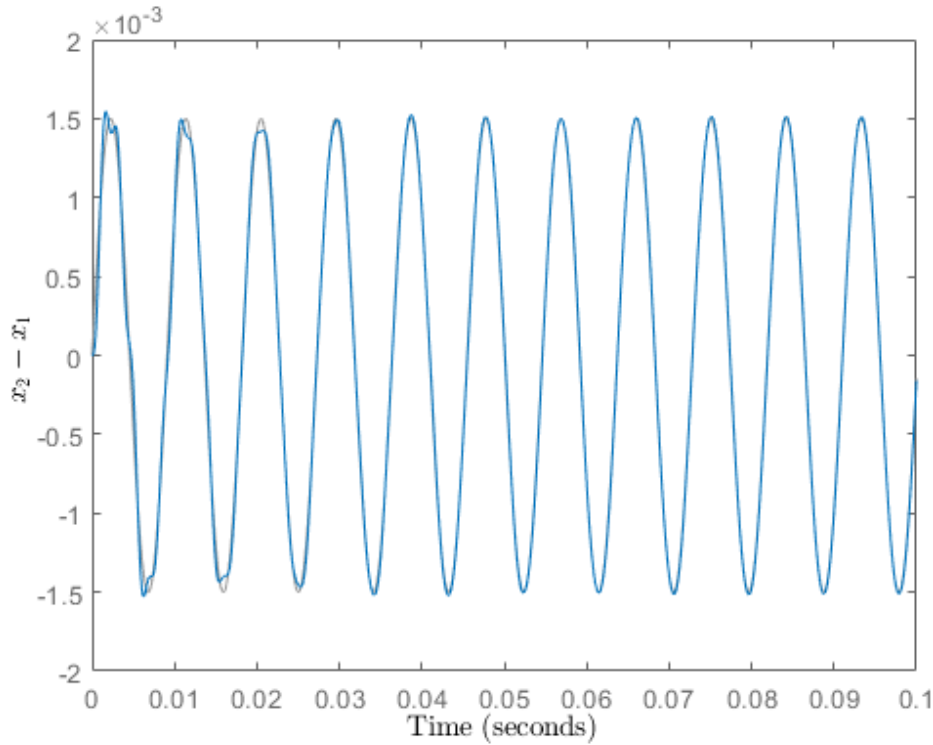
Figure 5.1: Time response of linear system, subjected to $u(t) = 0.0015 sin(2\pi 100 t)$

The output amplitude oscillates similarly to the input amplitude $A = 0.0015$[m]. Despite the absence of Coulomb friction in this linear model, the general model's time response is consistent with the results of experiment 1 in section 3.2.

5.1.2 Frequency response linear model

Since $G(s) = C(sI - A)^{-1}B + D$, the transfer function directly follows from the state-space representation derived in the preceding section, resulting in the following transfer function:

$$G(s) = \frac{1^7 s^6 + 1.233^{10} s^5 + 5.939^{14} s^4 + 1.655^{17} s^3 + 4.079^{21} s^2 + 3.71^{23} s + 5.79^{27}}{s^8 + 1378 s^7 + 7.076^7 s^6 + 3.878^{10} s^5 + 1.069^{15} s^4 + 2.676^{17} s^3 + 4.889^{21} s^2 + 4.595^{23} s + 5.971^{27}} \quad (5.1)$$

As previously indicated, the filtering hypothesis can be tested using this transfer function. Recall that filtering hypothesis is satisfied if: $|G(j\omega)| \gg |G(jn\omega)|$, for $n = 2, 3, ...$, such that the linear part of the model filters out any harmonic generated by the nonlinearity. It is observed that the model order of the Equation 5.1 is equal to the order of the denominator polynomial, therefore the model order is equal to 8. The transfer function is then utilised to obtain the Bode plot, shown in Figure 5.2. At the same time, Matlab determined the cutoff frequency of the transfer function $\omega_c = 4.6329e + 03$[rad/sec]. Ideally, a low-pass filter attenuates all frequencies above this frequency, but from the Figure 5.2 it is observed that some frequencies are still passed through. This is characterised by the rate of the roll-off frequency. For a low-pass filter of first-order, the roll-off frequency is -20[dB] per decade of frequency. The roll-off rate is significantly higher with higher-order low-pass filters. According to the trimmer dynamics, the low-pass filter's is approximately 1, since it can be observed from Figure 5.2 that the roll-off rate is roughly -20[dB] per decade. This implies that harmonics of the second order
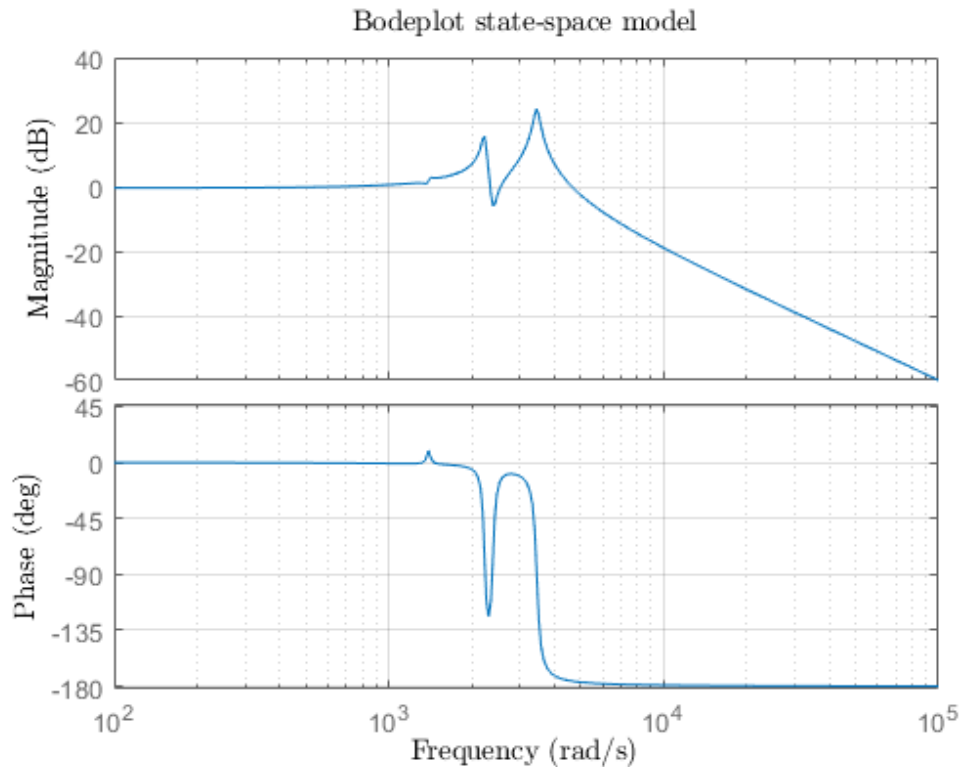
Figure 5.2: Bode plot for SISO linear system

will be attenuated with this transfer function and thus the first-order DF method can be applied to the overall system.

In addition the peaks in the Bode plot Figure 5.2, represent resonance frequencies. Resonance frequencies imply that the system contains poles, that may result in errors when using the DF technique approach [2].
DF method utilises the intersections of the linear transfer function and $-1/N(A, \omega)$, on the complex plane by means of the Nyquist locus corresponding to the transfer function Equation 5.1. The Nyquist locus of the transfer function is shown in Figure 5.3. The direction of increasing frequency is indicated by the arrows on the aforementioned Nyquist locus. Further analysis of the Nyquist locus indicates that it does not encircle the point $(-1, 0j)$. From Nyquist stability theorem it can then be concluded that the open-loop system is stable, i.e. $N = 0$ [6].

5.1.3 Linear stability analysis

To quantify the resonance frequencies, corresponding to the peaks in Figure 5.2, the stability of the linear part has to be analysed. It is possible that the some of the resonance frequencies are not visible in Figure 5.2 since they are not dominant for the output of $y = x_2 - x_4$. From the figure 2 peaks are clearly visible, but further investigation has shown that there is are two additional small (in terms of magnitude) resonant frequencies. These resonance frequencies correspond to the imaginary parts of the eigenvalues of the A-matrix from state-space representation or poles of the transfer function defined by Equation 5.1[3].

---

[3]Figure 5.2 also shows 'valleys' in the Bode plot, these correspond to the complex zeros of the transfer function
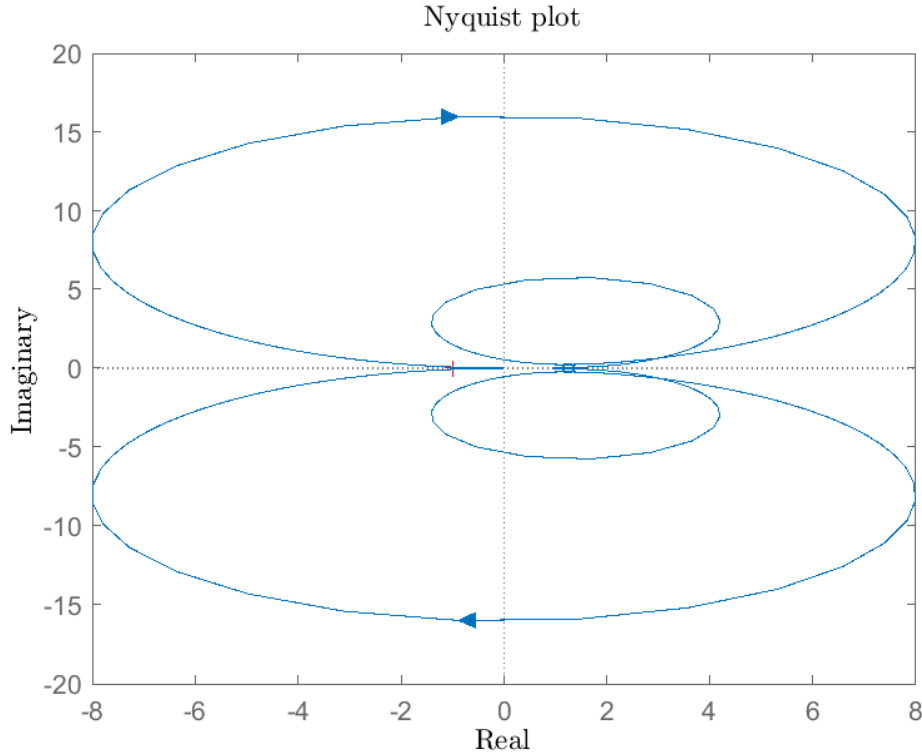
Figure 5.3: Nyquist locus of the transfer function $G(j\omega)$ from Equation 5.1

Computing the eigenvalues, associated to this system, with the eigenvalue problem: $\det(A - \lambda I) = 0$. For this 4DOF , the eigenvalue problem results in 8 complex eigenvalues:

$$
\begin{aligned}
\lambda_{1,2} &= -541.6448 \pm 7159.6999i \\
\lambda_{3,4} &= -80.5896 \pm 3453.172i \\
\lambda_{5,6} &= -41.8148 \pm 2229.5063i \\
\lambda_{7,8} &= -24.9984 \pm 1397.0567i
\end{aligned}
\tag{5.2}
$$

Observe that all eigenvalues have negative real component and therefore the linear system is considered to be stable according to corollary 2.2.0.1. Furthermore observation shows that all eigenvalues come as duplicates with positive and negative imaginary part, indicating either a pole or zeros with associated frequency of that imaginary component. For example $\lambda_{1,2}$ should show a peak at $\omega = 7159.6999$[rad/sec], but this is not visible since this pole/zeros might not be dominant for the output $y = x_2 - x_4$.

Effect of damping
To visualise the frequencies that are not dominant for the output, the effect of damping is analysed by deliberately changing the output matrix to track the position of x_1, x_2, x_3 and x_4:

$$
\vec{y(t)} = \underbrace{\begin{pmatrix} 1 & 1 & 1 & 1 & 0 & 0 & 0 & 0 \end{pmatrix}}_{C} \vec{x(t)}
\tag{5.3}
$$

Then the existence of these poles/zeros validated by considering a damping effect on the linear system. This is done by changing the damping coefficients (c_1, c_2, c_3 and c_4) to very small values. Based on this

slightly changed model the resonance frequencies of the system, that were initially not visible, show up in Figure 5.4.
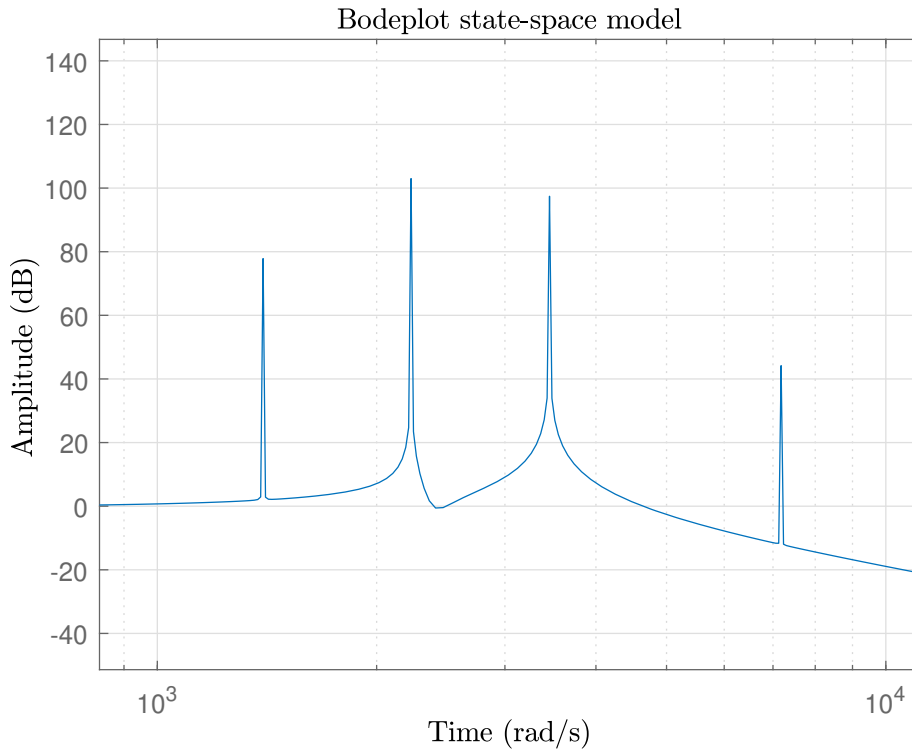
Figure 5.4: Bode plot for the system without damping

Figure 5.4 shows 4 distinct resonance frequencies corresponding to the imaginary parts of the eigenvalues of Equation 5.2.

However, the relevance of the resonance and anti-resonance frequencies for this is system is negligible since the operating frequency of system $f \approx 100$[Hz], is far below the first (anti)resonance frequency of $f \approx \frac{1397.0567}{2\pi} = 222.35$[Hz]. It is necessary to look at the resonance frequency that corresponds to the peak that is farthest to the right in Figure 5.4 since theory of the DF requires that filtering hypothesis is achieved. This is not entirely achieved if this peak is not suppressed. In other words, the resonant frequency of corresponding to that peak will not be attenuate if damping was not included. So it can be concluded that the damping ensures that (anti)resonance frequencies are suppressed in absolute magnitude. In addition, damping does not change the resonance frequencies since the (anti)resonance frequencies of Figure 5.4 directly correlate to the (anti)resonance frequencies shown in Figure 5.2. The significance of these observations must be considered since the operating frequencies is far below the first resonant frequency. And it is very unlikely that the induces limit cycle has a frequencies that precisely corresponds to the farthest to the right resonant frequency has has no attenuate of the higher Fourier coefficients is achieved.

5.2   Results nonlinear model

In the previous section it was shown that the filtering hypothesis was satisfied for the linear part of the system, so the third assumption listed in subsection 2.3.2 is validated. Anterior to the application

of the DF method itself, the other three assumptions must be satisfied. These three assumptions are related to the nonlinear part of the system.

- First assumption states that the system contains only 1 nonlinear component. For friction-, inertia-, viscous-controlled and Coulomb friction this assumption is obviously accomplished. For the equivalent nonlinear system this assumption does not apply, however as the name suggest, an equivalent nonlinearity can be derived based upon the two constituent nonlinear components, therefore this assumption is also accomplished for the equivalent nonlinearity.

- Second assumption states that the nonlinear component is time-invariant, i.e:

$$y(t) = f(x(t), t) = f(x(t))$$

  this assumptions applies to all models.

- The fourth assumption, states that the nonlinear component is odd, i.e., $f(-y) = -f(y)$. This is easily validated when observing the input-output considered for backlash and Coulomb friction functions. Both curves show rotational symmetry around the origin and hence are odd functions. This implies that the static term in Fourier expansion (a_0) vanishes.

Therefore it can be concluded that the 4 assumptions are accomplished for all nonlinearities and hence the DF method can be applied to the system.

The results where the nonlinear component is included in the system are analysed according to the following order: Starting by analysing the results for the friction-controlled backlash nonlinearity. Subsequently, the inertia- and viscous-controlled backlash nonlinearities will be analysed in similar manner. After that, the Coulomb friction nonlinearity model will be analysed. Finally, the equivalent nonlinearity model results naturally from the preceding results since the equivalent nonlinearity is a combination between two nonlinearities. For all models the condition for harmonic balance is checked. If this is achieved, the predicted properties resulting from that condition, might be validated by means of a corresponding FFT generated from associated Simulink model, as done in experiment. In addition, the models for friction-, and inertia-controlled backlash will be analysed with and without external reference forcing function.

5.2.1   Results : friction-controlled backlash

In general, it is assumed that the backlash in the trimmer dynamics behaves like a friction-controlled backlash, since the spring coil (shown on Figure 2.1a) that presses the cutter on the guard is relatively high. Resulting in high normal force between cutter and guard and thus the frictional force is relatively high since $F_N = \mu N$. Computing the condition for harmonic balance for friction-controlled backlash, the code listed and described by Appendix A.10 is used, where the external Coulomb friction function is replaced with the function for friction-controlled backlash denoted in Appendix A.3.

From theory it is known that $-1/N(A)$ tends to grow to the point $(-1, 0j)$ with increasing amplitude A, whereas the increasing direction b tends to grow away from zero to $(-\infty, -\infty j)$ on the complex-plane. Graphically, the condition for harmonic balance is checked if the two curves of $G(j\omega)$ and $-1/N(A)$ intersection on the complex plane. Since the Nyquist locus associated to the transfer function $G(j\omega)$ is already shown on Figure 5.3, only the locus associated to $-1/N(A)$ must be computed.

The verification of the friction-controlled backlash nonlinearity in terms of i/o wave characteristics, has been proven in subsection 4.2.1. However, the code for friction-controlled backlash DF, which checks the condition for harmonic balance is yet to be verified. Comparing the results from friction-controlled backlash DF code with results generated by Python programming language is one way to

validate the code. Since Python consists of a library for common DF's. One of the DF's, is the DF for friction-controlled backlash. Graphically, it is observed that the code written in Matlab produces an equivalent curve as the DF for friction-controlled backlash obtained from Python, shown in Figure 5.5. The curve for Matlab's self-defined DF shows an equivalent trend to the curve for Python's built-in

(a) Matlab   (b) Python
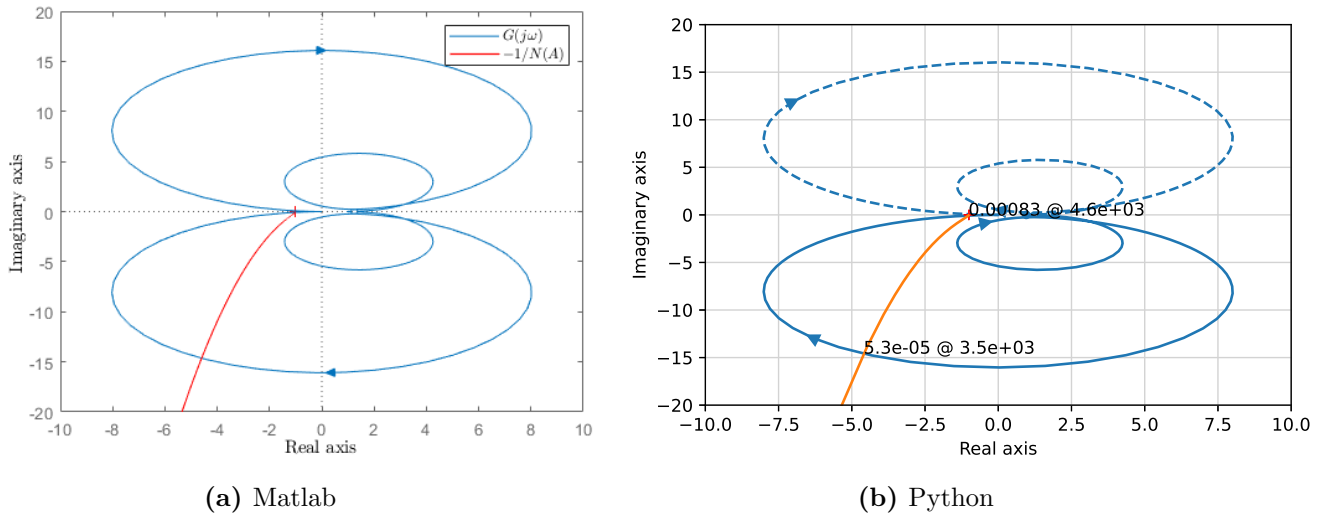
Figure 5.5: Transfer function with $-1/N(A)$, for friction-controlled backlash DF, where $b = 1e-4$[m]. Comparison Matlab with Python

DF. From this it can be concluded that the Matlab code is correctly coded. Using Python's built-in code has several advantages. One of them is that the code automatically generates the amplitude and frequency of the limit cycles associated with the intersection between the transfer function and the DF, shown in Figure 5.5b. A disadvantage is that the built-in library does not contain many DF, only the friction-controlled backlash DF, used in this section, is available.

Without external input
In section 3.1 the open-loop configuration was mostly used since this served to validate that the time response of these models matched the experimental data. However, DF theory is based on closed-loop configuration without external driving function ($r = 0$), shown in Figure 2.5. This configuration is more accessible since it only shows a peak in the FFT corresponding to the limit cycle.
Energy is applied to the system with an impulse input. It is expected that the output of the model only show one oscillations with a frequency corresponding to the frequency of the limit cycle. It is also possible that the system does not show any limit cycles since the backlash width has not reached a certain value, such that it never intersects with the curve of the transfer function. Logically this leads to the question: what is the maximum width of b so that the DF theory does not predict limit cycles? Or in other words: at what value of b does the first intersection between $-1/N(A)$ and $G(j\omega)$ occur? By trial and error, this value is approximately $b \approx 2e-8$[m], shown in Figure 5.6.
From Figure 5.6, it is observed that for a value of: $b = 1e-8$[m] no intersection occur thus no limit cycle predicted, $b = 2e-8$[m] the two curves just 'touch' each other so no limit cycle predicted. Incorporating these higher harmonics will be discussed in section 6.4. A value of $b = 3e-8$[m] shows a clear intersection between the two curves, and based on DF theory a limit cycle is predicted.
Summarising, the results obtained from the condition for harmonic balance corresponding to Figure 5.6. For a value of $b = 1e-8$[m], no limit cycle is predicted, $b = 2e-8$[m] on the edge of the existence of a self-sustained limit cycle, whereas the value of $b = 3e-8$[m] clearly predicts a limit cycle. From these values, Simulink is able to compute the related time responses. Resulting in the
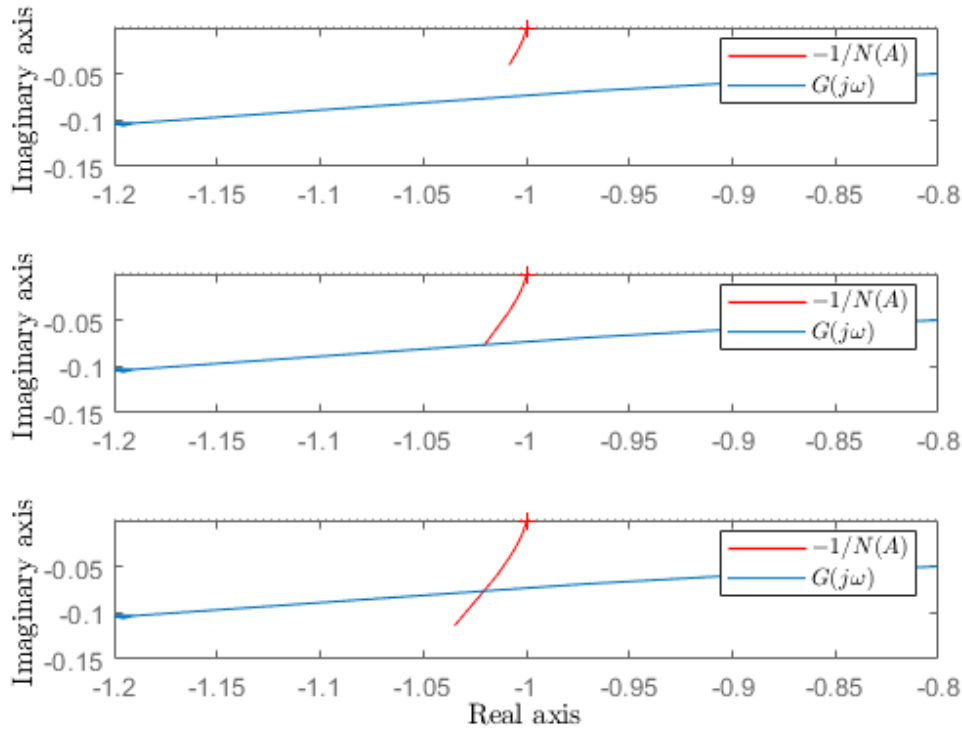
Figure 5.6: First row: $b = 1e - 8[m]$, second row: $b = 2e - 8[m]$ and last row: $b = 3e - 8[m]$

time responses shown in Figure 5.7. Simulink models shows that indeed no limit cycling behaviour is observed for $b = 1e - 8[m]$. For a value of $b = 2e - 8[m]$ very small self-sustained oscillations are observed, and for a value of $b = 3e - 8[m]$ self-sustained oscillations are observed. Therefore it can be concluded that the predictions, based on the condition for harmonic balance indicated with Figure 5.6, are in agreement with the results obtained from the time response from Simulink indicated by Figure 5.7.

The value of b is now increased to $b = 4e - 6[m]$. Similar to Figure 5.6, a graphical representation between $G(j\omega)$ and $-1/N(A)$ is generated, shown in Figure 5.8. From Figure 5.8 it is observed that there is a single intersection, occurring near the origin, with amplitude: $A_{lch} = 3.3138e - 05[m]$ and frequency $\omega_{lch} = 4.6077e + 03$ [rad/sec], that is $f_{lch} = \frac{4.6077e+03}{2\pi} = 733.3[Hz]$[4] . Subsequently, the corresponding Simulink model, is simulated with an impulse input, resulting in the output shown by Figure 5.9: It is observed that a self-sustained exists, since the time response of the system does not die out if: $t \to \infty$, in other words the system keeps oscillating. This oscillation, corresponding to the limit cycle, is indicated in Figure 5.9a. The amplitude[5]. of that limit cycle is measured from that graph, leading to an amplitude of:

$$A_{lcs} = \frac{3.303e - 5 - -3.2961e - 5}{2}[m]$$
$$A_{lcs} = 3.2995e - 05[m]$$

Comparing this value for the amplitude of the limit cycle to the value for the amplitude generated

---

[4]script from: A_{lch} stands for limit cycle amplitude predicted by the condition for harmonic balance
[5]script from: A_{lcs} stands for limit cycle amplitude predicted by Simulink model
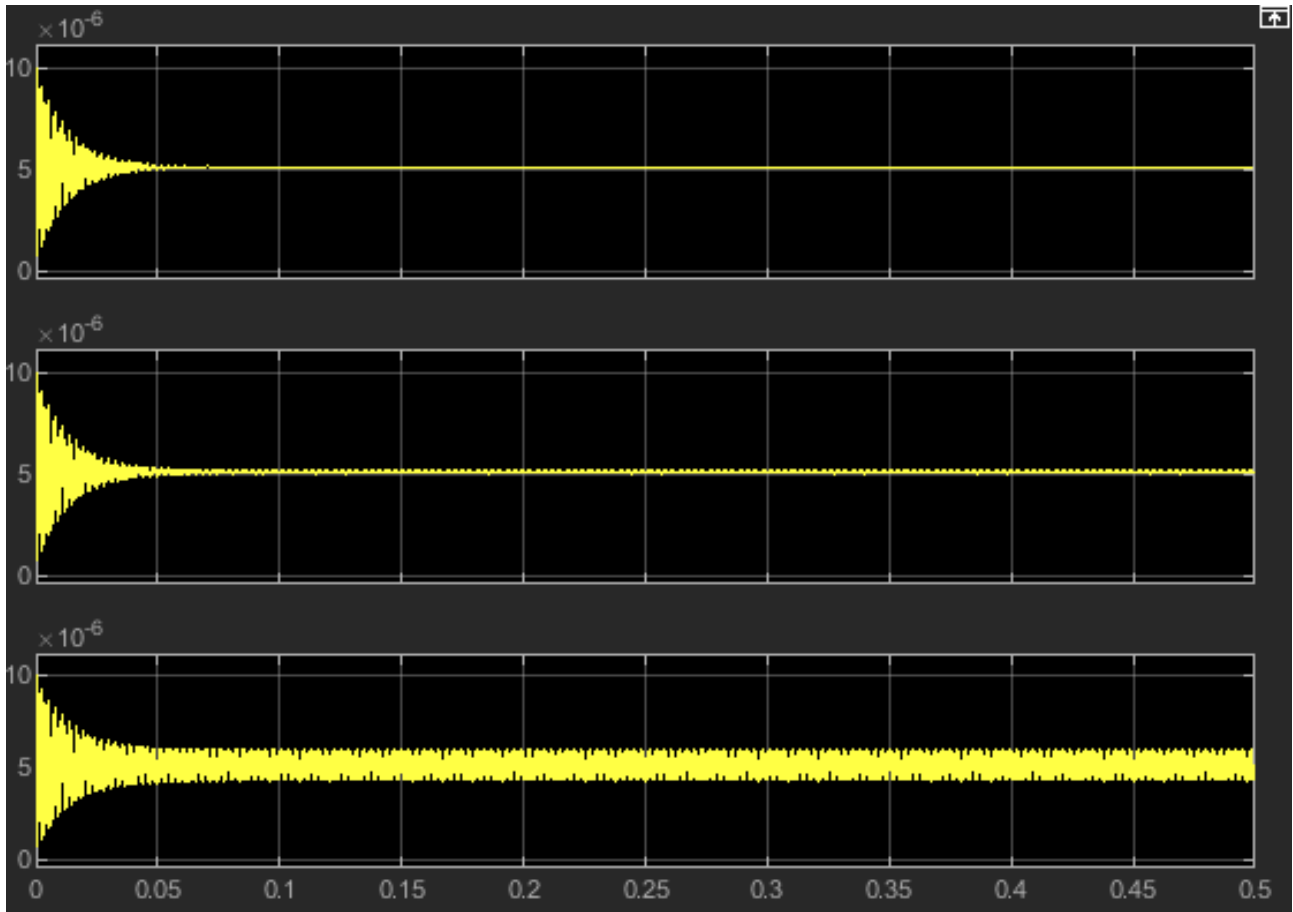
Figure 5.7: Simulink output for top: $b = 1e - 8[m]$, middle: $b = 2e - 8[m]$ and bottom: $b = 3e - 8[m]$

based on the condition for harmonic balance A_{lch}, leads to a percent error in the amplitude of:

$$\delta = \left| \frac{A_{lch} - A_{lcs}}{A_{lcs}} \right| \cdot 100\%$$

$$\delta = \left| \frac{3.3138e - 05 - 3.2995e - 05}{3.2995e - 05} \right| \cdot 100\%$$

$$\delta = 0.4334\%$$

Therefore it is concluded that the Simulink model works considerably well for simulating the results when dealing with friction-controlled backlash nonlinearities.

In addition to the time response, the FFT indicated by Figure 5.9b, for this system is analysed. It shows a single peak with a frequency of $f_{lcs} = 734.00[Hz]$. Again a comparison between the frequency obtained from the condition for harmonic balance f_{lch}, is compared to the frequency obtained fomr Simulink f_{lcs}, leading to a percent error in the frequency of:

$$\delta = \left| \frac{f_{lch} - f_{lcs}}{f_{lcs}} \right| \cdot 100\%$$

$$\delta = \left| \frac{733.34 - 734.00}{734.00} \right| \cdot 100\%$$

$$\delta = 0.046\%$$

The condition for harmonic balance, graphically indicated by Figure 5.8, therefore predicts the amplitude and frequency considerably well for friction-controlled backlash. It must be noted, that the peak
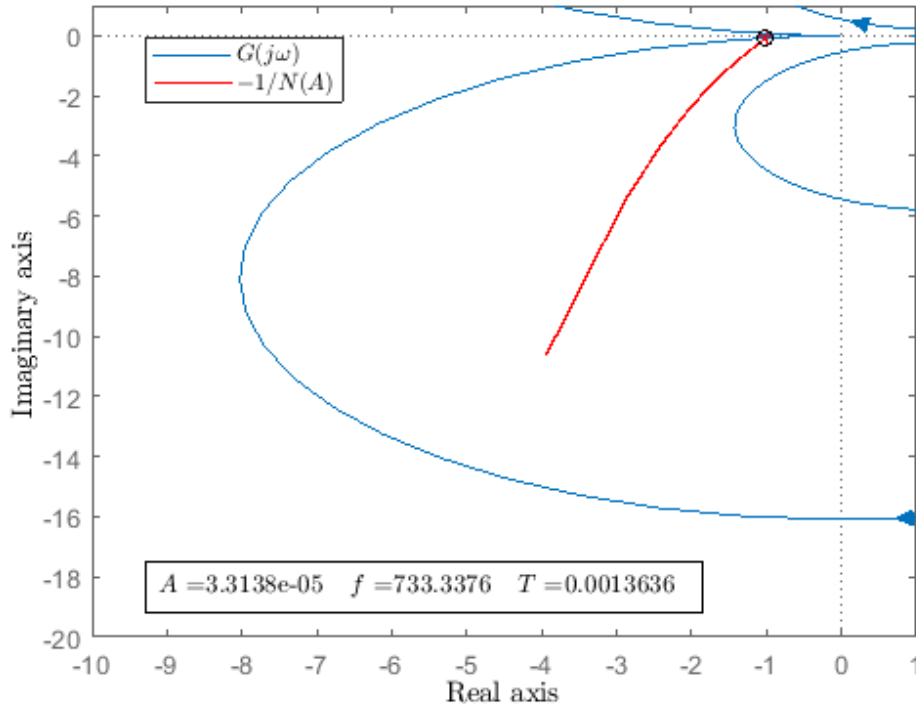
Figure 5.8: Transfer function with $-1/N(A)$, for friction-controlled backlash DF, where $b = 4e{-}6$[m]. Plot generated by Matlab.

in Figure 5.9b has a certain bandwidth, which results from the frequency resolution of the sampled data. The sampling frequency for this model was set to $F_s = 10002300$[Hz], while the number of samples was $N = 1000231$, based on a sampling interval of $0 \leq t \leq 0.1$[s]. According to Equation 3.1, the frequency resolution for the sampled model is:

$$\Delta f = \frac{10002300}{1000231} = 10[\text{Hz}]$$

A fundamental limitation of the frequency resolution is that it can only be increased if the sampling interval is increased.

The time response of Figure 5.9a showed that the limit cycle did no blow up as: $t \to \infty$ but stabilised, so based on that it can be concluded that the predicted limit cycle is stable. Stability in the framework of the condition for harmonic balance requires a neater explanation. The governing theory is described in subsection 2.3.6. In essence, this stability theory dictates that, to determine the stability of a predicted limit cycle, the operating point related to that limit cycle has to be perturbed in increasing direction of amplitude, and visualise where the perturbed operating point is located w.r.t. the transfer function. If the perturbed operating point is encircle by the transfer function, the limit cycle is unstable. Whereas it is stable if the perturbed operating point is shifted outside the transfer function. For the limit cycle shown in Figure 5.8, the operating point is perturbed outside the contour of the transfer function and hence the related limit cycle is stable.

Realistically, the width of the backlash is unknown and therefore varying values of b should be investigate. Increasing the backlash width even more leads to the creation of a second limit cycle. In addition, the width might increase over time due to wear and fatigue.

It must be noted that the DF, for friction-controlled backlash, is undefined if the amplitude is smaller than the backlash width $A \leq b$ since the eccentric pin does not touch the edges of the driving bridge.

(a) Time response

(b) FFT
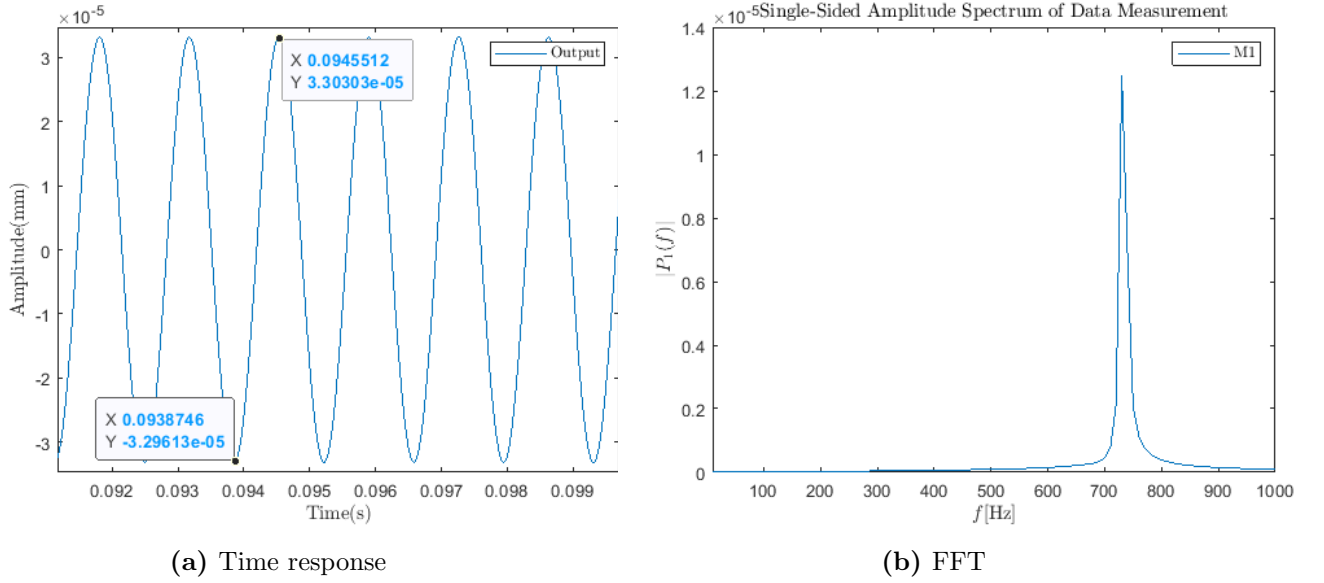
Figure 5.9: Zoomed in plot of Simulink friction-controlled backlash model, with $b = 4e - 6[\text{m}]$, FFT for friction-controlled Simulink model with $b = 4e - 6[\text{m}]$, and a sampling frequency of: $F_s = 10002300[\text{Hz}]$

Mathematically, this is defined as:

$$N(A) = \begin{cases} \text{undefined} & \text{if } A \leq b \\ \frac{1}{A}(b_1 + ja_1) & \text{if } A > b \end{cases} \tag{5.4}$$

where the corresponding Fourier coefficients are derived in subsection 2.3.4. Taking these coefficient in consideration shows that: $N(A) \propto \frac{b}{A}$, then the negative inverse of this DF:

$$-\frac{1}{N(A)} \propto -\frac{A}{b} \tag{5.5}$$

Equation 5.5 proves that for greater values of b, the inverse DF becomes more and more negative. Eventually the curve for $-1/N(A)$, will intersection a second time with the contour of the transfer function. To visualise this, the backlash width is increased by a factor of ten, resulting in $b = 4e - 5[\text{m}]$. For this value of backlash width, the transfer function with the $-1/N(A)$ is shown in Figure 5.10a, with the compute values for the amplitude and frequency related to this second limit cycle. That is $A_2^{lch} = 2.1089e - 5[\text{m}]$ and $f_2^{lch} = 533.22[\text{Hz}]$ respectively [6]. While the amplitude of the first limit cycle, analysed from Figure 5.8 previously, is scaled by factor of ten according to the increase of b by factor of ten, resulting an $A_1^{lch} = 3.3138e - 4[\text{m}]$. The frequency of that limit cycle remains constant since $N(A)$ is frequency independent, so $f_1^{lch} = 733.3[\text{Hz}]$. In Table 5.1, the characteristics of the two limit cycles that correspond to Figure 5.10a are enumerated.

Table 5.1: Properties of the limit cycles predicted by a backlash size of $b = 4e - 5[\text{m}]$

Limit cycle	$A_{lch}[\text{m}]$	f_{lch} [Hz]
1	3.3138e-4	733.33
2	2.1089e-5	533.22

---

[6]Now script denotes second limit cycle, while superscript denotes limit cycle predicted by the condition for harmonic balance

(a) Transfer function with $-1/N(A)$

(b) Time response simulink
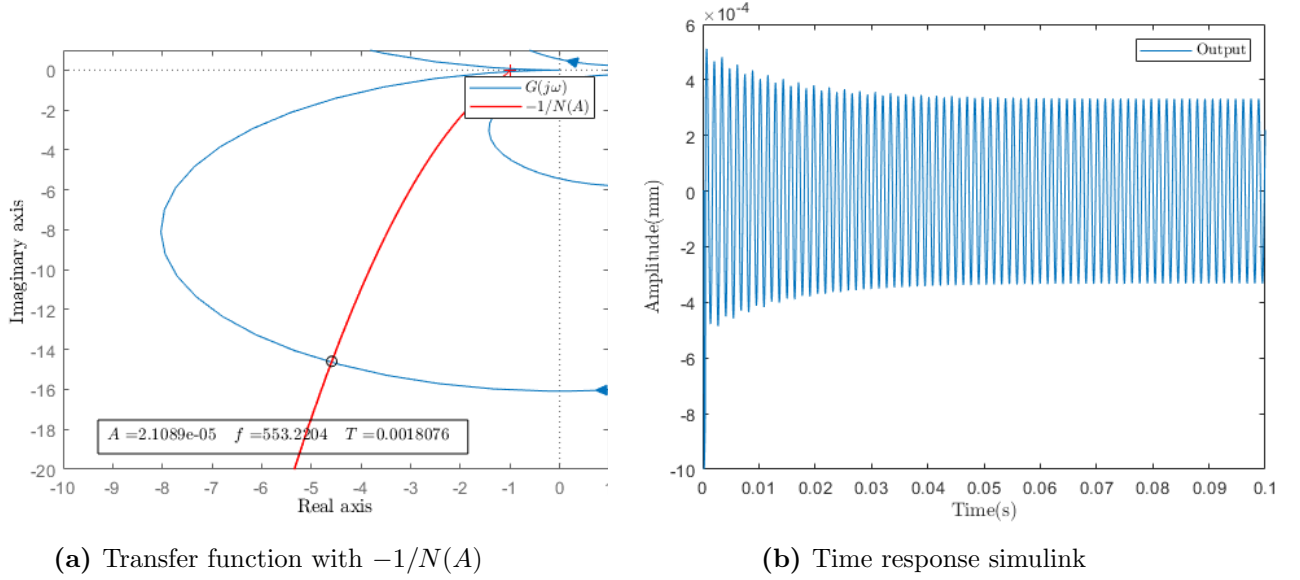
Figure 5.10: Graphical determination of the condition for harmonic balance with the related time response of Simulink for: $b = 4e - 5$[m]

For stability reason, it should already be noted that: $A_2^{lch} \leq A_1^{lch}$. But before evaluating the stability of the second limit cycle, the time response of the overall system is observed in Figure 5.10b resulting from the related Simulink model. The time response shows that a self-sustained oscillation exists, with an amplitude of: $A_{lcs} = 3.2995e - 04$[m], which is in agreement with the amplitude of the first limit cycle summarised in Table 5.1. In addition it has similar frequency of the first limit cycle, namely $f_{lcs} = 733.33$[Hz]. Furthermore, no additional peaks are observed in the related FFT, compared to: Figure 5.9b. This leads to the conclusion that the 'newly' established limit cycle is not visible in the system's time response. The stability of the limit cycles can be used to explain this intriguing observation. The initial limit cycle has already been determined to be stable. Similar to the first limit cycle, the second limit cycle's stability is examined by perturbing the corresponding operating point into increasing direction of A. As a result, the perturbed operating point is now encircled by the contour of the transfer function and hence in the unstable regime. There it will absorb energy, and move along the curve of $-1/N(A)$ until it settles in the operating point corresponding to the stable limit cycle. So, although the second limit cycle is unstable, it will shift it's operation point to the stable operating point. Therefore, only the amplitude and frequency corresponding to the first stable limit cycle are displayed in the results of Figure 5.10b. The aforementioned analysis is carried out for a range of backlash widths b, proving that a frequency independent stable limit cycle exist, related to the first operating point. A summary of the results is shown in Table 5.2. From Table 5.2 is is evident that there is a proportional relation between the size of b and the amplitude of the limit cycle A_{lc} since $b = 1e - 4$[m] predicts limit cycle with $A_{lc} = 0.00083$[m] and $b = 1e - 3$[m] predicts limit cycle with $A_{lc} = 0.0083$[m]. So increasing backlash by a factor of ten, results in an increase of the limit cycle by a factor of ten. An directly associated Simulink model has further validated these observation, shown in Appendix E. Further observation of Table 5.2, show that the predicted limit cycles are frequency independent, as expected according to the friction-controlled DF theory described in subsection 2.3.4.

With external input

In the above analyses, the system with a single nonlinear element and zero external input was analysed. Here the results when replacing zero external input reference signal $r(t) = 0$, with a sinusoidal external input, will be analysed. The external function results from the fact the real system is driving by a rotating motor. Given that the eccentricity of the pin has an amplitude of: $A_{motor} = 0.0015$[m], that

Table 5.2: Amplitude and frequency of predicted limit cycle for varying backlash widths

b[m]	A_{lc}[m]	ω_{lc} [rad/sec]	f_{lc} [Hz]
$1e-4$	0.00083	4.6e3	733
$2e-4$	0.0017	4.6e3	733
$3e-4$	0.0025	4.6e3	733
$4e-4$	0.0033	4.6e3	733
$5e-4$	0.0041	4.6e3	733
$6e-4$	0.0050	4.6e3	733
$7e-4$	0.0058	4.6e3	733
$8e-4$	0.0066	4.6e3	733
$9e-4$	0.0075	4.6e3	733
$1e-3$	0.0083	4.6e3	733

is rotating with a frequency of: $f_{motor} = 100$[Hz][7], this can be mathematically modelled as:

$$r(t) = 0.0015sin(2\pi100t) \tag{5.6}$$

It is expected that an equivalent limit cycle shows up in the time response of the system since friction-controlled DF is frequency independent. Similar to the closed-loop analyse above, a value of $b = 4e-5$[m] is chosen. Resulting in an equivalent graphical representation of the condition for harmonic balance shown in Figure 5.10a. These results are then compared to the results obtained from a related Simulink model with an open-loop configuration, similar to open-loop experiment The configuration is shown in Appendix C.5 by Figure C.5. Resulting in the time response shown by Figure 5.11, where the blue line indicates the output directly observed after the linear block, while the yellow line indicates backlashed output, similar to the backlashed output shown in Figure 2.9. From the time response it is observed that a base harmonic oscillates approximately between $[-0.001, +0.001]$[m], corresponding to the input amplitude of the driving function. In addition, the signal consist of sub oscillations. Obtaining the frequency of the additional harmonic, that might correspond to the limit cycle, is easily found by performing an FFT on this output signal (blue signal). A comparison is drawn between the closed-loop FFT and the open-loop FFT related to the blue signal in Figure 5.11. The comparison is presented in Figure 5.12 The open-loop FFT, shows that an additional peak is observed, with a frequency of $f \approx 100$[Hz]. The other peak in the FFT has similar frequency as the frequency corresponding to the limit cycle thus it can be concluded that a limit cycle, generated by backlash, can be either evaluated with the closed-, or open-loop configuration since they produce equivalent results in the FFT.

Another analysis can be performed on the open-loop configuration by changing the input amplitude A, while keeping the backlash size fixed. Resulting in the open-loop results shown in Appendix E. From the results it is concluded that the amplitude of the limit cycle scales is not altered by the driving amplitude, shown in Figure E.2.

5.2.2 Results : inertia-controlled backlash

Friction-controlled backlash assumes that the load (driving bridge) had no inertia since: $M = 0$. Equivalently, it can be said that the system experiences infinite friction. In contrary to friction-controlled backlash, inertia-controlled backlash assumes that the load has inertia thus $M \neq 0$, or

---

[7]From experiment it was observed that the frequency was actually higher namely: $f = 109.845$[Hz], but model was constructed before experiment
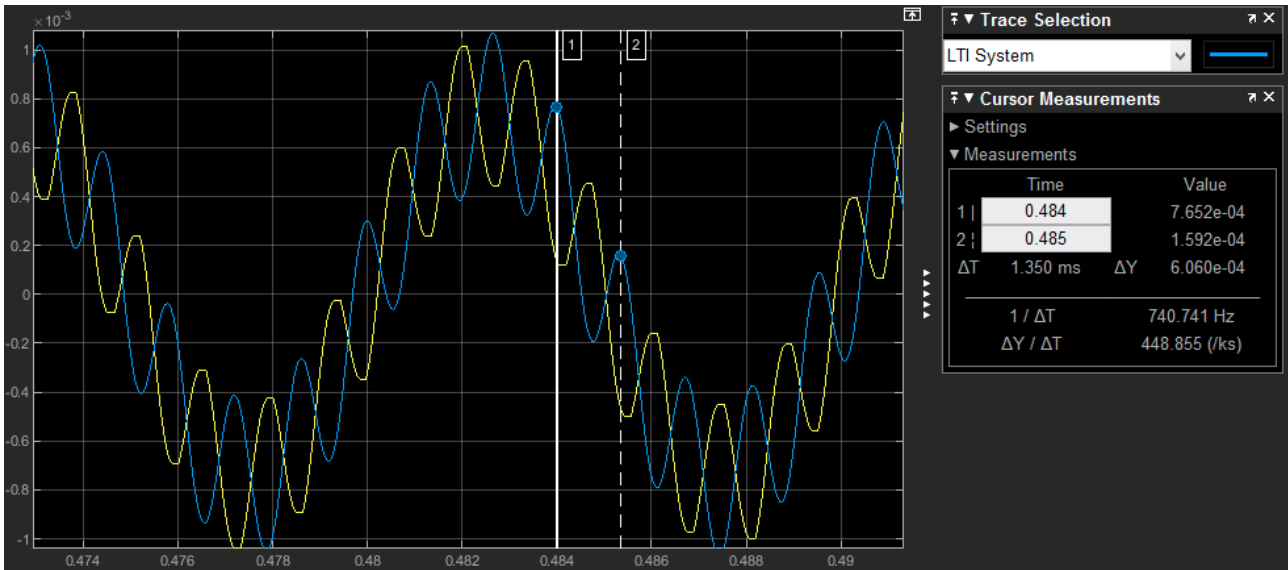
Figure 5.11: Time response with external driving function, for backlash width: $b = 4e - 5$[m]

$D = 0$. In the absence of friction, the load keeps on moving after motor and load separate. From theory, inertia-controlled backlash DF has been derived, corresponding to the code listed in Listing A.10. Additionally, it was shown that contact angle ϕ was dependent upon the ratio of b/A. To make the code easier to implement, this ratio is defined as: $\beta = b/A$ which make the DF $N(A) \to N(\beta)$. It should be noted that this ratio is is only defined on the range: $0 < \beta \leq 2$ since the total backlash gap has a length of $2b$ [8], therefore values $\beta \geq 2$ would make the DF obsolete.

A similar analyse as for friction-controlled backlash, is performed for inertia-controlled backlash. Meaning that the graphical representation of the condition for harmonic balance is compared to a related Simulink model. Since the DF is changed according to β the condition for harmonic balance (Equation 2.25), changes to:

$$N(\beta)G(j\omega) + 1 = 0 \tag{5.7}$$

graphically computing Equation 5.7 solves, for the ratio β and frequency ω. The graphical representation of Equation 5.7 is shown in Figure 5.13. From Figure 5.13 it is observed that one intersection appears, corresponding to a frequency of $\omega \approx 5120$[rad/s], that is $f_{lch} \approx \frac{5120}{2\pi} = [814.9]$[Hz][9]. The stability of this limit cycle is again determined by perturbing the operating point in the increasing direction of A. However, the DF itself is a function of $\beta = b/A$, and therefore the this direction has to be taken with care. Further investigating $-1/N(\beta)$ shows that the increasing direction of β tends to move away from $(-1, 0j)$-point and, thus the increasing direction of A has the tendency to move towards $(-1, 0j)$-point, similar to the increasing direction of A for friction-controlled backlash DF.

Since the operating point, corresponding to the limit cycle, shift outside the contour of the transfer function, this limit cycle is said to be stable. Similar to the analyses for friction-controlled backlash, a related Simulink model generates the time response and corresponding FFT. Here the nonlinear block, representing inertia-controlled backlash, is a self-defined Matlab function listed in Appendix A.11. For the open-loop configuration this results in the time response and FFT shown by Figure 5.16. Similar to the results obtain from Figure 5.11 for friction-controlled backlash, the open-loop configuration for inertia-controlled backlash shows additional oscillations, in the time response Figure 5.14a, as well. The frequencies of the additional oscillations are generated with a FFT shown in Figure 5.14b. This shows that, besides the harmonics corresponding to the driving frequency of $f = 100$[Hz], one

---

[8]For the inertia-controlled backlash derivation, a backlash gap of $2b$ was used, whereas the derivation of friction-controlled backlash assumed that the total width was b

[9]script from: f_{lch} stands for 'limit cycle based on condition for harmonics balance'
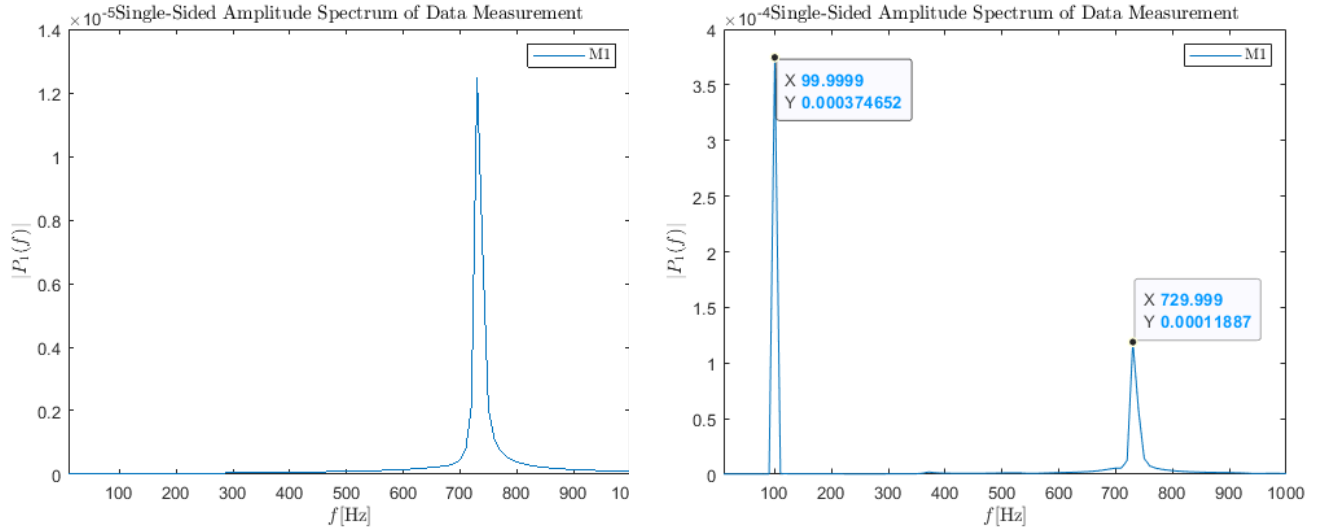
(a) Closed-loop without driving function, $b = 4e-6$[m]   **(b)** Open-loop with driving function, $b = 4e-5$[m]

Figure 5.12: Comparison between closed-, and open-loop FFT

additional harmonic is observed with frequency: $f_{lcs} \approx 659$[Hz]. Which corresponds to a limit cycle generated from the backlash nonlinearity. However, it is observed that the predicted limit cycle, based on the condition for harmonic balance, has a substantial higher frequency than the observed limit cycle based on the FFT from Simulink. The accuracy of the the results can be quantified according to:

$$\delta = \left| \frac{f_{lch} - f_{lcs}}{f_{lcs}} \right| \cdot 100\% = \left| \frac{814.9 - 660}{660} \right| \cdot 100\% = 23.47\%$$

Or in other words, the predicted limit cycle based on the condition for harmonic balance is 23.47% higher than the limit cycle observed in the Simulink model. A possible explanation for this is that the low-pass filtering hypotheses is only partially accomplished. Therefore the accuracy of the magnitude of the frequency of the predicted limit cycle based on the condition for harmonic balance, might be very different than the actual value. To illustrate this, if higher harmonics were included in the Fourier expansion leading the to coefficient for the DF, the contour of the DF would transform to a 2D 'line'. In doing so, it creates a certain 'ball' around the 1D DF, with a certain radius, resulting in a similar plot shown by Figure 5.15. From Figure 5.15 it can be observed that there is a certain range of frequencies corresponding to stable limit cycles if these higher harmonics were included[10] since intersections with the transfer function can now occur for frequencies: $4.6e3$[rad/sec] $\lesssim \omega_{lc} \lesssim 5.38e3$[rad/sec], translating this to f yields a bandwidth of frequencies, all corresponding to stable limit cycles:

$$732[\text{Hz}] \lesssim f_{lc} \lesssim 856[\text{Hz}] \tag{5.8}$$

5.2.3   Results : viscous-controlled backlash

The results when both friction and inertia act simultaneously on the driving bridge will now be analysed. Indicating a viscous-controlled backlash DF, for which the theory is derived in subsection 2.3.4, leading to $M \neq 0$ and $D \neq 0$. In contrary to the previous DF, this DF is frequency dependent,

---

[10]Figure 5.15 is an example and does not correspond to the actual higher harmonics DF for inertia-controlled backlash
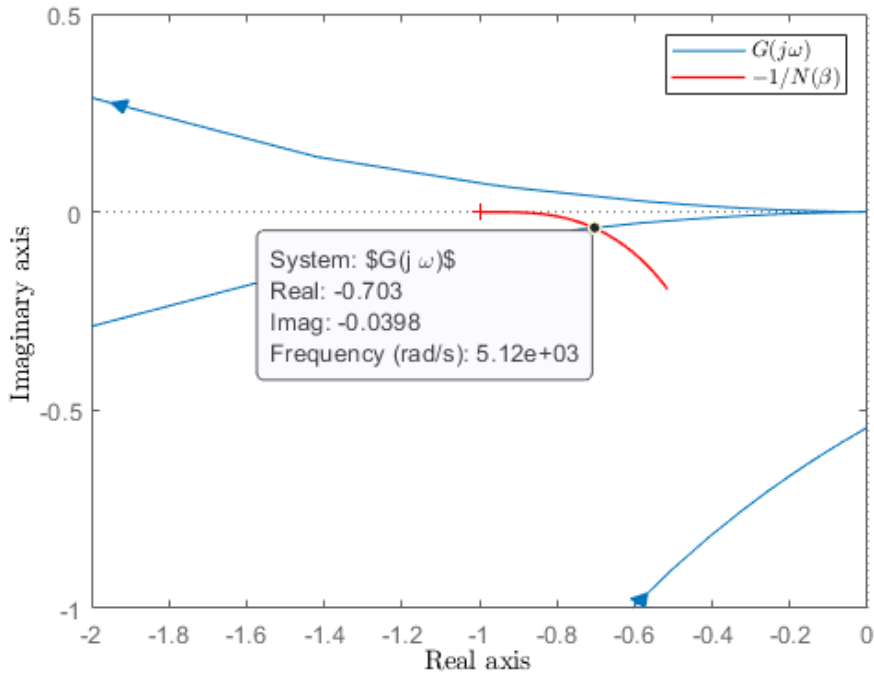
Figure 5.13: Inertia-controlled backlash DF with transfer function loci

resulting form from the separation angle between motor and load according to:

$$
\begin{aligned}
\phi_s &= \tan^{-1}\left(\frac{1}{\gamma}\right) \\
\phi_s &= \tan^{-1}\left(\frac{D}{M\omega}\right)
\end{aligned}
\tag{5.9}
$$

So for fixed values of M and D, increasing the driving frequency leads to relatively smaller separation angle, on which the derivation of the input-output wave characteristic, shown in Figure 2.11, is derived. As a consequence the from the that input-output wave characteristic. Generally, the ratio between M and D hard to obtain since the the backlash nonlinearity is a very complex component. Similar to inertia-controlled backlash, the contour for the DF is generated for the ratio of $\beta = b/A$ instead of A. In addition to β, the viscous-controlled DF is based on the frequencies ω, that is scaled according to the ratio for M/D since to $\gamma = \frac{M}{D}\omega$. Hence the DF becomes: $N(\beta, \gamma)$. Where the values for $0 < \beta \leq 2$ and the values for $\gamma > 0$. Figure 5.16a shows the transfer function with plotted with $-1/N(\beta, \gamma)$, for some random values of β. The increasing direction is A is again determined by the observation the the loci for increasing values of β have the tendency to move to the RHS of Figure 5.16a, hence the increasing direction of A is the opposite of β, in the direction towards the point of $(-1, j0)$, similar the inertia-controlled backlash. Further investigation of Figure 5.16a shows that if $\gamma \to \infty$, the loci has the tendency to shift to the contour for inertia-controlled backlash, whereas $\gamma \to 0$, the contour has the tendency to shift to the curve for friction-controlled backlash. This observation proves that the contour for viscous-controlled backlash is bounded by the contours of friction-, and inertia-controlled backlash. Due to the complexity of the DF for viscous-controlled backlash, the associated code is expensive and thus has a high computational time. Therefore the range of γ is limited by randomly selected values, such that:

$$
1 < \gamma < \frac{3}{2}
$$

(a) Time response

(b) FFT
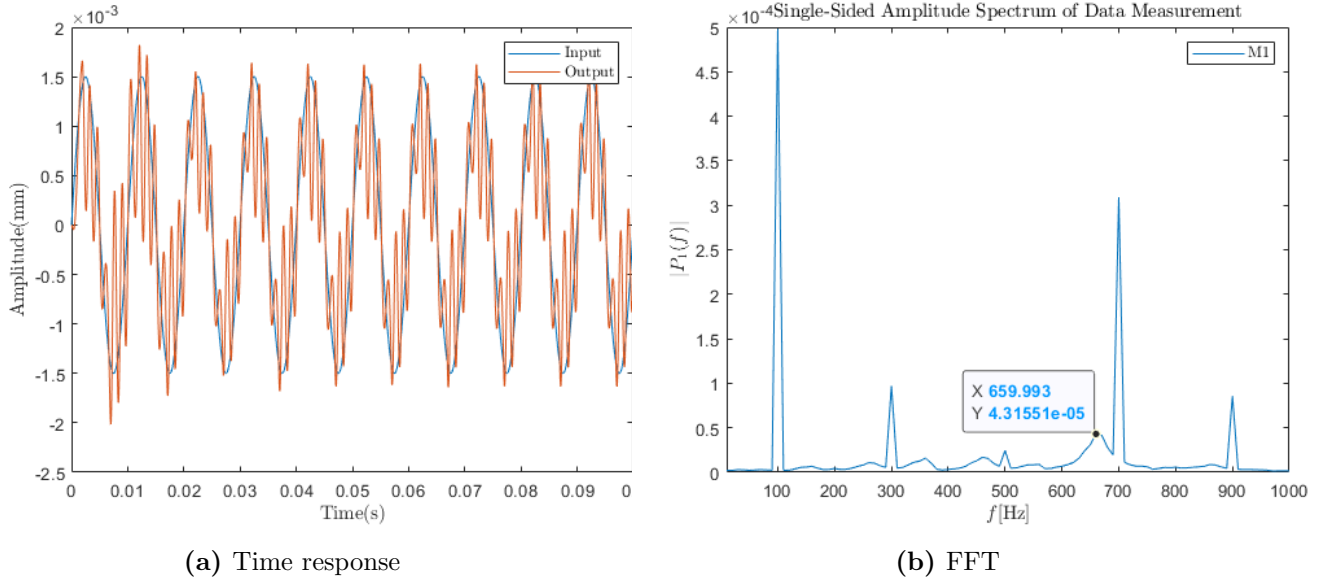
Figure 5.14: Results from Simulink model for inertia-controlled backlash in open-loop configuration

Since the contours for friction-, and inertia-controlled backlash are presented in the preceding sections, it is now possible to plot these contour to the same graph as the contour for viscous-controlled backlash, shown in Figure 5.16b. The thick red lines denote the contours for friction-, and inertia-controlled backlash, whereas the thinner lines correspond to contours for viscous-controlled backlash.

From Figure 5.16b it is observed that the contour of viscous-controlled backlash - no matter the model parameters used for viscous-controlled backlash - potentially only intersection with the inner circle of the transfer function. However, this intersection is entirely enclosed by the outer circle of the transfer function and Nyquist stability it is then concluded that all these potential limit cycles resulting from these intersections are considered to be unstable. Taking the increasing direction of A into account, similar to the analyses related to Figure 5.10b, leads to the conclusion that these unstable limit cycle eventually merge to the set of stable limit cycle near $(-1, j0)$-point. Thus for this system there will only be stable limit cycles, shown in the time response, with frequencies that are bounded by the frequencies of the limit cycle predicted by either friction- and inertia-controlled backlash. In some sense there is a certain 'bandwidth' of frequencies, corresponding to a stable limit cycle, for limit cycles. This is illustrated in Figure 5.17. Whether limit cycles exist in the first place, still depends on the backlash width. But if limit cycles are observed in the frequency response, the corresponding frequencies of that limit cycle should be in the range of:

$$733[\text{Hz}] \lesssim f_{lc} \lesssim 815[\text{Hz}] \tag{5.10}$$

corresponding to the bandwidth of stable limit cycles, denoted by the arrow in Figure 5.17. So although, viscous-controlled backlash is dependent upon the ratio of M and D (which is fundamentally unknown) and dependent upon the driving frequency ω it is possible to say something about the potential limit cycles. Namely, that the frequencies of these limit cycles should be in the range of Equation 5.10. Designing an experiment is one method for figuring out how friction affects the limit cycles that backlash predicts. A certain degree of backlash is intentionally added to the driving bridge in this experiment. Subsequently, the time response of this experiment is analysed with a FFT. For example, it showed that a limit cycle with: $f_{lc} = 760[\text{Hz}] \rightarrow \omega = 4775[\text{rad/sec}]$ and a corresponding amplitude A occurred. Given the b and the driving frequency the condition for harmonic balance can be numerically solved for the ratio M/D to determined how friction is affecting the backlash
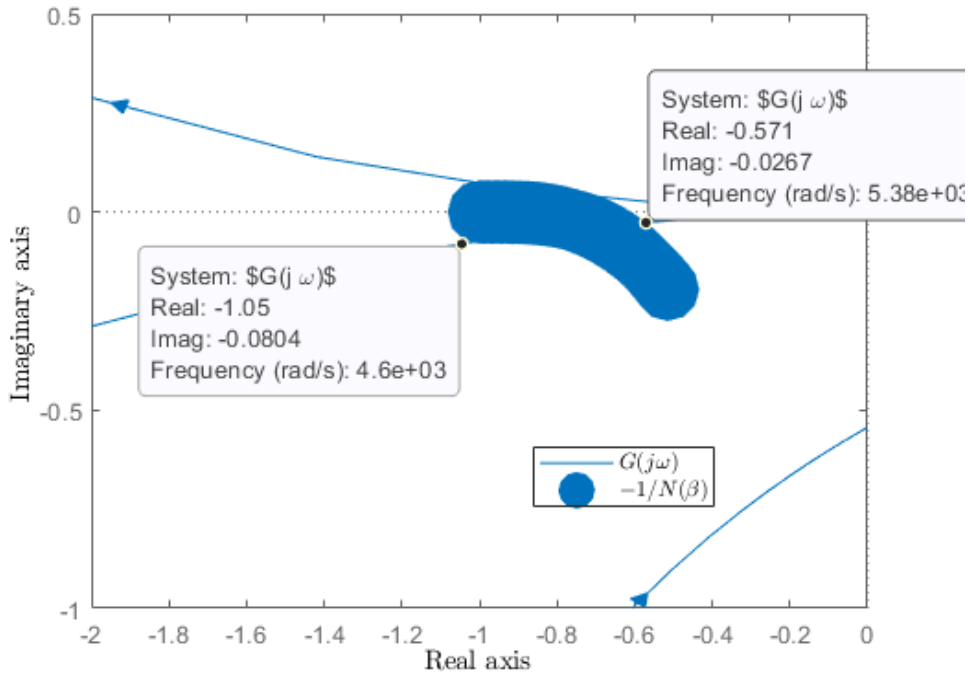
Figure 5.15: Example of inertia-controlled backlash including higher harmonics

nonlinearity. In other words, the condition for harmonic balance denoted by Equation 5.11:

$$N\left(\frac{b}{A}, \frac{M}{D}\omega\right) G(j\omega) + 1 = 0 \tag{5.11}$$

can be numerically solved for this experiment. The hypothesis that backlash in the trimmer behaves more like friction-controlled backlash than like inertia-controlled backlash can be validated by this experiment.

5.2.4 Results : Coulomb friction backlash

In subsection 2.3.5 the DF for Coulomb code was derived. Remember that the DF for Coulomb friction was purely real,

$$N(A) = \frac{4F_c}{\pi A}$$

therefore the negative inverse of the DF traces a line on the real-axis in the complex-plane. Which in turn indicates that, on order to find limit cycling behaviour, the linear transfer function has to 'cross' the negative real-axis at some point. From the Nyquist plots of the transfer function, it was already observed that this is not the case for the transfer function associated to the trimmer. Therefore, it is possible to generalise a statement of potential limit cycling behaviour: the negative inverse DF does not intersect with the linear transfer function for trimmer dynamics, hence no limit cycle is predicted. This has to be verified with experiment. Once again the transfer function is plotted with the contour of $-1/N(A)$, resulting in Figure 5.18: From the graphical representation of the condition for harmonic balance, shown by Figure 5.18, no limit cycle is predicted. This is in agreement with the results from the first experiment of section 3.2, where no additional harmonics were found apart from the harmonics corresponding to the fundamental harmonic.

Similar to the results for backlash, a Simulink model is created in feedback configuration to validate

(a) Viscous-controlled loci

(b) Friction-, inertia-, and viscous-controlled loci
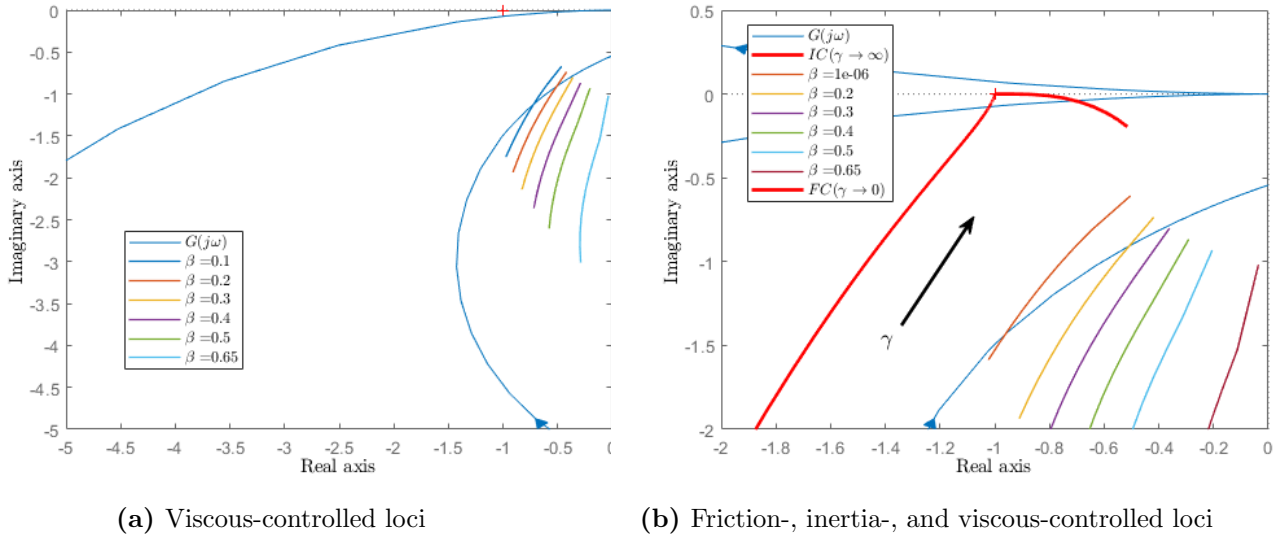
Figure 5.16: Transfer function with contour for viscous-controlled backlash: $-1/N(\beta, \gamma)$

that no limit cycles are induced by Coulomb friction. Appendix C.5, shows an equivalent closed-loop configuration to generate the time response for the Coulomb friction nonlinearity. An ideal relay is used as the nonlinearity related to Coulomb friction. The time response with associated FFT is shown in Figure 5.19. In contrast to the hypothesis that Coulomb friction DF, does not induce limit cycling behaviour since the DF does not have imaginary part and therefore does not intersect with this transfer function, the time response shows an additional oscillation in Figure 5.19a. A potential explanation is that, follows from the observation that the contour of $-1/N(A)$ asymptotically merges with the contour of the transfer function near the origin, shown in Figure 5.18. Previously, it has been shown that the introduction of higher harmonics graphically transformed the 1D line segment of the DF to a thicker 2D line segment on the complex plane. Taking that into consideration, the transfer function might intersect with $-1/N(A)$, near the origin since the thickness considerably small. In addition, for increasing frequency the transfer function spirals into

$$\lim_{\omega \to +\infty} G(j\omega) \to (0, 0j) - \text{point} \tag{5.12}$$

High frequency limit cycles are therefore anticipated, which are precisely observed in Figure 5.19b. This observation is further evaluated by changing the ideal relay nonlinearity with the built-in component 'Coulomb & Viscous' friction. Furthermore, the Coulomb friction coefficient is increased to $F_c = 1.5[-]$ and a viscous friction component of $F_f = 0.1[\text{Ns/m}]$, resulting in a shorter path length over the negative real-axis for the contour of the DF, since:

$$-\frac{1}{N(A)} = -\frac{A\pi}{4F_c} \tag{5.13}$$

In addition, instead of the open-loop configuration a closed-loop configuration is simulated with an impulse response, resulting in Figure 5.20.
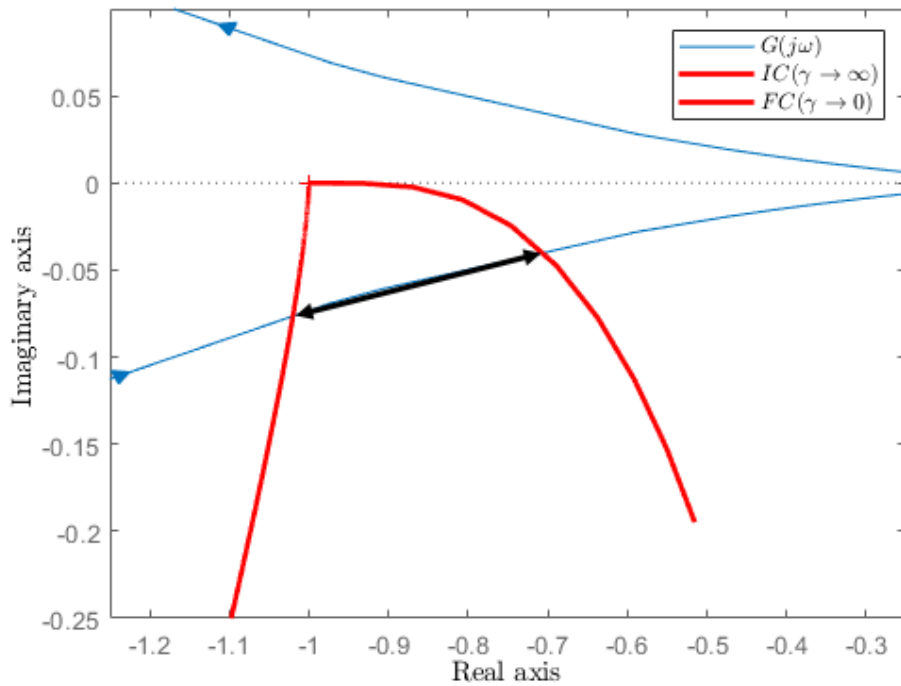
Figure 5.17: Bandwidth for range of stable limit cycles
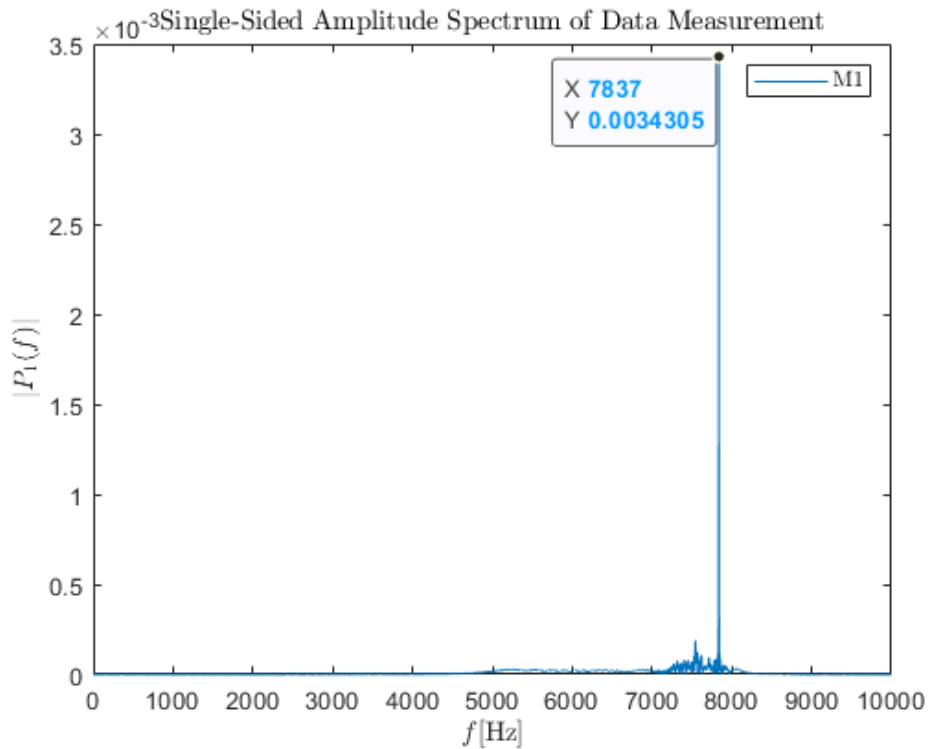
Figure 5.20: Closed-loop FFT for impulse response of the 'Coulomb & Viscous' built-in nonlinearity, with $F_c = 1.5$[-] and $F_f = 0.1$[Ns/m]

From the figure Figure 5.20 it is concluded that the impulse response show similar results as for the
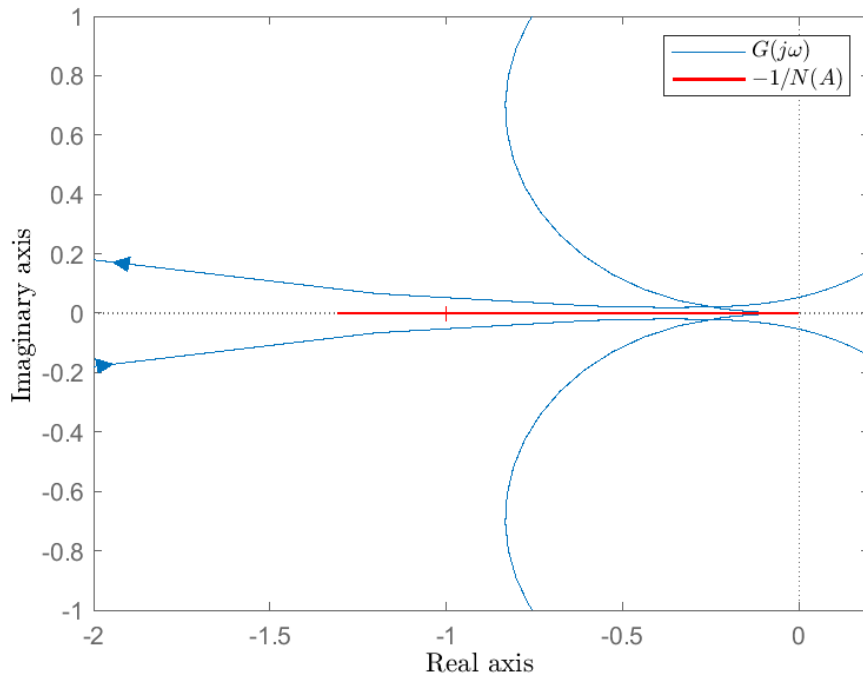
Figure 5.18: Transfer function with negative inverse of the Coulomb DF on the complex plane, where $F_c = 0.015$[-]

FFT obtained from the closed-loop configuration. Further investigation of the system subjected to impulse response, shows that the amplitude of the predicted limit cycle scales in linear fashion with F_c. For example increasing F_c by factor 10 results an increase of the amplitude by factor 10 as well. A realistic value of the Coulomb friction, which is assumed to be below 1.0[N], show high frequency limit cycles but with extremely small amplitude and therefore Coulomb friction nonlinearity might be neglected when predicting limit cycles.

5.2.5   Results : equivalent nonlinearity backlash

Finally, the results for the equivalent nonlinearity between friction-controlled backlash and Coulomb friction are analysed, that result from the theory described in section 2.4.

It was assumed that the backlash component in the trimmer is friction-controlled since the frictional forces between the cutter and guard are relatively high. As briefly mentioned, Simulink DF is derived on the input-output wave characteristic of the relevant nonlinearity. Unfortunately, this has not been achieved for the equivalent nonlinearity, however the DF in terms of frequency response can still be derived. Equation 2.58 shows that the inherent nonlinearity, which is Coulomb friction, has to be adjusted by $1/G_g(s)$ to account for the fact that Coulomb friction is velocity dependent, whereas backlash is positional dependent. This results to the following modified inherent nonlinearity for

(a) Time response

(b) FFT
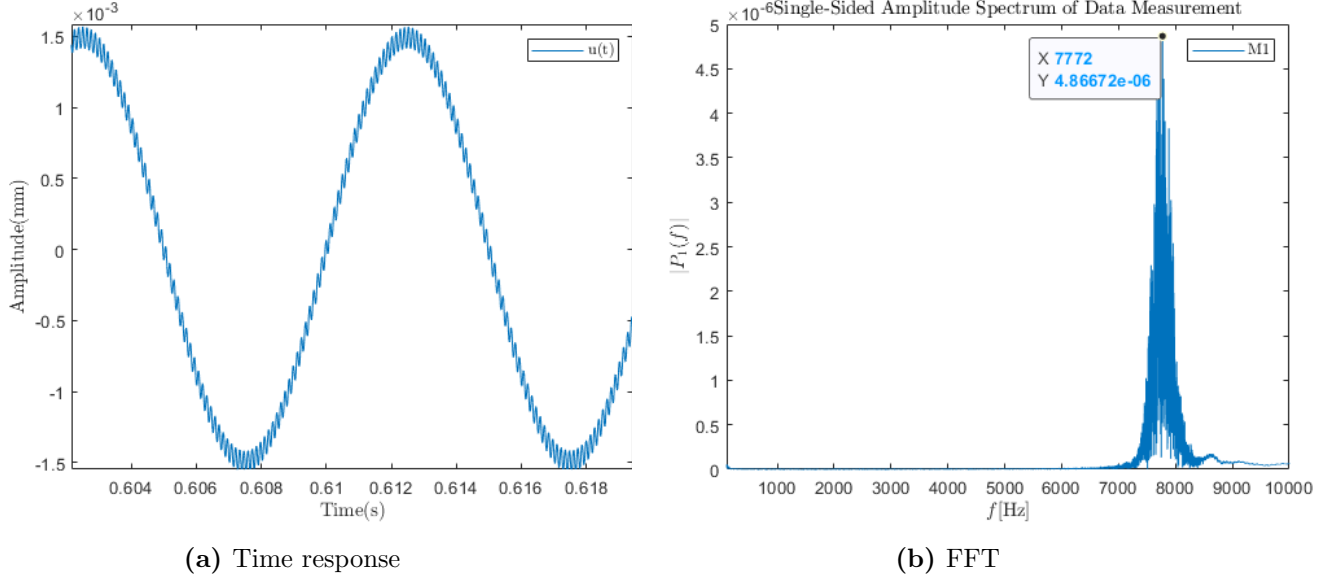
Figure 5.19: Open-loop Simulink output for Coulomb friction, with $F_c = 0.015$[-]

Coulomb friction as:

$$\frac{1}{G_g(j\omega)} N_f(A) = \frac{1}{G_g(j\omega)} \frac{4F_c}{A\pi}$$

$$\frac{1}{G_g(j\omega)} \frac{4F_c}{A\pi} = \frac{1}{j\omega} \frac{4F_c}{A\pi}$$

$$= -j\frac{4F_c}{\omega A\pi}$$

Combing this to the intentional nonlinearity $N_r(A)$, for friction-controlled backlash, leads to the following - frequency dependent DF - equivalent nonlinear DF:

$$N_{eq}(A,\omega) = \frac{1}{A}\left(\frac{\pi}{2} - \sin^{-1}\left(\frac{2b}{A} - 1\right) - \left(\frac{2b}{A} - 1\right)\sqrt{1 - \left(\frac{2b}{A} - 1\right)^2}\right.$$
$$\left. + j\left(\frac{4b}{\pi}\left(\frac{b}{A} - 1\right) - \frac{4F_c}{\omega A\pi}\right)\right) \tag{5.14}$$

Since this DF is frequencies dependent, a variety of contours with changing frequencies is generated, similar to the results for viscous-controlled backlash. A large variety of potential contours for the equivalent nonlinearity is possible since ω, F_c and b can all change. Some of the results are summarised in Figure 5.21.
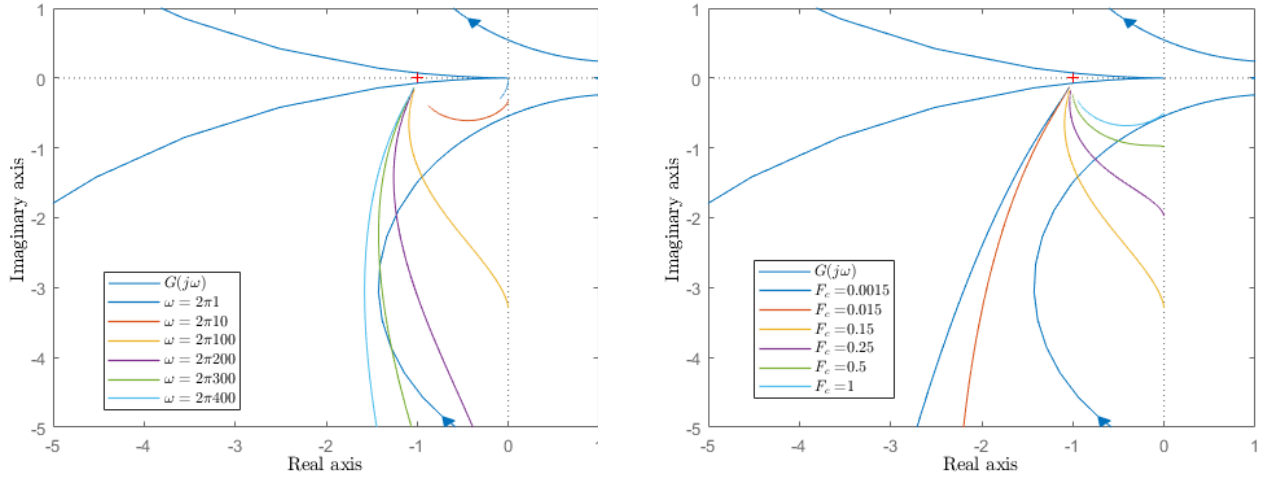
(a) Change in ω, with $F_c = 0.15$ and $b = 200e - 5$

(b) Change in F_c, with $\omega = 2 \cdot \pi 100$ and $b = 200e - 5$
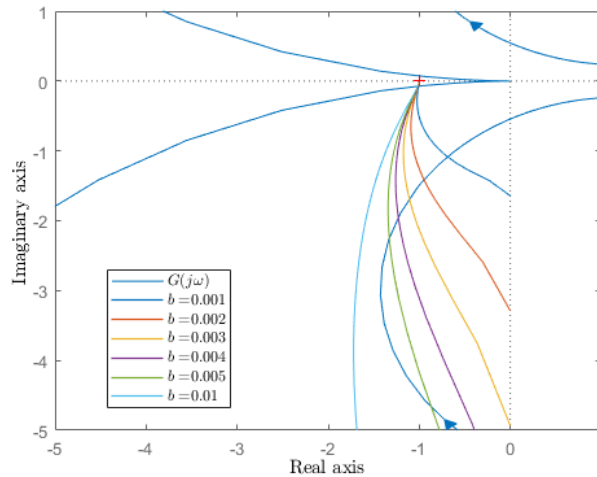
(c) Change in b, with $F_c = 0.15$ and $\omega = 2 \cdot \pi 100$

Figure 5.21: Contour of the equivalent nonlinearity, for change model parameters

From Figure 5.21a it is observed that increasing ω leads to a similar contour for the DF as for friction-controlled backlash since the additional imaginary term in Equation 5.14, vanishes:

$$\lim_{\omega \to \infty} \left(\frac{4F_c}{\omega A \pi} \right) = 0$$

therefore the DF for the equivalent nonlinearities reduces to the DF for friction-controlled backlash. Taking the limit for F_c to infinity, shows that the imaginary term, resulting from friction-controlled backlash, becomes marginal compared to the Coulomb friction term.

Figure 5.21b and Figure 5.21c show the resulting contour for the equivalent nonlinearity when changing the F_c and b respectively. Note that these changes show similar behaviour as for viscous-controlled backlash DF described in subsection 5.2.3. In addition, for some model parameters it is possible to observe multiple intersections (limit cycles) between the transfer function and the negative inverse of the DF, however the associated operating point tend to move to $(-1, 0j)$-point, if the operating point is perturbed. Resulting in a bandwidth of stable intersection, similar to Figure 5.17.

In subsection 5.2.1, it was shown that for friction-controlled backlash, with $b = 4e - 6[m]$, a limit cycle

occurred with $A_{lch} = 3.313e - 5$[m] and frequency $f_{lch} = 733.3$[Hz]. These observation are now further compared to the results from the equivalent nonlinearity. Since the equivalent nonlinearity reduces to the friction-controlled backlash as $F_c = 0$, it is expected that for these model parameter equivalent limit cycling behaviour is predicted. The result is shown on Figure 5.8.
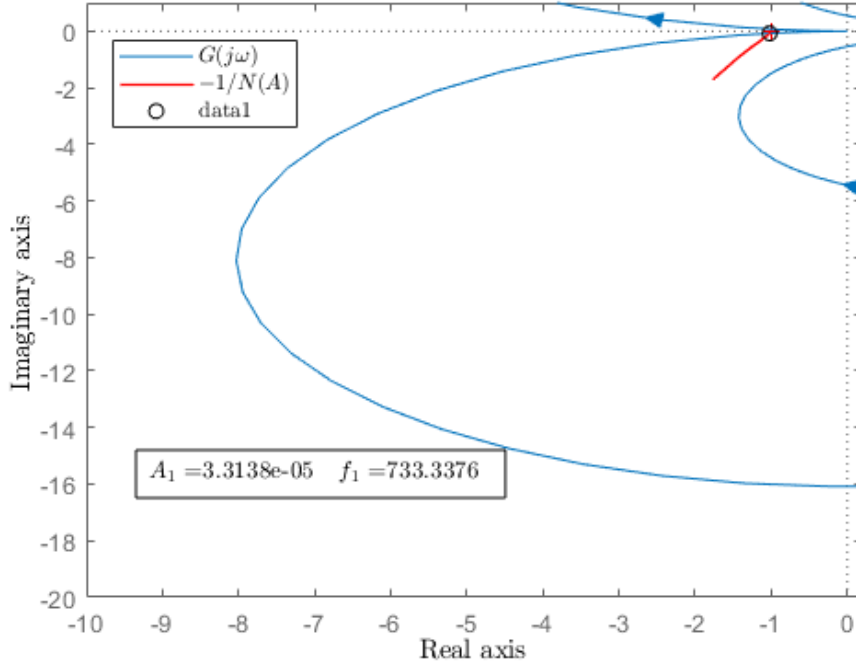
Figure 5.22: $b = 4e - 6$[m], $F_c = 0$[-]

Although the contour for $-1/N(A, \omega)$ has a shorter path length, it traces the exact curve for the friction-controlled backlash DF. Hence it intersects with the transfer function at the same location, and therefore it predicts a limit cycle with equivalent properties as the friction-controlled DF did. However, from Figure 5.21b it is observed that the contour of the DF changes rapidly, when Coulomb friction is introduced to the system. It was assumed that realistic value of Coulomb friction is below 1.0[N]. Applying $F_c = 0.6$ and $\omega = 200\pi$, the to DF results in the contour, with the associated FFT obtained from the related closed-loop Simulink model, are shown in Figure 5.23

Figure 5.23a shows that 1 intersection occurs, therefore 1 limit cycle is predicted, with frequency $f_{lcs} = 737.514$[Hz]. The frequency of this limit cycle is thus:

$$\delta = \left| \frac{737.514 - 733.33}{733.33} \right| \cdot 100\%$$

$$\delta = 0.5705\%$$

higher than the frequency of the limit cycle predicted for friction-controlled backlash. Resulting from the fact the contour corresponding to the equivalent nonlinearity with $F_c = 0.6$, intersects with the transfer function at a slightly higher frequencies, shown in Figure 5.24.

(a) C. equivalent nonlinearity

(b) FFT
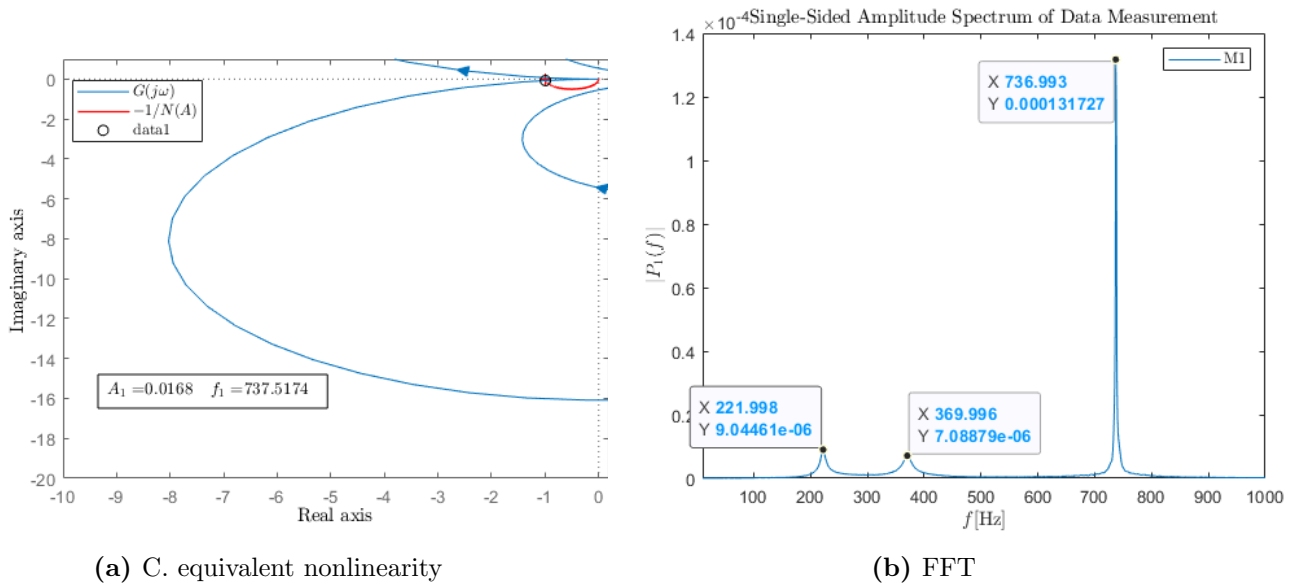
Figure 5.23: Closed-loop Simulink for equivalent nonlinearity, with $b = 4e - 6$[m] and $F_c = 0.6$[-]
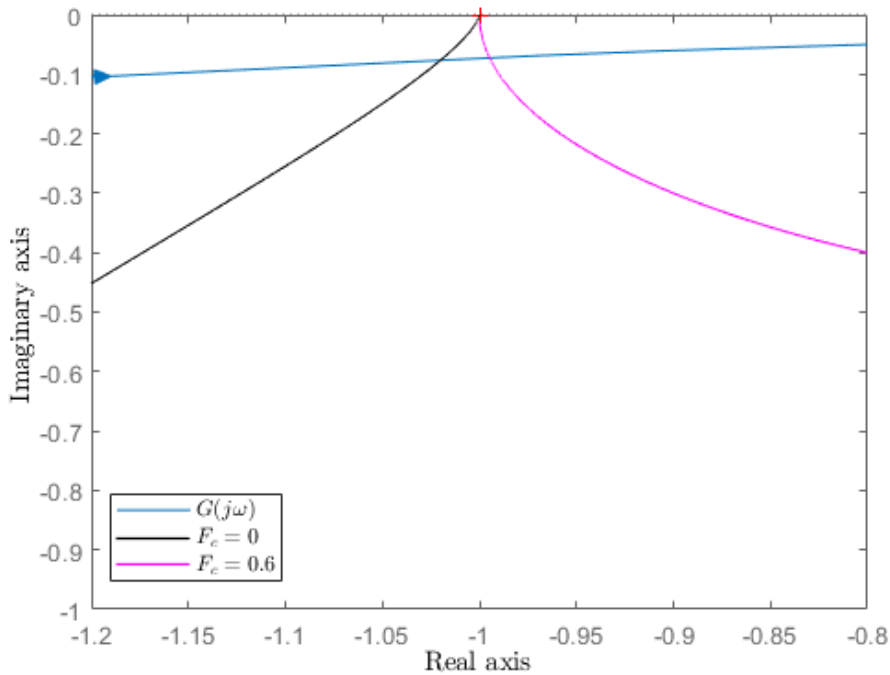
Figure 5.24: Comparison for contours obtained for equivalent nonlinearity, with $b = 4e - 6$

However, the amplitude of limit cycle has changed significantly since the the DF has changed significantly as well. A closed-loop configuration in Simulink, is used here to obtain the FFT shown by Figure 5.23b. The FFT shows that a peak occurs at $f_{lcs} = 736.993$[Hz], which corresponds to the frequency of the limit cycle. Besides that frequency, two more peaks are observed in the FFT, with frequency $f_1 = 221.989$[Hz] and $f_2 = 369.996$[Hz], where the latter is a harmonic generated by the frequency of the limit cycle since $\frac{736.993[\text{Hz}]}{369.996[\text{Hz}]} \approx 2$.

Chapter 6

Discussion & Recommendations

Considering the distinct cases for DF analysis led to the observation that for all cases, one or under strict conditions 2 limit cycles were predicted. Friction-controlled backlash showed that a stable limit cycle was predicted with a frequency of $f \approx 733$[Hz]. Inertia-controlled predicted a slightly higher frequency limit cycle $f \approx 815$[Hz], while the DF's for the viscous-controlled backlash illustrated that the range of frequencies for which stable limit cycles can occur, are in fact bounded by the contours of the DF's for friction- and inertia-controlled backlash. It is then discussed that, even though unstable limit cycles might exist, that the time response associated to that model only showed stable limit cycle in the vicinity backlash. This results from the observation that the potential unstable limit cycles all have the tendency to shift towards to 'band' of stable limit cycles, by perturbing the amplitude of the operating point. This results from the inherent property that these intersections are all encircled by the outer radius of the transfer function and hence all these intersection are considered to be unstable based on the Nyquist stability criterion.

Another restriction, such that limit cycles were not present in the Simulink model for backlash, is that the width of the backlash component should: $b \lesssim 2e - 8$[m]. Values greater than this value already should undesired limit cycles. However, from experiment it was observed that for values of $b = 200e - 6$, which is a lot larger than previously mentioned value of b, no limit cycles were observed in the system. Indicating that the friction between the cutter and guard attenuates the magnitude of the predicted limit cycle. Since the backlash component is complex by nature, it is impractical to predict the precisely value for which limit cycles exist in the first place. In the results of viscous-controlled backlash, an experimental study is proposed to evaluate how friction is affecting the backlash component and hence the predicted limit cycle.

Another consideration that has to be taken into account is that the experimental results were manually calibrated. Potentially resulting in inaccuracy in terms of absolute magnitude of the oscillating motion between the cutter and guard. But does not result in inaccuracy in terms of the frequency of that oscillating motion. In other words, the peaks in experiment's FFT are not subjected to inaccuracy in terms of frequency, but are inaccurate in terms of absolute magnitude. This is a desired observation since the frequency of the possible limit cycles is important rather than their amplitude.

Given the fact the DF method is a approximate study, there is more to say about the inaccuracy. A vital consideration of approximate studies is the consideration of error bounds [19]. However, literature has shown that is is almost impractical to derive error bound equations for the DF.

6.1 Limitations of applicability - odd nonlinearities

The fundamental assumption for the derivation of the DF method, was that a self-sustained oscillation exists in the first place. For which the shape of the oscillation is governed by a perfect sinusoid. Unfortunately, this does not always apply to limit cycle, as the Van der Pol oscillator has shown.

In addition, the derivation of the DF only applies to hard-nonlinearities. Indicating that non all

nonlinear components can be approximated with a DF. Hard-nonlinearities can be considered as on-off nonlinearities. In other words, the have the property that they are piece-wise linear. Friction-controlled backlash is a good illustration of an on-off nonlinearity, but inertia-controlled backlash already shows that input-output relation is not perfectly linear when eccentric pin and driving bridge are in contact hence for this type of backlash the DF less applicable than for friction-controlled backlash. Similar analyse applies to viscous-controlled backlash. For Coulomb friction, the derivation of the DF relied on the assumption that Coulomb friction could be modelled as an ideal relay, and hence the nonlinearity as an on-off nonlinearity. Realistically, the friction between the cutter ans guard have a nonlinear viscous term as well an thus the input-output relation is not perfectly linear.

Finally, the derivation of the DF only applies to odd-nonlinearities, such that the static term of the Fourier expansion vanishes $a_0 = 0$, leading to the Fourier expansion that only contain a_1 and b_1 term.

6.2 Limitations of performance - filtering hypothesis

Odd-nonlinearities indicate that the static term in the Fourier expansion vanishes, indicating that only a_1 and b_1 are left behind. Unfortunately, this is not the whole story. As mentioned throughout this research, the filtering hypothesis must be also be accomplished such that the higher terms of the Fourier expansion are completely attenuate, such that $a_n = 0$ and $b_2 = 0$ for $n = 2, 3, ...$ Only than the condition for harmonic balance is accurate. Even for very small higher-ordered terms, inaccuracy arises and the predicted limit cycles, based on this condition, are inaccurate. Resulting in the conclusion that more accurate results are achieved the more the transfer function behaves like a low-pass filter. From the Bode plot, related to the frequency response of the linear transfer function of the trimmer, it has been determined that the 'filtering order' is approximately 1. This indicates that this transfer function is on the edge of filtering out the higher harmonics. Moreover, the model parameters on from which the transfer function is derived, have an inherent inaccuracy and therefore it is possible to that the filtering hypothesis might not completely be achieved. A consequence if the filtering hypothesis is not entirely achieved, was illustrated in subsection 5.2.2. It showed that inclusion of the higher harmonics could potential make the line of the negative inverse of the DF thicker, and hence intersection(s) between the transfer function and the negative inverse of the DF to occur somewhere else. Hence the properties of that limit cycle might deviate from the observed limit cycle. Based on this, the following conclusion are made with the consideration that higher harmonics were excluded in the derivation of the DF:

1. The amplitude and frequency of the predicted limit cycle are not accurate

2. A predicted limit cycle does not actually exist

3. An existing limit cycle is not predicted

Another restriction for the applicability of the DF has to considered, related to the filtering hypothesis. In literature it has been shown that the DF method erroneously predict limit cycles if the plots of the contours of the transfer function and the negative inverse of the DF nearly tangent [20]. This has be taken into account when modeling trimmer dynamics, and can be easily verified by plotting of the associated backlash DF and transfer function.

6.3 Validity of assumptions

During this research it was assumed that backlash in the trimmer, can best be modelled as friction-controlled backlash. No empirical evidence is found to validate this assumption. However, with great possible certainty it is said to be true since the spring force pressing the cutter to the guard is high. If not, there is a chance that hair may be crushed between the cutter and guard rather than being

actually trimmed.

Furthermore, it was assumed that the trimmer only included two nonlinearities for backlash and Coulomb friction. Consider the illustration of Figure 2.1b, from that it can be said that for a realistic model an additional backlash component is present between the guard housing and plastic housing where the motor is located. This backlash component results from the fact that the essential component are not rigidly mounted to the motor housing so that these components can be cleaned. However, it is assumed that the size of this backlash component was negligible.

6.4 Future Work

- The general Simulink model, used to validate experiment, did not show any limit cycles for $b = 100e - 6$ backlash. Keep in mind that this general differs from the DF theory, since the 'linear' part of the transfer function here includes Coulomb friction nonlinearity. The results from this Simulink model agreed with measurement and hence not limit cycles predicted. It does not mean that DF theory is insufficient. Probably the Coulomb friction alleviates the potential limit cycles. Feed forward friction compensation should show that, based on DF theory, indeed limit cycles are there but friction alleviates the potential limit cycles.

- As seen in the previously, the sinusoidal input DF, represent an approximate mathematical framework for analysing nonlinear systems. However, the method only includes the first harmonics of the Fourier expansion. The overall system might 'show' limit cycling behaviour in higher harmonics. Therefore it is necessary to investigate the procedure of including the higher harmonics of Fourier expansion into the DF method. Ultimately resulting in a more complex condition for harmonic balance. Full credit go to 'P.W.J.M. Nuij, O.H. Bosgra, M. Steinbuch' with their article on *Higher-order sinusoidal input describing functions for the analysis of non-linear systems with harmonic responses* [17].

- Including cascaded DF's in a closed-loop configuration, such that the additional backlash non-linearity can be included for the DF method. Again the overall frequency response is obtained by closing the loop. Previously, it was stated that the the higher harmonics should be filtered out to utilise the condition for harmonic balance. This means that both $G_1(j\omega)$ and $G_1(j\omega)$ should act as a low-pass filter, where $G_1(j\omega)$ and $G_1(j\omega)$, resulting from clever decomposition of $G(j\omega)$

- This study showed that, according to DF theory, only a certain bandwidth of stable limit cycles can occur. The range of the bandwidth showed to be very limited, since the contour of the transfer function comes very close to $(-1, j0)$-point, from which the DF's for backlash originates. As a consequence the bandwidth of potential limit cycles is very limited. In contrast to what has been done in this study, one might consider the effects of altering the model parameters that correspond to the transfer function on the forecasting of limit cycles. A Monte Carlo simulation can be employed for this.

- The theory and results for the viscous-controlled backlash prescribed that only stable limit cycles can be found for this system with a certain range of frequencies. By conducting an experiment, one can determine how friction is affecting the backlash nonlinearity for the trimmer. In doing so, it is essential that the FFT shows that a limit cycle is found for a given amount of backlash. Then the condition for harmonics balance, for viscous-controlled backlash indicated by: Equation 5.11, can be numerically solved for the ratio of M/D. In advance this ratio tells, how friction is affecting the backlash.

- A quantitative model that is able to transform the predicted properties of a limit cycle to unpleasant vibrations. In other words, how 'unpleasant' are the induced limit cycles in the eyes

of a user of the trimmer.

Chapter 7

Conclusion

To analyse the existence of limit cycles in nonlinear systems, the DF theory was employed. This theory is based on the Fourier series with the assumption that limit cycles have sinusoidal shape. DF theory was applied to the trimmer, for which the linear and nonlinear components could be visually separated. The applicability of the DF, requires the transfer function of the trimmer to have low-pass filtering behaviour. It has been shown that the transfer function for this particular met this requirement, but omitting damping is not recommended since this should that a resonant frequency appear in the Bode plot and hence the filtering hypothesis is not entirely achieved.

For trimmer dynamics, two nonlinear elements were considered: backlash and Coulomb friction. However, it was shown that the backlash nonlinearity had multiple forms: friction-controlled, inertia-controlled and viscous-controlled form. More realistically, combinations of the three forms of backlash with Coulomb friction, showed to be applicable to trimmer dynamics. For this realistic scenario an equivalent nonlinear DF was derived. All models showed the existence of a stable limit cycle with approximately equivalent frequency. It is therefore recommended to use the widely known friction-controlled backlash DF since this DF is fairly easy to implement in contrast to the DF for inertia-, viscous-controlled backlash, and the equivalent nonlinear.

An extension of the Nyquist stability theorem states that intersection between the contour of the transfer function and the contour of negative inverse of the DF, suggest limit cycling behaviour. In literature this statement is known as the 'condition for harmonic balance', and if this condition is met limit cycling behaviour is predicted. For this research project 2 transfer functions, corresponding the two distinct trimmers, were examined in the presence of backlash. Firstly, a transfer function related to experiment's trimmer was evaluated. General results of the research relied on a different transfer function however. Based on the condition for harmonic balance, this transfer function predicts a limit cycle for backlash values that are greater than $b \approx 2e - 8$[m]. In advance the stability of these predicted limit cycles was examined. Resulting in only stable limit cycles. Stability of limit cycles can be determined graphically when perturbing the amplitude in positive direction.

Keep in mind that DF method, which is based on a Fourier series, is an approximate method. Only fundamental harmonics are included in this theory. This might lead to inaccuracy of the method, as discussed previously.

Applying the DF method to trimmer dynamics, shows promising results but further research is opted for. Especially, an additional experiment the serves to quantify how friction is affecting backlash for trimmers should be validated. In other words, the ratio of M/D for the realistic viscous-controlled backlash DF should experimentally be determined. In addition, the inclusion of additional backlash component might be necessary to obtain a generic model.

As stated before, this study aimed to investigate the relation between backlash and the existence of limit cycles in trimmer dynamics. The method to conduct this research was to utilise the DF method. subsection 5.2.1 showed the amplitude of the predicted limit cycles was proportional to the size of backlash, providing sufficient sufficient knowledge to answer the main research question:

What is the influence of the size of play to the induced limit cycles and hence to observed vibrations?

The related sub research questions will be answered here:

- What is the effect of damping on the linear stability of the system?
  Linear stability analysis showed that the inclusion of damping resulted in an increase of the magnitude of the resonance frequencies. However, the (anti)resonant frequencies did not change and remained for below the operating frequency of the system. Moreover, it is very unlikely that the induced limit cycle has precisely a frequency corresponding to the (anti)resonant frequency and hence no attenuation for the higher order Fourier coefficients is achieved.

- What is the influence the play element to the stability and performance of the system?
  Despite unstable limit cycles are predicted for certain backlash size, the overall stability of the system is not altered. Especially, the analyses of the results presented in subsection 5.2.3 showed that all operating points corresponding to the unstable limit cycles all had the tendency to shift towards the stable limit cycle regime.
  The inclusion of backlash does affect the performance of the system, since it contributions to the existence of limit cycles and hence additional oscillations. There is a proportional relations between the size of backlash b and the amplitude of the limit cycle.

- What is the influence of the frictional components the stability and performance of the system?
  Similar to the answer on the previous question, the stability is not altered with the inclusion of Coulomb friction, however the performance does change. With the help of experiment's findings, described in section 3.3, it was shown that the induced limit cycles resulting from backlash were suppressed when Coulomb friction was introduced to the system. Coulomb friction between the cutter and guard is therefore actually a desired element.

- What is the influence of the input amplitude, and backlash width, to the stability and performance of the system?
  The open-loop configuration with external driving input, showed that the input amplitude had not effect on the properties of the limit cycle. It has to be noted that there is a distinction between the input amplitude and the amplitude of the limit cycles.

- What is the influence of the input frequency to the stability and performance of the system?
  For friction-, and inertia-controlled backlash the performance of the of the system does not change since the related DF are frequency independent. Resulting in the 'normal' condition for harmonic balance from which the amplitude of the predicted limit cycle is determined from the DF part, while the frequencies is solely resulting from the transfer function part. For viscous-controlled backlash and for the equivalent nonlinearity, the DF depends on the input frequency. In subsection 5.2.5 it was shown that the equivalent nonlinear DF, results to a DF contour similar to the contour of friction-controlled DF, whereas decreasing frequency the DF contour results in a contour similar to the contour of inertia-controlled DF. Despite this observations, the system's performance barely alters since there is a limited range of frequency for which stable limit cycle can exist at all.

- How does the predicted limit cycle, by the describing function method, manifest itself in the output of the system?
  As seen throughout this research, the generated limit cycle manifest itself as sub oscillations on top of base oscillations, corresponding to the driving function, for the realistic open-loop configuration. For closed-loop, without external input, the limit cycles are the only oscillations in the time response of the output of the system. It has been shown that the closed-loop

configuration is a practical way to determine the properties of the limit cycles since the open-loop configuration also should subharmonics corresponding to the driving input and hence it was sometimes impractical to visually validate which peak in the FFT corresponded to a limit cycle and which peak corresponded to a subharmonic.

Open-loop configuration is however helpful to validate data to Simulink model, since the data is obtained from a open-loop configuration with external input.

Bibliography

[1] A. Gelb and W. E. V. Velde, "Multiple-input describing functions and nonlinear system design," 1968.

[2] J.-J. E. Slotine and W. Li, *Applied nonlinear control*. Upper Saddle River, NJ: Pearson, Oct. 1990.

[3] X. Chen, F. Fang, and X. Luo, "A friction identification approach based on dual-relay feedback configuration with application to an inertially stabilized platform," *Mechatronics*, vol. 24, pp. 1120–1131, Dec. 2014.

[4] L. Keviczky, R. Bars, J. Hetthéssy, and C. Bányász, "Stability of linear control systems," in *Advanced Textbooks in Control and Signal Processing*, pp. 197–239, Springer Singapore, Oct. 2018.

[5] M. Amin, C. Zhang, A. Rygg, M. Molinas, E. Unamuno, and M. Belkhayat, "Nyquist stability criterion and its application to power electronics systems," May 2019.

[6] M. S. Fadali and A. Visioli, "Stability of digital control systems," in *Digital Control Engineering*, pp. 87–121, Elsevier, 2009.

[7] J. H. Taylor, "Describing functions," Dec. 1999.

[8] L. T. Aguilar, I. Boiko, L. Fridman, and R. Iriarte, *Self-Oscillations in Dynamic Systems*. Springer International Publishing, 2015.

[9] Z. Úředníček, "Describing functions and prediction of limit cycles," *WSEAS Transactions on Systems and Control 13*, vol. 1991-8763, 2018.

[10] A. Jopling and R. Johnson, "The elliptic describing function," *IEEE Transactions on Automatic Control*, vol. 9, no. 4, pp. 458–468, 1964.

[11] A. Mashayekhi, S. Behbahani, A. Nahvi, M. Keshmiri, and M. Shakeri, "Analytical describing function of LuGre friction model," *International Journal of Intelligent Robotics and Applications*, vol. 6, pp. 437–448, Jan. 2022.

[12] M. Ruderman, "Stick-slip and convergence of feedback-controlled systems with coulomb friction," *Asian Journal of Control*, Oct. 2021.

[13] E. Davison and D. Constantinescu, "A describing function technique for multiple nonlinearities in a single-loop feedback system," *IEEE Transactions on Automatic Control*, vol. 16, no. 1, pp. 56–60, 1971.

[14] L. Tan and J. Jiang, "Chapter 4 - discrete fourier transform and signal spectrum," in *Digital Signal Processing (Third Edition)* (L. Tan and J. Jiang, eds.), pp. 91–142, Academic Press, third edition ed., 2019.

[15] L. Marino and A. Cicirello, "Multi-degree-of-freedom systems with a coulomb friction contact: analytical boundaries of motion regimes," *Nonlinear Dynamics*, vol. 104, pp. 35–63, Mar. 2021.

[16] H. Olsson, "Describing function analysis of a system with friction," in *Proceedings of International Conference on Control Applications*, IEEE.

[17] P. Nuij, O. Bosgra, and M. Steinbuch, "Higher-order sinusoidal input describing functions for the analysis of non-linear systems with harmonic responses," *Mechanical Systems and Signal Processing*, vol. 20, pp. 1883–1904, Nov. 2006.

[18] M. H. Al-qatamin, "An optimal state feedback controller based neural networks for synchronous generator excitation control system," *International Journal of Electrical and Computer Engineering (IJECE)*, vol. 3, May 2013.

[19] A. Bergen, L. Chua, A. Mees, and E. Szeto, "Error bounds for general describing function problems," Tech. Rep. UCB/ERL M81/55, EECS Department, University of California, Berkeley, Jul 1981.

[20] S. Engelberg, "Limitations of the describing function for limit cycle prediction," *IEEE Transactions on Automatic Control*, vol. 47, pp. 1887–1890, Nov. 2002.

Appendices

Appendix A

Matlab codes

A.1   Transfer function derivation

$$sQ(s) - AQ(s) = BU(s)$$
$$(sI - A)Q(s) = BU(s) \tag{A.1}$$
$$Q(s) = (sI - A)^{-1}BU(s)$$

putting this into the output equation of Equation 2.20;

$$Y(s) = C[(sI - A)^{-1}BU(s)] + DU(s)$$
$$Y(s) = (C(sI - A)^{-1}B + D)U(s) \tag{A.2}$$

$$\int_{\frac{\pi}{2}}^{\pi-\sin^{-1}\left(1-\frac{2\,b}{A}\right)} (A-b)\cos(t)\,dt = \frac{2\,b\,(b-A)}{A}$$

$$\int_{\pi-\sin^{-1}\left(1-\frac{2\,b}{A}\right)}^{\frac{3\,\pi}{2}} (A\sin(t)+b)\cos(t)\,dt = 0$$

$$\int_{\frac{3\,\pi}{2}}^{2\,\pi-\sin^{-1}\left(1-\frac{2\,b}{A}\right)} -(A-b)\cos(t)\,dt = \frac{2\,b\,(b-A)}{A}$$

$$\int_{2\,\pi-\sin^{-1}\left(1-\frac{2\,b}{A}\right)}^{\frac{5\,\pi}{2}} (A\sin(t)-b)\cos(t)\,dt = 0$$

A.2   General code form computing properties of linear model

The code for the construction of the linear part of the system is shown in Listing A.1. From the EOM (Equation 2.9), the state-space representation is obtained by line: `sys = ss(A,B,C,D)`, with associating A-, B-, C- and D-matrices. Code is then able to compute the transfer function corresponding to the state-space representation by the line: `G = tf(sys)`. Note that the obtained transfer function, for this model, is a double input/single output transfer function, since the system is a dissipating system and hence the B-matrix, in state-space representation, has 2 columns, i.e. B-matrix $\in \mathbb{R}^{8\times2}$. Where the first column is associated with the relative displacement and the second column is associated with the relative velocity of the trimmer. However, the required output matrix (C-matrix), tracks the relative displacement of the trimmer and hence only the first transfer function of the double input/single output transfer function is used.

Listing A.1: Code properties linear model

```
1  %% This section states the state-space model, and from the model the bodeplot is ...
       obtained
2  clear all; clc; close all;
3
4  m1 = 0.035;
5  m2 = 0.003;
6  m3 = 0.005;
7  m4 = 0.030;
8
9  k1 = 200e3;
10  k2 = 30e3;
11  k3 = 150e3;
12  k4 = 100e3;
13  k5 = 1e3;
14
15  c1 = 3.5;
16  c2 = 0.4;
17  c3 = 1.0;
18  c4 = 4.0;
```

```matlab
19
20  %State variables, do NOT uncomment variables x1,...,x8 below!
21  % x1 = q1
22  % x2 = q2
23  % x3 = q3
24  % x4 = q4
25  % x5 = dq1
26  % x6 = dq2
27  % x7 = dq3
28  % x8 = dq4
29
30  A = [0 0 0 0 1 0 0 0;
31       0 0 0 0 0 1 0 0;
32       0 0 0 0 0 0 1 0;
33       0 0 0 0 0 0 0 1;
34       -(k1+k2)/m1 k2/m1 0 0 -(c1+c2)/m1 c2/m1 0 0;
35       k2/m2 -(k2+k5)/m2 k5/m2 0 c2/m2 -c2/m2 0 0;
36       0 k5/m3 -(k3+k4+k5)/m3 k4/m3 0 0 -(c3+c4)/m3 c4/m3;
37       0 0 k4/m4 -k4/m4 0 0 c4/m4 -c4/m4];
38
39  B = [0 0;
40       0 0;
41       0 0;
42       0 0;
43       -k2/m1 -c2/m1;
44       k2/m2 c2/m2;
45       0 0;
46       0 0];
47  % two antiresonance frequencies
48
49  % Desired output
50  C = [0 1 0 -1 0 0 0 0];                                        % ...
        Output relative position of cutter (x2) and guard (x4)
51  D = 0;
52
53  % Construct SS-model
54  sys = ss(A,B,C,D);
55
56  % Construct transfer function based on SS-model
57  G = tf(sys);
58  G = G(1);
```

A.3   Code DF friction-controlled backlash

Listing A.2: Code DF friction-controlled backlash

```matlab
1  function N =  backlash_describing_func_2(A, b)
2      %A = amplitude range
3      %b = Size of backlash
4
5      N = zeros(size(A));
6      N(A < b) = 0;
7      CgtrD = A(A >= b);
8
9      N_re = (0.5 + 1/pi*(1 - (b./A)).*sqrt(1 - (1 - b./A).^2) + 1/pi * asin(1 - ...
          (b./A)));
10     N_im = -((1)./(pi)).*(1 - (1 - b./A).^2);
11
```

```
12        N = N_re + 1i*N_im;
13  end
```

A.4   Code friction-controlled backlash DF

Code listed in Listing A.3 takes three input arguments: the input wave $e(t)$, the deadband width D_{size} and the previous output from the block u_{prev}. The latter is needed to make the if-else statement work. The code is based on the potential values of the friction-controlled backlash DF of Equation 2.36

Listing A.3: Code DF friction-controlled backlash

```matlab
1  function N =  backlash_describing_func_2(A, b)
2      %A = amplitude range
3      %b = Size of backlash
4
5      N = zeros(size(A));
6      N(A < b) = 0;
7      CgtrD = A(A >  b);
8
9      N_re = (0.5 + 1/pi*(1 - (b./A)).*sqrt(1 - (1 - b./A).^2) + 1/pi * asin(1 - ...
             (b./A)));
10     N_im = -((1)./(pi)).*(1 - (1 - b./A).^2);
11
12     N = N_re + 1i*N_im;
13  end
```

A.5   Code inertia-controlled backlash

Listing A.4: Code DF inertia-controlled backlash

```matlab
function [N] =  backlash_DF_inertia_0910(Beta, w)
x = sym('x');
eqnLeft = sin(w*x);                              % phi is scaled by w
eqnRight = w.*x - Beta;
sym_phi = vpasolve(eqnLeft == eqnRight, x);
phi = sym2poly(sym_phi);                         % This phi has to go into the ...
    nested function
N = myN(Beta,phi);
    function N = myN(Beta,phi)
        N_re = (1/pi)*(pi + 2*sin(sin(phi)  +Beta) - phi - sin(sin(phi)  ...
            +Beta).*cos(sin(phi)  +Beta));
        N_im = -(1/pi)*(1 - cos(sin(phi)  +Beta)).^2;

        N = N_re + 1i*N_im;
    end
end
```

A.6 Code viscous-controlled backlash

Listing A.5: Code DF viscous-controlled backlash

```matlab
1  function [N] = viscous_DF(Beta,phi)
2
3  phi_s = atan(1./phi);
4
5  x = sym('x');
6  eqnLeft = sqrt(1 - phi.^2) - Beta;
7  eqnRight = sin(x) + ((phi.^2).*exp((1./phi).*(atan(1./phi) - x)))./(sqrt(1 + phi.^2));
8  sym_phi = vpasolve(eqnLeft == eqnRight, x);
9  phi_c = sym2poly(sym_phi);
10
11 np = ((2*phi.^2)./(pi.*(1 + phi.^2))).*[((1 + phi.^2)./(2.*phi.^2)).*(phi_s - ...
       phi_c + pi + sin(phi_c).*cos(phi_c)) + 1./(2*phi) + ...
12     (1./phi).*(Beta - sqrt(1 + phi.^2)).*((1./phi).*cos(phi_c) - sin(phi_c)) - ...
13     (1./phi).*sin(phi_c).^2 - sin(phi_c).*cos(phi_c)];
14
15 nq = ((-2*phi.^2)./(pi.*(1 + phi.^2))).*[1 + 1./(2.*phi.^2) + ((1 - ...
       phi.^2)./(2.*phi.^2)).*sin(phi_c).^2 + ...
16      (1./phi).*(Beta - sqrt(1+phi.^2)).*((1./phi).*sin(phi_c) + cos(phi_c)) + ...
17     (1./phi).*(sin(phi_c).*cos(phi_c))];
18
19 N = np + 1i*nq;
20 end
```

A.7   Code equivalent nonlinearity

Listing A.6: Code DF viscous-controlled backlash

```matlab
1  function N = equivalent_nonlin(A,D,w,Fc)
2  %UNTITLED2 Summary of this function goes here
3  %   Detailed explanation goes here
4      %A = amplitude input wave
5      %D = Size of backlash
6
7      Nr = zeros(size(A));
8      Nr(A < D) = 0;
9      CgtrD = A(A >= D);
10     N_re = (0.5 + 1/pi*(1 - (D./A)).*sqrt(1 - (1 - D./A).^2) + 1/pi * asin(1 - ...
           (D./A)));
11     N_im = -((1)./(pi)).*(1 - (1 - D./A).^2);
12     Nr = N_re + 1i*N_im;
13     a_1 =0;
14     b_1 = (4*Fc)/pi;
15     Nf = (1./A)*(b_1 + 1i*a_1);
16
17
18     N = Nr - (1i/w)*Nf
19 end
```

A.8   Code friction-controlled backlash based on time domain

Listing A.7: Code DF friction-controlled backlash time domain

```
1  function u = fcn(e, D_size, u_prev)
2  if e - u_prev > D_size/2
3        u = e - D_size/2;
4  else
5      if e - u_prev < -D_size/2
6          u = e + D_size/2;
7      else
8       u = u_prev;
9      end
10 end
11 end
12 end
```

A.9   Code inertia-controlled backlash based on time domain

The code only takes two input arguments, namely: the input wave $u(t) = A\sin(\omega t)$ and t which is time. Code produces required output stated by Equation 2.42. The code is able to reproduce results over multiple period by replacing t by `mod(t,T)`. `mod(t,T)` returns the remainder after division of t by T. Validation of the function block is done by observing that the output wave, when applying an input wave, matches the trend shown by Figure 2.10. Again $A = 0.0015$[m] $b = 0.0004$[m] and $f = 109.845$[Hz]

Listing A.8: Code DF inertia-controlled backlash

```
1  function y = fcn(u,t)
2  b = 0.0004;                              %Backlash size
3  A = 0.0015;                              %Input amplitude
4  w = 200*pi;
5  freq = 100;
6  w = 2*pi*freq;
7  T = 2*pi/w;
8  phi = 0.00190662;                        %Numerical computed connection point
9
10 y = (w*A*mod(t,T) - b/2)                 .*(mod(t,T)≥0 & mod(t,T)<phi)...
11        + (u + b/2)                       .*(mod(t,T)>phi & mod(t,T)<T/2)...
12        + (-w*A*mod(t,T) + 0.0049)        .*(mod(t,T)≥T/2 & mod(t,T)<T/2+phi)...
13        + (u - b/2)                       .*(mod(t,T)>T/2+phi & mod(t,T)<T);
14
15
16 end
```

A.10   General nonlinear code Coulomb Friction DF

The code listed in Listing A.9 is able to check if the condition for harmonic balance is satisfied between the linear transfer function and the nonlinear friction-controlled backlash DF. Where the friction-controlled DF, line 8, can be replaced by the external functions for the other nonlinearities as well. First, the size of backlash is defined (line 5), subsequently an external function associated to the nonlinearity of is called (line 8). Then the negative inverse of that nonlinearity is plotted on the complex plane together with the linear transfer function (line 13 and 14). Intersections of the two curves are performed by the `fsolve`-command (line 22). The function return the amplitude and frequency corresponding to the predicted limit cycle. Intersections are then plotted on the same graph. After that simulink is used again to validate the predictions, based on DF theory. Zero external input model is then compared to similar model, subjected to model with driving input frequency, by means of the FFT.

Listing A.9: General code for computing intersection between friction-controlled backlash and transfer function

```
1  %% Nonlinear part
2  clc; close all;
3
4  % Define deadband width
5  b = 0.00004;
6
7  % Call external DF
8  N = @(A) backlash_describing_func_2(A, b)
9  cc = linspace(b/2+0.000001,0.0025,10000);
10
11  % Plot Nyquist of linear TF with 1/N DF
12  figure(1);
13  nyquist(G(1)); hold on;
14  plot(real(-1./N(cc)), imag(-1./N(cc)), 'r', 'LineWidth', 1)
15
16
17  % Define TF obtain from linear model
18  G_1 = @(s)(1e07*s^6 + 1.233e10*s^5 + 5.939e14*s^4 + 1.65e17*s^3 + 4.065e21*s^2 + ...
       3.667e23*s + 5.714e27)/ (s^8 + 1378*s^7 + 7.076e07*s^6 + 3.878e10*s^5 + ...
       1.069e15*s^4 + 2.676e17*s^3 + 4.889e21*s^2 + 4.595e23*s + 5.971e27)
19
20
21  % Compute intersection point between TF and 1/N
22  [xopt, res] = fsolve(@(x) [real(N(x(1)))*real(G_1(1i*x(2))) - ...
       imag(N(x(1)))*imag(G_1(1i*x(2))) + 1;
23                          real(N(x(1)))*imag(G_1(1i*x(2))) + ...
                              imag(N(x(1)))*real(G_1(1i*x(2)))  ], x0);
24
25  % Initial guesses to compute fsolve
26  A0 = 0.0003;
27  w0 =3500;
28  x0 = [A0, w0];
29
30  A_opt(1) = xopt(1)
31  w_opt(1) = xopt(2)
32  f_opt = w_opt(1)/(2*pi)
33  T_period = 1/f_opt
34  plot(real(G_1(1i*w_opt(1))), imag(G_1(1i*w_opt(1))), 'ko')
35  xlim([-8 0])
36  ylim([-20 2])
```

A.11   Code inertia-controlled DF for backlash

Listing A.10: Code DF inertia-controlled backlash

```matlab
function [N] =  backlash_DF_inertia_0910(Beta, w)
x = sym('x');
eqnLeft = sin(w*x);                                 % phi is scaled by w
eqnRight = w.*x - Beta;
sym_phi = vpasolve(eqnLeft == eqnRight, x);
phi = sym2poly(sym_phi);                            % This phi has to go into the ...
    nested function
N = myN(Beta,phi);
    function N = myN(Beta,phi)
        N_re = (1/pi)*(pi + 2*sin(sin(phi)  +Beta) - phi - sin(sin(phi)  ...
            +Beta).*cos(sin(phi)  +Beta));
        N_im = -(1/pi)*(1 - cos(sin(phi)  +Beta)).^2;

        N = N_re + 1i*N_im;
    end
end
```

Appendix B

Derivation Fourier coefficients

B.1 Derivation Fourier coefficients backlash operator

$$
a_1 = \frac{1}{\pi} \underbrace{\int_{\pi/2}^{\pi-\gamma} (A-b)\cos(\omega t) d(\omega t)}_{= \frac{2b(b-A)}{A}}
$$

$$
+ \frac{1}{\pi} \underbrace{\int_{\pi-\gamma}^{3\pi/2} (A\sin(\omega t)+b)\cos(\omega t) d(\omega t)}_{=0}
$$

$$
+ \frac{1}{\pi} \underbrace{\int_{3\pi/2}^{2\pi-\gamma} -(A-b)\cos(\omega t) d(\omega t)}_{= \frac{2b(b-A)}{A}}
$$

$$
+ \frac{1}{\pi} \underbrace{\int_{2\pi-\gamma}^{\frac{5\pi}{2}} (A\sin(\omega t)-b)\cos(\omega t) d(\omega t)}_{=0}
$$

(B.1)

so the Fourier coefficient for a_1 is:

$$
a_1 = \frac{1}{\pi} \left[\frac{2b(b-A)}{A} + 0 + \frac{2b(b-A)}{A} + 0 \right]
$$

$$
a_1 = \frac{4b}{\pi} \left(\frac{b}{A} - 1 \right)
$$

(B.2)

B.2 Viscous DF coefficients

$$
n_p(A,\omega) = \frac{2\gamma^2}{\pi(1+\gamma^2)} \left(\frac{1+\gamma^2}{2\gamma^2}(\phi_s - \phi_c + \pi + \sin(\phi_c)\cos(\phi_c)) + \frac{1}{2\gamma} \right.
$$

$$
+ \frac{1}{\gamma} \left(\frac{b}{A} - \sqrt{1+\gamma^2} \right) \left(\frac{1}{\gamma}\cos(\phi_c) - \sin(\phi_c) \right)
$$

$$
\left. - \frac{1}{\gamma}\sin^2(\phi_c) - \sin(\phi_c)\cos(\phi_c) \right)
$$

(B.3)

$$n_q(A, \omega) = \frac{-2\gamma^2}{\pi(1 + \gamma^2)} \left(1 + \frac{1}{2\gamma^2} + \left(\frac{1 - \gamma^2}{2\gamma^2} \right) \sin^2(\phi_c) \right.$$
$$+ \frac{1}{\gamma} \left(\frac{b}{A} - \sqrt{1 + \gamma^2} \right) \left(\frac{1}{\gamma} \sin(\phi_c) + \cos(\phi_c) \right) \tag{B.4}$$
$$\left. + \frac{1}{\gamma} \sin(\phi_c) \cos(\phi_c) \right)$$

Appendix D

Derivation EOM based on Euler-Lagrange

For q_1 the EOM are derived as follows. Consider:

$$\frac{d}{dt}\left(\frac{\partial \mathcal{L}}{\partial \dot{q}_i}\right) - \frac{\partial \mathcal{L}}{\partial q_i} + \frac{\partial R}{\partial \dot{q}_i} = Q_i$$

where

$$\mathcal{L} = T - V$$
$$\mathcal{L} = \frac{1}{2}m_1\dot{q}_1^2 + \frac{1}{2}m_2\dot{q}_2^2 + \frac{1}{2}m_3\dot{q}_3^2 + \frac{1}{2}m_4\dot{q}_4^2 -$$
$$\left(\frac{1}{2}k_1(q_1)^2 + \frac{1}{2}k_2(q_2 - q_1 - u)^2 + \frac{1}{2}k_3q_3^2 + \frac{1}{2}k_4(q_4 - q_3)^2 + \frac{1}{2}k_5(q_2 - q_3)^2\right)$$

and

$$R = \frac{1}{2}c_1\dot{q}_1^2 + \frac{1}{2}c_2(\dot{q}_2 - \dot{q}_1 - \dot{u})^2 + \frac{1}{2}c_3\dot{q}_3^2 + \frac{1}{2}c_4(\dot{q}_4 - \dot{q}_3)^2$$

then

$$\frac{d}{dt}\left(\frac{\partial \mathcal{L}}{\partial \dot{q}_1}\right) = \frac{d}{dt}(m_1\dot{q}_1) = m_1\ddot{q}_1$$

$$\frac{\partial \mathcal{L}}{\partial q_1} = k_1q_1 - k_2q_2 + k_2q_1 + k_2u$$

$$\frac{\partial R}{\partial \dot{q}_1} = c_1\dot{q}_1 - c_2\dot{q}_2 + c_2\dot{q}_1 + c_2\dot{u}$$

such that:

$$\ddot{q}_1 = \frac{1}{m_1}\left[-(c_1 + c_2)\dot{q}_1 + c_2\dot{q}_2 - (k_1 + k_2)q_1 + k_2q_2 - k_2u - c_2\dot{u}\right]$$

The transform function related to the state-space representation is derived as:

$$sQ(s) = AQ(s) + BU(s)$$
$$Y(s) = CQ(s) + DU(s)$$

Appendix E

Summary varying backlash widths and input amplitude

Associated simulink models are computed, to validate that the limit cycles have varying amplitudes but equal frequencies related to Table 5.2. This is shown in Figure E.1: Further investigating the
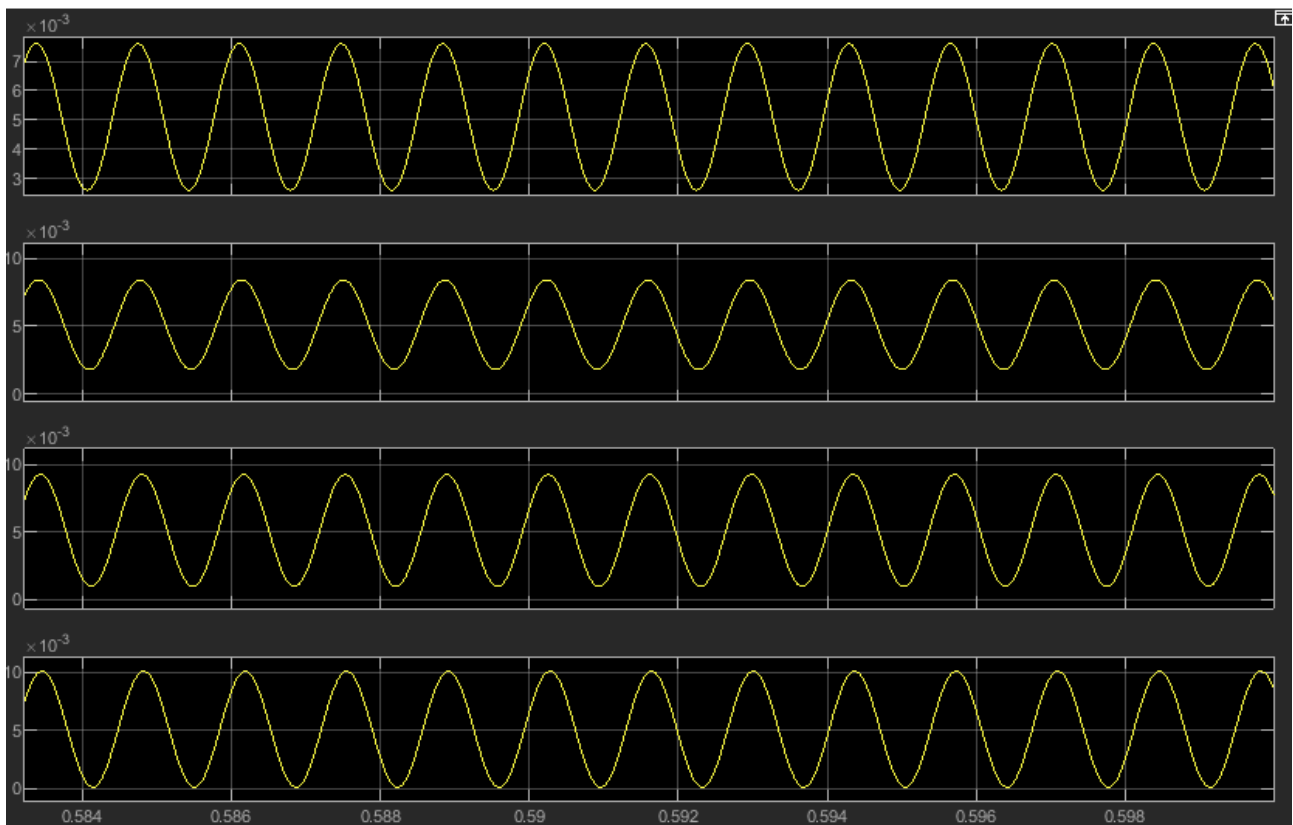

Figure E.1: Backlash model with varying backlash size widths with zero external input. Backlash varies from top to bottom: $3e - 4$[m], $4e - 4$[m], $5e - 4$[m] and $6e - 4$[m]

scope of simulink indeed shows that the amplitudes are in agreement with the predicted amplitudes from **??**, and all have similar frequency.

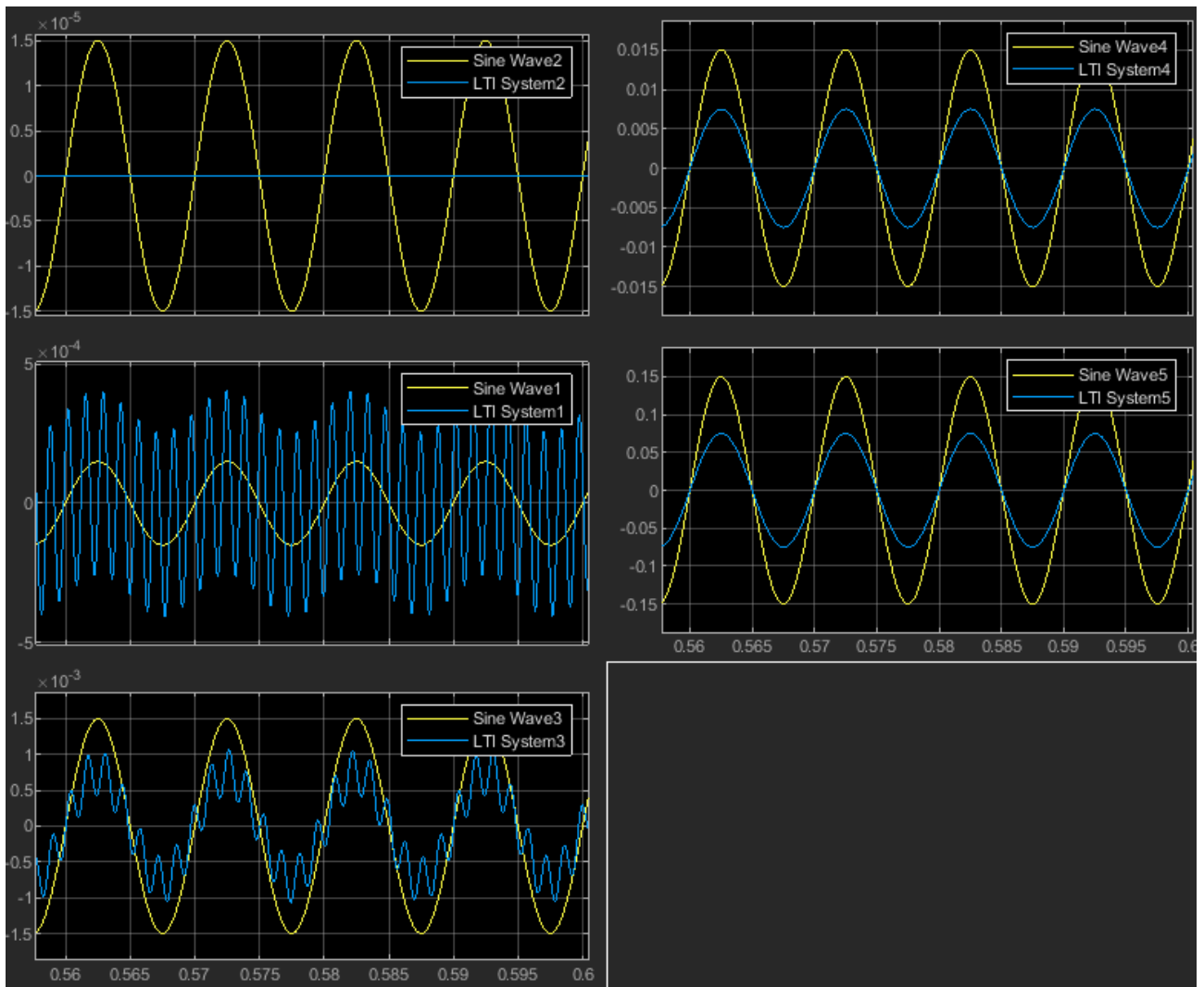Results for of the open-loop system for varying input amplitude.

Figure E.2: Yellow curve corresponds to input wave, blue curve corresponds to output.
Top left: input wave amplitude is $1.5e-6$[m], top right:input wave amplitude is $1.5e-2$[m], middle left: input wave amplitude is $1.5e-4$[m], middle right: input wave amplitude is $1.5e-1$[m] and bottom left: input wave amplitude is $1.5e-3$[m], for $b=4e-5$